

Production of strangeness in partonic interaction at the LHC

Production of strangeness in partonic interaction at the LHC

by Oliver Matonoha



LUND
UNIVERSITY

Thesis for the degree of Doctorate

Thesis advisors: Prof. Doktor Professorsson, Prof. Knirk Gnork

Faculty opponent: Prof. Gammal och Grå

To be presented, with the permission of the Faculty of Natural Sciences of Lund University, for public
criticism at LINXS (Delta 5, floor 5, IDEON building) on Friday, the 9th of June 2023 at 13:15.

Organization LUND UNIVERSITY	Document name LICENTIATE THESIS	
Department of Physics Box 124 SE-221 00 LUND Sweden	Date of disputation 2020-10-30	
Author(s) Oliver Matonoha	Sponsoring organization	
Title and subtitle Production of strangeness in partonic interaction at the LHC		
Abstract <p> Lorem ipsum dolor sit amet, consectetur adipiscing elit. Etiam lobortis facilisis sem. Nullam nec mi et neque pharetra sollicitudin. Praesent imperdiet mi nec ante. Donec ullamcorper, felis non sodales commodo, lectus velit ultrices augue, a dignissim nibh lectus placerat pede. Vivamus nunc nunc, molestie ut, ultricies vel, semper in, velit. Ut porttitor. Praesent in sapien. Lorem ipsum dolor sit amet, consectetur adipiscing elit. Duis fringilla tristique neque. Sed interdum libero ut metus. Pellentesque placerat. Nam rutrum augue a leo. Morbi sed elit sit amet ante lobortis sollicitudin. Praesent blandit blandit mauris. Praesent lectus tellus, aliquet aliquam, luctus a, egestas a, turpis. Mauris lacinia lorem sit amet ipsum. Nunc quis urna dictum turpis accumsan semper.</p>		
Key words quantum chromodynamics, quark-gluon plasma		
Classification system and/or index terms (if any)		
Supplementary bibliographical information	Language English	
ISSN and key title	ISBN 123456789 (print) 123456789 (pdf)	
Recipient's notes	Number of pages 201	Price
	Security classification	

I, the undersigned, being the copyright owner of the abstract of the above-mentioned dissertation, hereby grant to all reference sources the permission to publish and disseminate the abstract of the above-mentioned dissertation.

Signature _____

Date **2020-09-18**

Production of strangeness in partonic interaction at the LHC

by Oliver Matonoha



LUND
UNIVERSITY

A licentiate thesis at a university in Sweden takes either the form of a single, cohesive research study (monograph) or a summary of research papers (compilation thesis), which the licentiate student has written alone or together with one or several other author(s).

In the latter case the thesis consists of two parts. An introductory text puts the research work into context and summarizes the main points of the papers. Then, the research publications themselves are reproduced, together with a description of the individual contributions of the authors. The research papers may either have been already published or are manuscripts at various stages (in press, submitted, or in draft).

Cover illustration front: Cool figure by bla and bla.

Cover illustration back: Another cool image by bla.

Funding information: The thesis work was financially supported by the Swedish Research Council.

© Oliver Matonoha 2023

Faculty of Natural Sciences, Department of Physics

ISBN: 123456789 (print)

ISBN: 123456789 (pdf)

Printed in Sweden by Media-Tryck, Lund University, Lund 2023



Media-Tryck is a Nordic Swan Ecolabel certified provider of printed material.
Read more about our environmental work at www.mediathyck.lu.se

MADE IN SWEDEN

*Dedicated to
Humpty – Dumpty
bla bla blat*

Contents

List of publications	v
Acknowledgements	vi
Populärvetenskaplig sammanfattning på svenska	vii
Production of strangeness in partonic interaction at the LHC	1
I Fundamental theory	3
1 Introduction to quantum chromodynamics	5
1.1 Standard Model of elementary particles	5
1.2 Coordinate systems and kinematic observables	8
1.3 Quantum electrodynamics, electrons, and photons	8
1.4 Quantum chromodynamics, quarks, and gluons	10
1.5 From partons to hadrons	12
1.5.1 Initial and Final State Radiation	12
1.5.2 Factorisation theorem	13
1.5.3 Parton distribution functions	14
1.5.4 Parton fragmentation and the Lund string	15
1.6 Multiple partonic interactions	17
1.6.1 Color reconnection	19
1.7 Underlying event	20
1.8 From hadrons to partons: deconfined QCD matter	21
1.8.1 Bag model of hadrons	21
1.8.2 Lattice QCD	22
1.8.3 QCD phase diagram, chiral symmetry restoration	23
2 QCD phenomena in high energy hadronic collisions	25
2.1 Collisions of heavy nuclei	25
2.1.1 Collision geometry, centrality, multiplicity	25
2.1.2 MC Glauber model	26
2.2 Quark-gluon plasma	28
2.2.1 Quarkonium dissociation and sequential suppression	29
2.2.2 Strangeness enhancement	31

2.2.3	Collective flow	32
2.2.4	Jet quenching	35
2.2.5	Cold nuclear matter effects	36
2.3	QGP phenomena in small systems	36
2.3.1	Role of multiplicity	41
2.4	Phenomenological models	42
2.4.1	Pythia	42
2.4.2	String interactions and Ropes	44
2.4.3	EPOS LHC	45
II	Experimental Setup and Methodology	49
3	ALICE’s adventures at the LHC	51
3.1	CERN and the LHC	51
3.2	The ALICE experiment	52
3.3	Time Projection Chamber	55
3.3.1	Upgrade for Run 3: GEM read-outs	55
3.4	Inner Tracking Systems	57
3.5	V0A and V0C	58
4	Events, Tracks, and Vertices	61
4.1	Events and triggers	61
4.2	Event and track reconstruction	62
4.2.1	First primary vertex determination	62
4.2.2	Tracking	63
4.2.3	Finding secondary vertices	64
4.3	Centrality and multiplicity measurements and their caveats	66
4.4	Used tracks	68
4.4.1	Hybrid tracks	69
4.4.2	Geometrical cuts on tracks	69
III	Author’s measurements	71
5	Reconstruction of neutral strange particles with ALICE	73
5.1	Analysed datasets	73
5.2	Identification of V^0 s using ALICE	74
5.3	Signal extraction	74
5.3.1	Validation using simulations	76
5.4	Normalisation	77
5.5	Corrections to the reconstructed production	78
5.5.1	Secondary contribution correction	78
5.5.2	Reconstruction efficiency	80

5.6	Transverse momentum spectra	81
5.6.1	Comparisons with previously published results	81
5.7	Systematic uncertainties	82
5.7.1	Variation of selection criteria	84
5.7.2	Feeddown correction	85
6	Transverse Spherocity	89
6.1	Transverse spherocity	89
6.1.1	Motivation for studying event topology	89
6.1.2	S_O and $S_O^{(p_T=1.0)}$ as experimental observables	90
6.1.3	Relationship between $S_O^{(p_T=1.0)}$ and S_O	93
6.1.4	Track and event selection	94
6.1.5	Multiplicity selection and its interplay with $S_O^{(p_T=1.0)}$	95
6.1.6	Comparison of V^0 production with MC generators	97
6.2	Systematic uncertainties	98
6.2.1	Experimental bias	100
6.2.2	Correlation of uncertainties with $S_O^{(p_T=1.0)}$	101
6.2.3	Summary	101
6.3	Transverse momentum spectra vs. $S_O^{(p_T=1.0)}$	103
6.3.1	Ratios of neutral kaons to charged kaons	105
6.4	Mean transverse momenta and integrated yields	105
6.5	Ratios to pions	107
6.6	Baryon-to-meson ratio	109
6.7	Ratio of integrated yields vs. $S_O^{(p_T=1.0)}$	110
7	Underlying Event Activity	113
7.1	Motivation for studying event sub-structure	113
7.1.1	Underlying event	113
7.1.2	Hard process–multiplicity bias	113
7.1.3	Azimuthal regions and transverse activity	114
7.2	R_T as an experimental observable	115
7.2.1	Proxy to n_{MPI}	116
7.2.2	Extension to $R_{T,\min}$, $R_{T,\max}$	117
	Charged particle p_T spectra	118
7.2.3	Track and event selection	119
7.2.4	R_T measurements of neutral particles vs. charged particles .	120
7.3	Bayesian unfolding procedure	120
7.3.1	One-dimensional unfolding	121
7.3.2	Unfolding of K_S^0 , Λ , and $\bar{\Lambda}$ p_T spectra	125
7.4	R_T , $R_{T,\min}$, $R_{T,\max}$ distributions	127
7.5	Systematic uncertainties	130

7.5.1	Uncertainties from the unfolding procedure	133
7.5.2	Uncorrelated uncertainties	134
7.6	Description of regions and mean transverse momentum	135
7.7	Transverse momentum spectra	138
7.8	Baryon-to-meson ratio	143
7.9	Integrated yields	147
8	Discussion of results, conclusions, and outlooks	149
8.1	Summary of the research goals	149
8.2	Highlights of the $S_O^{(p_T=1.0)}$ measurement	150
8.3	Highlights of the R_T measurements	151
8.4	Conclusions and Outlooks	153
IV	Appendices	155
A	List of Acronyms	157
B	Mathematical Derivations	159
C	Complementary Material	161
D	Scientific Publications	163
	Author contributions	163
	Paper I: Title paper 1	163
	Paper II: Title paper 2	163
	Paper I: Title paper 1	165
	Paper II: Title paper 2	169
	References	173

List of publications

This thesis is based on the following publications, referred to by their Roman numerals:

I Title paper 1

S. Doctor, B. Someone

The Journal of Physical Chemistry A, 2020, 124(19), pp. 3943-3946

II Title paper 2

S. Doctor, B. Someone, C Another

Physical Chemistry Chemical Physics, 2020, 22(24), pp. 13659-13665

All papers are reproduced with permission of their respective publishers.

Acknowledgements

Lorem ipsum dolor sit amet, consectetuer adipiscing elit. Etiam lobortis facilisis sem. Nullam nec mi et neque pharetra sollicitudin. Praesent imperdiet mi nec ante. Donec ullamcorper, felis non sodales commodo, lectus velit ultrices augue, a dignissim nibh lectus placerat pede. Vivamus nunc nunc, molestie ut, ultricies vel, semper in, velit. Ut porttitor. Praesent in sapien. Lorem ipsum dolor sit amet, consectetuer adipiscing elit. Duis fringilla tristique neque. Sed interdum libero ut metus. Pellentesque placerat. Nam rutrum augue a leo. Morbi sed elit sit amet ante lobortis sollicitudin. Praesent blandit blandit mauris. Praesent lectus tellus, aliquet aliquam, luctus a, egestas a, turpis. Mauris lacinia lorem sit amet ipsum. Nunc quis urna dictum turpis accumsan semper.

Populärvetenskaplig sammanfattning på svenska

Lore ipsum dolor sit amet, consectetuer adipiscing elit. Etiam lobortis facilisis sem. Nullam nec mi et neque pharetra sollicitudin. Praesent imperdiet mi nec ante. Donec ullamcorper, felis non sodales commodo, lectus velit ultrices augue, a dignissim nibh lectus placerat pede. Vivamus nunc nunc, molestie ut, ultricies vel, semper in, velit. Ut porttitor. Praesent in sapien. Lore ipsum dolor sit amet, consectetuer adipiscing elit. Duis fringilla tristique neque. Sed interdum libero ut metus. Pellentesque place-
rat. Nam rutrum augue a leo. Morbi sed elit sit amet ante lobortis sollicitudin. Prae-
sent blandit blandit mauris. Praesent lectus tellus, aliquet aliquam, luctus a, egestas a,
turpis. Mauris lacinia lorem sit amet ipsum. Nunc quis urna dictum turpis accumsan
semper.

Production of strangeness in partonic interaction at the LHC

Part I

Fundamental theory

Chapter I

Introduction to quantum chromodynamics

This chapter serves as an introduction to particle physics, QCD, and phenomenology of high energy QCD interactions, with the focus on multiple partonic interactions and string formations. Furthermore, it introduces the physics of QCD matter and the deconfinement of hadrons.

I.1 Standard Model of elementary particles

The Standard Model (SM) of particle physics is a set of theories describes *elementary* constituents of matter and their interactions via fundamental forces of the Universe. It has been formulated in the 1970s, combining frameworks of quantum field theory (QFT), gauge symmetries, and spontaneous symmetry breaking.

Matter particles in the SM are classified into two main categories: quarks and leptons. Quarks come in six flavours (*up, down, charm, strange, top, and bottom*) and form hadrons, i.e. *baryons* (qqq) and *mesons* ($q\bar{q}$). The lepton sector also comprises six flavours (*electron, muon, tau, and their corresponding neutrinos*). Quarks and leptons are fermions with an intrinsic spin $1/2$. Furthermore, matter particles in the SM also come with associated antiparticles, which have opposite quantum numbers but the same mass.

The interactions between matter particles in the SM are mediated by an exchange of gauge bosons. There are three fundamental forces in the SM, described by four types of vector bosons (ordered by their typical strength):

1. *Strong force*, mediated by the gluon.
2. *Electromagnetic force*, mediated by the photon.
3. *Weak force*, mediated by the massive bosons W^\pm and Z^0 .

Moreover, the interactions are associated with local gauge symmetries, which determine their mathematical structure. The symmetry group for the SM is $SU(3) \times SU(2) \times U(1)$, corresponding to the strong and the electroweak sector. [1]

In addition, the SM also includes the scalar Higgs boson, which is responsible for giving mass to other elementary particles. This is achieved via the Higgs mechanism [2, 3], which involves the spontaneous breaking of the electroweak symmetry in the early universe. The Higgs boson was discovered experimentally at the Large Hadron Collider (LHC) in 2012 by the ATLAS [4] and CMS [5] collaborations, confirming a key prediction of the SM.

Nevertheless, the SM has several limitations, including its inability to account for dark matter, explain why the particle masses span over several orders of magnitude, and the CP violation problem related to the observed matter-antimatter asymmetry in the Universe. These are actively investigated in Beyond Standard Model (BSM) theories.

Quarks

$2.2^{+0.5}_{-0.4} \text{ MeV}$	$1.28 \pm 0.03 \text{ GeV}/c^2$	$172.76 \text{ GeV}/c^2$
u <i>up</i> $+\frac{2}{3}e$	c <i>charm</i> $+\frac{2}{3}e$	t <i>top</i> $+\frac{2}{3}e$
1964 - GIM mechanism	1974 - J/ψ meson	1995 - Tevatron
$4.7^{+0.5}_{-0.4} \text{ MeV}/c^2$	$4.7^{+0.5}_{-0.4} \text{ MeV}/c^2$	$4.7^{+0.5}_{-0.4} \text{ MeV}/c^2$
d <i>down</i> $-\frac{1}{3}e$	s <i>strange</i> $-\frac{1}{3}e$	b <i>bottom</i> $-\frac{1}{3}e$
1964 - GIM mechanism	1964 - kaon decay	1977 - Upsilon meson

Leptons

$0.511 \text{ MeV}/c^2$	$105.66 \text{ MeV}/c^2$	$1.77686 \text{ GeV}/c^2$
e <i>electron</i> $-1e$	μ <i>muon</i> $-1e$	τ <i>tau</i> $-1e$
1895 - X-rays	1936 - cosmic ray	1975 - SLAC
$< 2.2 \text{ eV}/c^2$	$< 0.17 \text{ MeV}/c^2$	$< 18.2 \text{ MeV}/c^2$
ν_e <i>electron neutrino</i> 0	ν_μ <i>muon neutrino</i> 0	ν_τ <i>tau neutrino</i> 0
1956 - nuclear reactor	1962 - Brookhaven	2000 - Fermilab

Gauge Bosons

0	0	$80.379 \text{ GeV}/c^2$
γ <i>photon</i> 0	g <i>gluon</i> 0	W W^\pm $\pm 1e$
1900 - Max Planck's quanta	1979 - PETRA	1983 - UA1, UA2
$91.1876 \text{ GeV}/c^2$	$125.10 \text{ GeV}/c^2$	
Z Z^0 0	H <i>Higgs</i> 0	2012 - ATLAS, CMS
1983 - UA1, UA2		

Figure 1.1: Particle of the Standard Model, listed together with their mass, electric charge, and the year and means of discovery (going clockwise from the top). VALUES NEED TO BE FIXED.

1.2 Coordinate systems and kinematic observables

Particles in HEP processes are described by their Lorentz-invariant four-vectors, $\mathbf{x} = (ct, x, y, z)$ and $\mathbf{p} = (E/c, p_x, p_y, p_z) = (E/c, \vec{p}_T, p_z)$, where $|\vec{p}_T| \equiv \sqrt{p_x^2 + p_y^2}$. In LHC experiments, the coordinate system is defined such that the x -axis points in the direction of the centre of the LHC, and the z -axis points in the direction of the beam, as shown in Fig. 1.2. In addition to the standard Cartesian coordinates, two observables, φ (azimuthal angle) and η (pseudorapidity), are used to describe the position and momentum of particles relative to the interaction point, which is located at $x = y = z = 0$. Pseudorapidity is defined as a function of the polar angle θ , where

$$\eta = -\ln(\tan(\theta/2)) . \quad (1.1)$$

For high-momentum particles ($E \simeq pc$), pseudorapidity is an approximation of the rapidity relative to the beam, given by

$$y = \frac{1}{2} \ln \frac{E + p_z c}{E - p_z c} . \quad (1.2)$$

Rapidity is a convenient quantity to use because it transforms additively under Lorentz boosts, unlike velocity. In these coordinates, the following relations hold:

$$p_x = |\vec{p}_T| \cos \varphi, \quad p_y = |\vec{p}_T| \sin \varphi, \quad p_z = |\vec{p}| \sinh \eta . \quad (1.3)$$

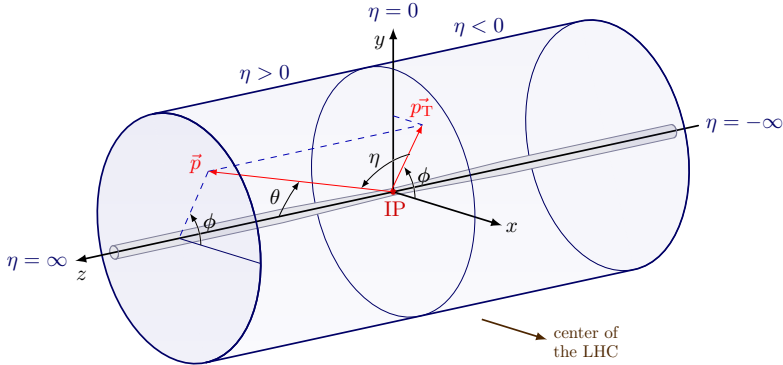


Figure 1.2: Coordinate system of an LHC experiment, with the interaction point in the centre.

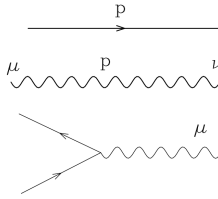
1.3 Quantum electrodynamics, electrons, and photons

In many aspects, QCD is a very similar theory to the simpler and better explored theory QED. In QFT, dynamics of particles can be provided in terms of its Lagrangian

density \mathcal{L} , from which equations of motions can be derived and which is also used to calculate interaction probabilities. The QED theory with a local U(1) symmetry has its \mathcal{L}_{QED} defined as:

$$\mathcal{L}_{\text{QED}} = \bar{\psi}(i\cancel{d} - m)\psi - \frac{1}{4}F_{\mu\nu}F^{\mu\nu} - e\bar{\psi}\cancel{A}\psi , \quad (1.4)$$

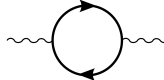
where ψ is the electron field with mass m and electric charge e , $F_{\mu\nu}$ the electromagnetic field-strength tensor, and Feynman slash notation is employed. The first part describes the dynamics of the electron fields, the second part describes the dynamics of the electromagnetic field, and the last part describes the interaction of electrons and photons with a coupling strength e . Using Feynman diagrams, they can be visualised as:



In QED interactions, each vertex depicted in the Feynman diagrams contributes to the probability of the process with a coefficient α (to the matrix elements as $\sqrt{\alpha}$, which is the coupling constant defined as $\alpha = e^2/4\pi$). This constant is generally small, which allows for interactions to be calculated using perturbation theory as an expansion series in α . The contributions to the series correspond to different Feynman diagrams representing the possible interaction processes, and they are ordered in powers of α based on the complexity of the diagrams.

Contributions from higher orders, such as the electron loop depicted below, lead to “screening” of the effective charge at large distances/small momenta, which makes the coupling constant dependent on the scale of the process μ . For example, at low energies corresponding to atomic scales, $\alpha \approx 1/137$, but at scales of the Z^0 boson mass, $\alpha \approx 1/127$ [6]. The *running* of this coupling is given by the β function, $\beta(\alpha) \equiv \frac{\partial \alpha}{\partial \log \mu^2}$, and it can be calculated by quantifying the effective coupling strengths at various orders of perturbation theory and using renormalisation group tools [7], although renormalisation is a more general concept. In QED, the screening leads to a positive sign in β calculated at lowest order, which means that when solving for α by integrating, α grows with energy scale¹.

¹The scale at which QED eventually breaks down due to this increase is well above the Planck mass.



Renormalisation is also used when calculating physical quantities where loop contributions lead to divergences, which are then absorbed into the parameters of the theory. The success of these procedures and the QED theory as a whole is validated by excellent prediction power for experimental measurements, such as the magnetic moment of an electron [8].

1.4 Quantum chromodynamics, quarks, and gluons

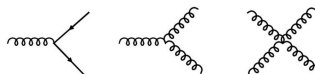
In QCD, particles have an additional quantum number called colour charge: red, green, and blue. Thus, there are three quarks of each flavour and eight gluons mediating interactions between. Gluons also carry colour charges, which allows them to interact with each other, making the theory non-Abelian. The QCD Lagrangian is symmetric under local SU(3) transformations and takes the shape of:

$$\mathcal{L}_{\text{QCD}} = \sum_f^{n_f} \bar{\psi}_i^{(f)} (iD_{ij}^\mu - m_f \delta_{ij}) \psi_j^{(f)} - \frac{1}{4} \sum_a^8 F_a^{\mu\nu} F_a^{\mu\nu} , \quad (1.5)$$

$$D_{ij}^\mu \equiv \partial^\mu \delta_{ij} + i g_s t_{ij}^a A_a^\mu , \quad (1.6)$$

$$F_{\mu\nu}^a \equiv \partial_\mu A_\nu^a - \partial_\nu A_\mu^a - g_s f_{abc} A_\mu^b A_\nu^c , \quad (1.7)$$

where ψ are the quark fields of n_f different flavours with mass m_f and colour i, j , D_{ij}^μ the covariant derivative with the coupling strength g_s and eight SU(3) generators given by matrices t_{ij}^a , and A_a^μ are the gluon fields [9]. Lastly, $F_{\mu\nu}^a$ is the field-strength tensor with f_{abc} being structure constants. The Lagrangian now also contains terms with interactions between gluons. In the representation of Feynman diagrams, for the interactions, there is:



Similarly to the QED case, the strong coupling constant can be defined as $\alpha_s = g^2/4\pi$. However, when considering its modifications due to virtual corrections, in addition to the quark loop, there is also a gluon loop.:



The gluon loop contributes to the β function in an opposite and larger way than the quark loop, and so overall, there is an *anti-screening* effect instead and a negative sign in the calculated one-loop β function. The running of the coupling can be calculated as:

$$\alpha_s(\mu) = \frac{1}{b_0 \log(\mu^2/\Lambda_{\text{QCD}}^2)} \quad , \quad (1.8)$$

where b_0 is a constant computed from the loop calculations, $b_0 = \frac{11 - \frac{2}{3} n_f}{4\pi}$ [10]. The introduced Λ_{QCD} is a scale parameter of the theory corresponding to the energy where the coupling becomes infinite, and depends on the definition of α_s and the number of available quark flavours n_f [9]. It ranges between 200 and 300 MeV/ c^2 [11].

From the running, it is evident that the coupling strength decreases with increasing energy, which is known as *asymptotic freedom* [10, 12] and corresponds to the fact that strong interaction is short-ranged. On the other hand, at low values, α_s diverges, which is related to the fact that quarks are bound to hadrons – *quark confinement*. The evolution of α_s also limits the applicability of perturbation theory at low energy regimes; calculations from perturbative QCD (pQCD) are relevant at leading orders starting typically from $1 - 2$ GeV/ c^2 . The measured $\alpha_s(\mu)$ is shown in Fig. 1.3, and at scales of the Z^0 boson mass is approximately 0.1185 ± 0.0006 [13, 14].

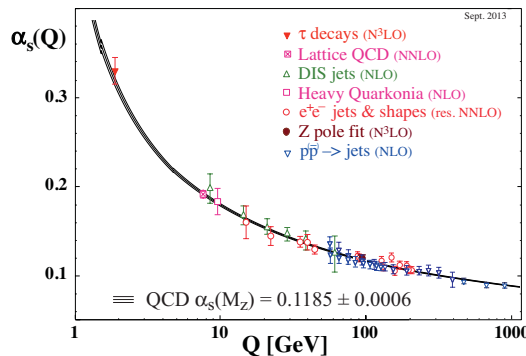


Figure 1.3: Strong coupling constant determined at different energy scales through various measurements and numerical calculations (data points) and compared with theoretical predictions from QCD. [13]

1.5 From partons to hadrons

1.5.1 Initial and Final State Radiation

In QFT, charged particles are surrounded by a cloud of virtual particles, which can be thought of as fluctuations in the particle's field. For example, the electron state can be described as a superposition of the bare electron plus additional massless bosons:

$$|e\rangle_{\text{phys}} = |e\rangle + |e\gamma\rangle + |e\gamma\gamma\rangle + \dots \quad (1.9)$$

and, at higher orders, pairs of virtual electrons. The fluctuations continuously form and recombine, with their lifetime depending on their energy and momentum. Specifically, the lifetime of a fluctuation with energy ω and transverse momentum k_T can be approximated as:

$$\tau \approx \frac{\omega}{k_T} \quad . \quad (1.10)$$

This implies that fluctuations with smaller- k_T live longer. [15]

As illustrated in Fig. 1.4, the coherent mixed state of the bare charge and the field fluctuations can be disturbed by the presence of an interaction. Intuitively, this interaction can change the energy and momentum of the fluctuations, their formation and recombination, and lead to the emission of radiation in two ways:

1. a fluctuation is kicked on-shell by the interaction and part of the field continues in its original direction, which leads to Initial State Radiation (ISR);
2. as a result of the field of the scattered particle rearranging itself, which can be a source of Final State Radiation (FSR).

In both of the cases, a larger momentum transfer implies more radiation. *For hard, wide angle emissions, cross sections can be calculated perturbatively at fixed orders.*

Soft and collinear emissions, however, lead to infra-red divergences ($\propto \frac{1}{\omega}, \propto \frac{1}{k_T^2}$) and thus, need to be factorised away from the amplitudes or the cross sections and then described using resummation techniques. Without any emissions, the probabilities of finding electrons and photons of fractional momentum x with respect to the whole system are:

$$f_e(x) = \delta(1 - x), \quad f_\gamma(x) = 0, \quad (1.11)$$

When considering the emissions above some scales parametrised by the resolution parameter Q^2 , these probabilities, however, evolve according to the DGLAP equation [16] :

$$\frac{\partial}{\partial \ln Q^2} \begin{pmatrix} f_e(x, Q^2) \\ f_\gamma(x, Q^2) \end{pmatrix} = \frac{\alpha_{\text{em}}}{2\pi} \int_x^1 \frac{dz}{z} \begin{pmatrix} P_{ee}(z) & P_{e\gamma}(z) \\ P_{\gamma e}(z) & P_{\gamma\gamma}(z) \end{pmatrix} \begin{pmatrix} f_e\left(\frac{x}{z}, Q^2\right) \\ f_\gamma\left(\frac{x}{z}, Q^2\right) \end{pmatrix}, \quad (1.12)$$

where $P_{ij}(z)$ are the splitting probability functions of a particle i emitting a particle j .

In QCD, the behaviour is analogous, with $\alpha_{\text{em}} \rightarrow \alpha_s$, $e \rightarrow q$, and $\gamma \rightarrow g$. [15]

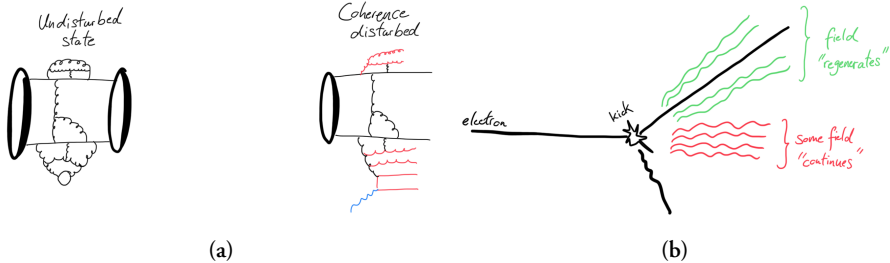


Figure 1.4: (a) Illustration of the field fluctuations before and after the state coherence gets disturbed by an external actor. (b) Illustration of emmisions of radiation in a scattering process.

1.5.2 Factorisation theorem

The evolution equation (1.12) implies that the probabilities of observing emissions with a fractional momentum x depend on the resolution Q^2 . In QCD,

1. when applied to the initial state, they are known as parton distribution functions (PDFs) and determine the probabilities of finding partons² in the composite hadronic state.
2. When applied to the final state, they are called fragmentation functions, and determine the probabilities of measuring fragments of the outgoing particles.

This leads to the factorisation theorem [17] for processes involving collisions of two hadrons, which separates the perturbatively calculable partonic cross section from

²Partons refer to the valence quarks, sea quarks, and gluons inside hadrons.

the non-perturbative partonic evolution and hadronisation. The theorem can be expressed as follows:

$$\sigma = f_i^A(x_i, \mu_F) f_j^B(x_j, \mu_F) \otimes \hat{\sigma}_{ij \rightarrow n}(\mu_F, \mu_R) \otimes D_{n \rightarrow n'} . \quad (1.13)$$

Here, i and j are the initial partons, $\hat{\sigma}_{ij \rightarrow n}$ is the partonic cross section, $D_{n \rightarrow n'}$ is the process-specific fragmentation function for evolving the partons n into the particles' final state n' , and μ_F and μ_R are the factorisation and renormalisation scales, respectively. The factorisation scale, μ_F , determines the scale below which the emissions are absorbed into the PDFs. The theorem is depicted in Fig. 1.5.

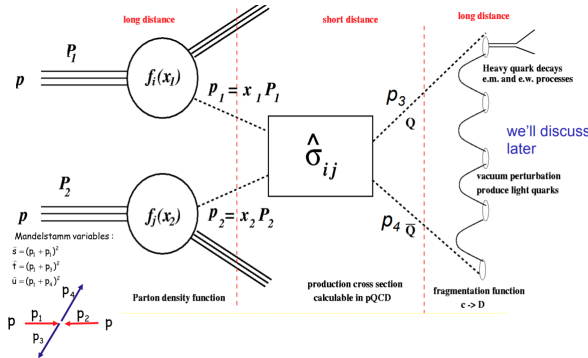


Figure 1.5: Illustration of the factorisation theorem. (NEEDS TO BE REMADE).

1.5.3 Parton distribution functions

The PDFs defining the probabilities of finding quarks and gluons in nucleons can be determined experimentally at hadron-electron colliders such as HERA [18]. They are determined from measurements of deep inelastic scatterings in a range of energies and momentum transfers. They are displayed in Fig. 1.6 as a function of the fractional momentum x (also called Björken x).

According to collider kinematics, $x \propto \frac{1}{\sqrt{s_{\text{c}}y}}$, therefore, the partonic composition of ultra-relativistic hadrons is dominated by gluons. Following unitarity principles and BK evolution equation [19], it is expected that gluons start recombining and the gluonic content saturates as $x \rightarrow 0$. This is actively researched [20], however, not directly measured yet. Additionally, it should be noted that in ultra-relativistic heavy nuclei, the partons are modified in the contracted nuclear environment and the PDFs are referred to as nPDFs.

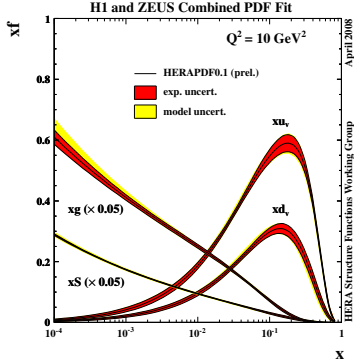


Figure 1.6: Parton distribution functions determined in ep scatterings at HERA as a function of the fractional momentum for the up, down, sea quarks, and gluons. [18]

1.5.4 Parton fragmentation and the Lund string

After the scattering process, the produced partons continue to fragment by emitting more partons in a process called the parton shower. Since the coupling strength in QCD increases with decreasing the energy scale of the splitting, this leads to the production of many soft, collimated emissions known as jets. The partonic evolution continues until the virtuality of the partons reaches the hadronization scale ($\approx \Lambda_{\text{QCD}}$). There are multiple frameworks within QCD to describe the evolution of partons into their final state, such as using the DGLAP equations or the so-called dipole formalism.

Once the partonic final state is reached, the partons hadronise into the observable mesons and baryons. The hadronisation process is not calculable in QCD and requires phenomenological models to describe it. One such model is the Lund string model [21], which describes hadronisation as the breaking of a color string between the quarks in the final state. In this model, the energy stored in the color string is converted into the mass of new hadrons.

According to confinement, hadronisation should involve at least two partons with complementary colours. In QCD, the $q\bar{q}$ potential takes the shape of

$$V_{q\bar{q}} \approx -\frac{4}{3} \frac{\alpha_s \hbar c}{r} + \kappa r \quad , \quad (1.14)$$

where κ is a parameter with value around 1 GeV/fm . In the non-perturbative regime (long distances), the potential is dominated by the linear part, which is reminiscent of a system bound by a string with tension κ . This is taken advantage of by the Lund string model – a q and \bar{q} pair separated by distance Δx is bound by a color field (string) with energy $\kappa \Delta x$.

If the q and \bar{q} continue separating as a result of the scattering, the energy stored in the color field increases. At some point, it can become energetically favourable to produce a new $q\bar{q}$ pair out of vacuum, which is a quantum mechanics tunnelling phenomenon characterised by the probability:

$$\frac{dP}{dm_T} \propto \exp\left(-\frac{\pi m_T^2}{\kappa}\right) , \quad (1.15)$$

where m_T is the transverse mass of the produced quarks. Otherwise, the $q\bar{q}$ system starts contracting and oscillates with a period $T = 2E_{\text{kin}}/\kappa$, where E_{kin} is its maximum kinetic energy. The produced q and \bar{q} then connect by new color fields to the original pair. This process repeats itself resulting in a cascade of many $q\bar{q}$ pairs connected by many color strings. In this description, baryons can also be created by double tunnelling of a $qq\bar{q}\bar{q}$ pair. The process is illustrated in Fig. 1.7.

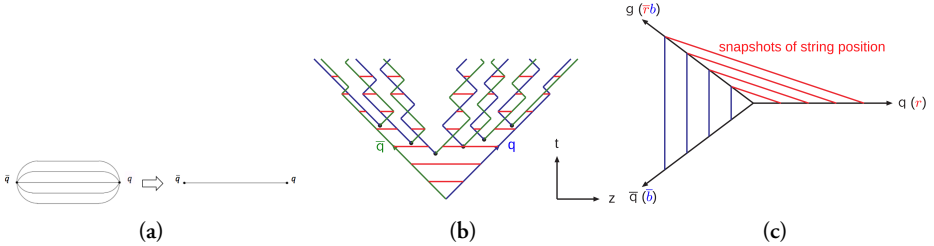


Figure 1.7: (a) Illustration of the color field between two quarks and its simplified representation with a string [21]. (b) Illustration of the string splitting by producing new $q\bar{q}$ in the $t - z$ plane [21]. (c) Visualisation of the treatment of gluons in the Lund string model [22].

Equation 1.15 also implies that production of strange quarks is suppressed by a factor of

$$\rho = \exp\left(-\frac{\pi(m_s^2 - m_{u,d}^2)}{\kappa}\right) . \quad (1.16)$$

This parameter is typically tuned to data, as substituting constituent ($m_s \approx 0.5 \text{ GeV}/c^2$, $m_{u,d} \approx 0.33 \text{ GeV}/c^2$) versus current masses ($m_s \approx 0.1 \text{ GeV}/c^2$, $m_{u,d} \approx 0$) leads to considerable differences underestimating and overestimating data, respectively.

For a $q\bar{q}g$ system, in this model, the gluon connects to the quark and antiquark and is effectively treated as a “kink” on the color field, adding energy and momentum to the $q\bar{q}$ string (stretching it in its direction), as visualised in Fig. 1.7.

It should be noted that in the paradigm of AA collisions, hadron production can be alternatively modelled by hadronisation at the QGP’s phase boundary by *coalescing* free quarks.

1.6 Multiple partonic interactions

Results from Sp \bar{p} S in the 1980s sparked motivations for considering interactions of multiple partons between the two composite protons. For example, the AFS experiment observed an abundance of 4-jet events, displayed in Fig. 1.8, that could not be explained by calculations considering a double gluon bremsstrahlung from a single partonic scattering[23]. Furthermore, UA5 measurements studying energy dependence of multiplicity distributions $P(N_{\text{ch}})$ saw the so-called KNO scaling[24], where $P(N_{\text{ch}})/\langle N_{\text{ch}} \rangle$ does not depend on energy, but revealed a broadening in high-multiplicity events with increasing \sqrt{s} [25, 26], which was not reproducible in the context of N_{ch} being produced from a single string [27]. This further suggested the presence of multiple production sources.

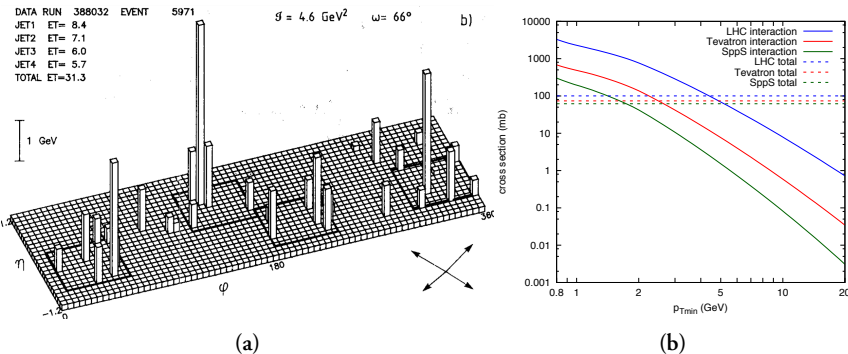


Figure 1.8: (a) Event display of an event with a 4-jet, where the pillars correspond to transverse energy deposits. [23] (b) Dependence of the integrated parton-parton cross section on the cutoff parameter $k_{\perp\min}$ for Sp \bar{p} S at $\sqrt{s} = 0.63$ TeV, Tevatron at $\sqrt{s} = 1.96$ TeV, and the LHC at $\sqrt{s} = 13$ TeV, modelled with Pythia. [27]

These findings prompted further development of Regge theory and approaches that incorporated multiple pomerons, which were successful in describing the N_{ch} distributions. However, this approach is fully decoupled from descriptions of the perturbative primary scattering. Subsequently, much of the phenomenology related to multiple partonic interactions was developed within the framework of the Pythia MC event generator, which is discussed individually in Chapter ?? [27]. However, nowadays, the relevance of the concept of MPIs in hadronic collisions extends beyond this generator. A scattering with double partonic interactions is illustrated in Fig. 1.9.

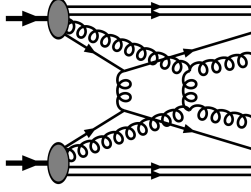


Figure 1.9: Diagram showing a double partonic interaction, a case of $n_{\text{MPI}} = 2$. [15]

In the Pythia approach, MPI are treated as additional perturbative scatterings. In QCD, the $2 \rightarrow 2$ cross section (dominated by the gluon exchange t-channel) diverges as $\propto \alpha_S^2(k_\perp^2)/k_\perp^4$, so a cutoff parameter $k_{\perp\min}$ must be introduced, and using (??) leads to:

$$\frac{d\sigma}{dk_\perp^2} = \sum_{ij} \int dx_1 dx_2 f_i(x_1, \mu_F^2) f_j(x_2, \mu_F^2) \frac{d\hat{\sigma}_{ij}^H}{dk_\perp^2}, \quad (1.17)$$

$$\sigma_{\text{int}}(k_{\perp\min}) = \int_{k_{\perp\min}^2}^{s/4} \frac{d\sigma}{dk_\perp^2} dk_\perp^2. \quad (1.18)$$

The choice of cutoff can be tuned to experimental data, and for the SppS energy of $\sqrt{s} = 630$ GeV, a value of around 1.6 GeV/c was typical [27]. The dependence of this parton-parton scattering cross section is shown in Fig. 1.8.

The total pp cross-section, which is on the order of 100 mb at $\sqrt{s} = 13$ TeV, is given by

$$\sigma_{\text{pp}} = \sigma_{\text{elastic}} + \sigma_{\text{single dif.}} + \sigma_{\text{double dif.}} + \sigma_{\text{non-dif.}}, \quad (1.19)$$

where the inelastic cross sections $\sigma_{\text{inel}} \approx \sigma_{\text{double dif.}} + \sigma_{\text{non-dif.}}$ corresponds to approximately 60% of the total. The mean number of MPIs, $\langle n_{\text{MPI}} \rangle$, can be estimated using:

$$\langle n_{\text{MPI}} \rangle(k_{\perp\min}) = \frac{\sigma_{\text{int}}(k_{\perp\min})}{\sigma_{\text{inel}}} \quad (1.20)$$

However, the actual treatment is more complex and involves considerations of other parameters such as the dampening factor k_\perp^0 to account for the confinement nature of partons, modifications of multiparton PDFs, energy-momentum conservation effects, x -dependent source geometry, and the intertwinedness of partonic evolutions.

In summary, MPIs represent several subcollisions that take place in an average pp collision with p_T scales of a few GeV. They are colour-connected to the beam remnants, which in the Lund model are represented by strings. Since a string with

$\kappa = 1 \text{ GeV/fm}$ yields, as a rule of thumb, approximately one hadron per unit rapidity, and the average pp collision at the LHC at $\sqrt{s} = 13 \text{ TeV}$ has $\langle dN_{\text{ch}}/dy \rangle \approx 6$, the typical number of partonic interactions is around six [27].

Finally, the observation of QGP-like phenomena in pp collisions at the LHC has renewed interest in MPI phenomenology, as discussed in the following chapter. Such observations do not contradict the concept of MPIs; rather, they suggest the possibility of incorporating collective behavior among the MPIs, such as interactions between strings, local modifications of string tensions, or, alternatively, the formation of a multipartonic state with QGP-like properties.

1.6.1 Color reconnection

The incorporation of MPIs improved the description of the N_{ch} distributions and their dependence on \sqrt{n} . However, there were also observations of $\langle p_{\text{T}} \rangle (N_{\text{ch}})$ increasing as a function of N_{ch} , which could not be explained. More MPIs lead to more strings, which in turn leads to the production of more particles, but the p_{T} is mostly unaffected. This would predict a weaker dependence of $\langle p_{\text{T}} \rangle$ on N_{ch} , contrary to the data [27]. The issue was resolved by implementing a possible color reconnection mechanism, which rearranges the color fields between partons.

TBA Insert diagrams of the processes!

One can envision the following process:

$$e^+ e^- \rightarrow W^+ W^- \rightarrow q_1 \bar{q}_2 q_3 \bar{q}_4.$$

In this scenario, a color reconnection mechanism could rearrange the colour-connected $q_1 \bar{q}_2$ and $q_3 \bar{q}_4$ into $q_1 \bar{q}_4$ and $q_3 \bar{q}_2$ if it were energetically favourable, depending on the phase-space configurations. Measurements at LEP [28] of this process have indeed shown that such final-state corrections must be taken into account to explain the data on W masses and widths. They also reported that the reconnection probabilities for such events are on the order of 50%, further indicating that colour reconnection is an important factor to consider.

Pythia implements CR by minimizing the total length of strings in the system, analogous to minimising potential energy [29]. This mechanism, illustrated in Fig. 1.10, explains the rising trend of $\langle p_{\text{T}} \rangle$ as a function of N_{ch} : shorter strings imply fewer hadrons to split the transverse boost across, and the more MPI, the bigger this effect. Moreover, CR also helped describe the absolute value of $\langle p_{\text{T}} \rangle$. With this approach, no further modifications of fragmentation parameters were necessary, in line with the concept of jet universality. However, it should be noted that there are various CR implementations and all rely on parameters obtained from tuning to data.

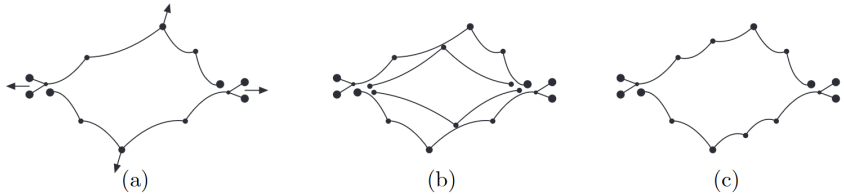


Figure 1.10: Depiction of the CR process: **(a)** in a hard parton subcollision, the outgoing gluons are connected to the beam remnants through colour. Additional gluon kinks may occur through initial state radiation, which are ordered by rapidity. **(b)** A second hard scattering should theoretically result in two new strings connected to the remnants. **(c)** In order to minimise the total string length, gluons are colour reconnected. [30]

It is also worth noting that the p_T boost acquired through color reconnection may depend on mass and whether a hadron is a baryon or meson, which somewhat mimics the hydrodynamic signatures of collective flow observed in AA collisions [31].

1.7 Underlying event

The underlying event (UE) in high-energy collisions refers to the additional hadronic activity that accompanies the primary hard scattering process, but is not directly related to it. This includes the fragmentation products of the beam remnants, ISR and FSR, as well as the effects of the previously discussed MPIs, and is visualised in Fig. 1.11. The UE (with its name coined at Tevatron [32]) is typically characterized by a distribution of softer particles around and far outside of the hard process and was first observed at Sp \bar{p} S in the 1980s [33]. These measurements saw a constant plateau of transverse energy E_T outside of the jet core, with its height independent of the jet energy.

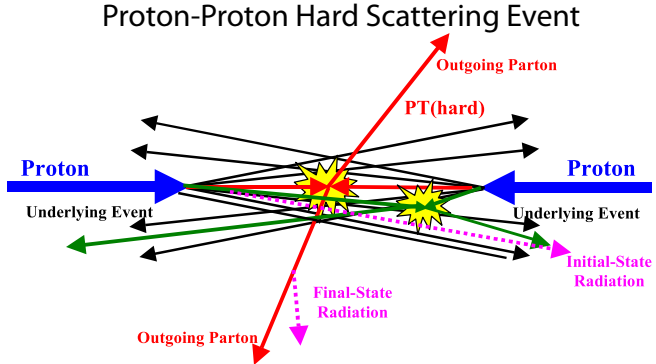


Figure 1.11: Cartoon illustrating a pp collision and its components: the hard scattering process, beam remnants, initial/final state radiation, and the MPIs. The last three contribute to the underlying event. [32, 34]

It is important to note that particle production in UE is different from the MB production, as it is biased by the presence of hard scattering. Additionally, the magnitude of the UE can fluctuate significantly from event to event.

1.8 From hadrons to partons: deconfined QCD matter

A simple argument can be made that confinement of quarks inside hadrons cannot be sustained when the density of partons is too large compared to that inside ordinary hadrons. Or alternatively, when the partonic kinetic energies are much larger than the confining part of the $q\bar{q}$ potential in (1.14). The following sections introduce some theoretical frameworks predicting the deconfinement of quarks and gluons. The calculations presented use natural units ($\hbar = c = k_B = 1$).

1.8.1 Bag model of hadrons

In this very naive approach [35, 36], hadrons are treated as spherical cavities (“bags”) with radius R of free massless quarks. These cavities exist in the non-perturbative QCD vacuum, which exerts a confining pressure B . The lowest-energy solution of the Dirac equation for the quarks, which in this case is $\not{p}\psi = 0$, is the $s_{1/2}$ -state given by:

$$\psi(r, t) = N \begin{pmatrix} j_0(\omega r)U \\ i\sigma \cdot \hat{r} j_1(\omega r)U \end{pmatrix} \exp(-i\omega t) , \quad (1.21)$$

where N is a normalisation constant, j_0 and j_1 are spherical Bessel functions, ω is the quark energy, and U the two-component spinor. The assumption that quarks are confined within the cavity volume represents the boundary conditions that the quark scalar density $\psi\bar{\psi}$ becomes zero at $r = R$, which is equivalent to $j_0(\omega R) = j_1(\omega R)$:

$$\hat{j}_0^2(\omega R) - \vec{\sigma} \cdot \hat{r} \vec{\sigma} \cdot \hat{r} j_1^2(\omega R) = 0 \quad (1.22)$$

$$j_0(\omega R) = j_1(\omega R) , \quad (1.23)$$

which happens when $\omega \approx \frac{2.04}{R}$. Thus, energy of the system can be given by

$$E(R) \approx n_q \cdot \frac{2.04}{R} + \frac{4\pi}{3} BR^3 . \quad (1.24)$$

Here, the first term represents the kinetic energy of n_q quarks in the cavity and second term is the cavity volume energy. Gluon solutions should also be considered but are neglected in this approach. The first term acts to expand the cavity, whereas the second term acts to contract it. Finding an optimum of this energy with respect to R leads to

$$B^{1/4} \approx \left(\frac{2.04n_q}{4\pi} \right)^{1/4} \frac{1}{R} . \quad (1.25)$$

Finally, assuming values for a proton, $R \approx 0.8$ fm, and three valence quarks $n_q = 3$, the confining pressure can be approximated as $B^{1/4} \approx 206$ MeV. [35]

To relate the confining pressure to a critical temperature at which deconfinement occurs, T_c , one can assume a gas of relativistic massless fermions and bosons with energy density ρ [37?]. Using Stefan-Boltzmann law, the equation of state is,

$$P = \frac{1}{3}(d_b + \frac{7}{8}d_f)\rho = (d_b + \frac{7}{8}d_f)\frac{\pi^2}{90}T^4 \quad (1.26)$$

where d_b and d_f are the degeneracy numbers for bosons and fermions, in this case gluons and quarks, respectively. Summing together possible colours, polarisations, and flavours for particles and antiparticles, one gets $d_b = 16$ and $d_f = 24$. Inserting the cavity pressure B value calculated in (1.25), T_c can be estimated as approximately 145 MeV.

1.8.2 Lattice QCD

Lattice QCD (LQCD) is a technique allowing calculation of processes involving the strong interaction in the non-perturbative regime, from first principles, without phenomenological assumptions. In this approach, the space-time continuum is discretised into a four-dimensional lattice, which allows QCD path integrals to be solved

numerically. Smallest squares on the lattice are called *plaquettes*, with the lattice links representing gluon fields and lattice sites representing quark fields. [38]

Lattice calculations are computationally extremely intensive³, thus, a sufficiently coarse lattice spacing must be chosen to reduce computational costs and make the approach feasible. Often, simulations are also performed with unphysical quark masses (e.g. $m_q \sim m_\pi$), for the same reason. The results are then extrapolated using highly complex methods. Another limitation in LQCD is the so-called *sign problem*, discussed in detail for instance in Ref. [40], which arises when evaluating highly oscillatory complex integrals in finite-density environment.

Despite its challenges, LQCD has been successful in various predictions, notably, the *ab initio* calculation of the mass of neutron (uud) using the mass of Ω (sss) as an input [41]. Furthermore, it allows for the calculation of thermodynamics of QCD matter and predicts its equation of state, as well as a phase transition at $T_c \approx 150$ MeV [42, 43], which is usually identified with the formation of quark-gluon plasma QGP, discussed in Chapter ???. The dependence of energy density and pressure on temperature can be seen in Fig. 1.12.

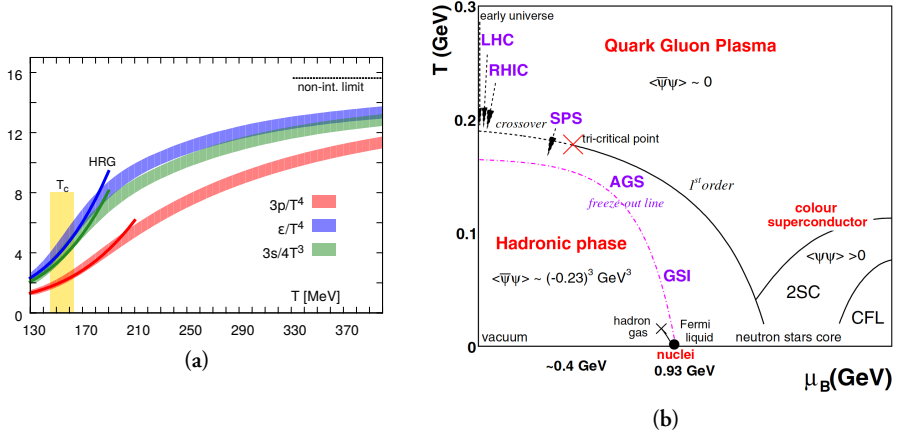


Figure 1.12: (a) Dependence of the pressure (red), energy density (blue), and entropy density (green) on temperature, determined with LQCD. [43] (b) Phase diagram of QCD matter. [44]

1.8.3 QCD phase diagram, chiral symmetry restoration

Phase transitions of QCD matter are investigated to explore the QCD phase diagram with respect to temperature T and baryon chemical potential μ_B , which corresponds

³In fact, in the past, LQCD was among important drivers of the advancement of GPU computing and it is also used as benchmark in high-performance computing [39].

to net baryon density. Figure 1.12 visualizes the different areas of the QCD phase diagram probed by various experiments [44]. Measurements of Pb-Pb collisions at the LHC access high T and almost zero μ_B , as the nucleons of ultrarelativistic Pb nuclei escape the interaction volume before the plasma develops, and the high energy subsequently leads to a sizable baryon production balanced by anti-baryons due to conservation laws. Experiments studying collisions of slower and heavier nuclei reach higher μ_B regions.

Furthermore, looking back at the QCD Lagrangian in (1.5) and neglecting quark current masses $m_{u,d} \rightarrow 0$, it can be seen that it is invariant when switching the up and the down quark, corresponding to a SU(2) isospin symmetry. This allows the fermion fields to be rewritten in terms of their left and right chiralities and the QCD Lagrangian then exhibits a larger *chiral symmetry*.

However, it is known that the vacuum expectation value of a $q\bar{q}$ state is much larger than the current masses $m_{u,d}$:

$$\langle 0 | q\bar{q} | 0 \rangle = \langle 0 | u\bar{u} + d\bar{d} | 0 \rangle \approx (250 \text{ MeV})^3 \quad , \quad (1.27)$$

where the value is taken from average masses of light flavour mesons. This means that the QCD vacuum spontaneously breaks the chiral symmetry. [45]

It can be expected that in the plasma of deconfined quarks and gluons, chiral symmetry is *restored* [46, 47]. This is actively studied in AA collisions, for example in searches of the so-called chiral magnetic effect [48] or degeneracy of normally chiral partners [49], such as the ρ ($J^P = 1^-$) and a_1 ($J^P = 1^+$) states.

Chapter 2

QCD phenomena in high energy hadronic collisions

The aim of this chapter is to give an introduction to the physics of heavy ions and the various phenomena related with the quark-gluon plasma QGP. Furthermore, a detailed summary of the findings of QGP phenomena in small systems, i.e. pp and pA collisions, is given. Lastly, some Monte Carlo event generators based on phenomenological modelling of hadronic collisions relevant to this dissertation are summarised.

2.1 Collisions of heavy nuclei

2.1.1 Collision geometry, centrality, multiplicity

Collisions of heavy nuclei, composed of many fluctuating nucleons, may occur under various initial state configurations. Some quantities used to describe them are the impact parameter b , defined as the distance between the two nuclei centers, number of participating (scattered) nucleons N_{part} , and the number of binary nucleonic collisions N_{coll} .

Determining these quantities is important because:

1. Soft processes, such as light flavor particle production, are expected to scale with the interaction volume, which $\propto N_{\text{part}}$.
2. Hard processes, such as jet and heavy flavor production, are expected to scale with the number of large momentum transfer interactions given by N_{coll} .

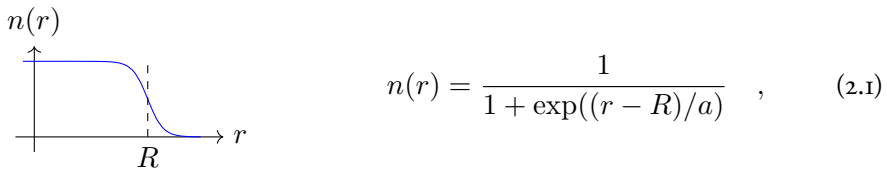
3. b , disregarding the fluctuations of nucleonic positions, defines the shape and anisotropy of the overlap region, which are important initial state conditions.

Since these quantities cannot be directly measured, they need to be modelled. The charged particle *multiplicity* is commonly used for this purpose, as $\langle N_{\text{ch}} \rangle$ increases monotonically with N_{part} , N_{coll} , and decreasing b . Multiplicity N_{ch} can be measured experimentally, e.g. with tracking detectors. The concept of *centrality* is also used, which is defined as quantiles of the total nuclear cross-section. For example, a centrality of 0 – 5% refers to low b values and the top 5% of N_{ch} values (central events), while 95 – 100% centrality refers to high b values and the bottom 5% of N_{ch} values (peripheral events). Centrality can also be inferred from other *event activity* classifiers, such as amplitudes of scintillators at forward rapidity, transverse energy in calorimeters, or energy from beam remnants in zero-degree-calorimeters.

In AA collisions, these relationships are well-defined, and thus the models perform well. The most popular model is the MC Glauber model [50]. Other models include MC-KLN [51] and IP Glasma [52].

2.1.2 MC Glauber model

The MC Glauber model [50] takes on a very simple albeit powerful approach. The two nuclei are simulated in three dimensions in a way that satisfies their respective nuclear density profiles, usually modelled by sampling the positions of nucleons from the Woods-Saxon distribution:



where R is the nuclear radius and a the nuclear skin thickness.

The nucleonic densities can be represented by uniform disks, or more accurately by Fermi-distributions or Gaussian profiles to account for fluctuations of their densities. Their parameters are left free and are tuned to the data.

A random impact parameter is then chosen or sampled. The collision is then treated as a sequence of independent binary nucleon-nucleon collisions, where

- i. nucleons remain travelling in straight lines,

2. the inelastic nucleon-nucleon cross section σ_{NN} does not depend on the number of interactions,
3. two nucleons are considered to interact if their transverse relative distance $d \leq \sqrt{\sigma_{\text{NN}}/\pi}$.

Figure 2.1 illustrates an example of a Glauber Monte Carlo event for a Au+Au collision. By simulating numerous collisions, the average N_{part} and N_{coll} are determined¹, and their relations to centrality and event activity observables are determined by fitting to experimental data.

Recent studies have extended the MC Glauber model to include sub-nucleonic structures. Such efforts show that the production of charged hadrons at mid-rapidity scales linearly with the number of participating partons. Comparisons with LHC data at $\sqrt{s_{\text{NN}}} = 5.02 \text{ TeV}$ suggest that the number of sub-nucleonic degrees of freedom ranges from 3 to 5 [53].

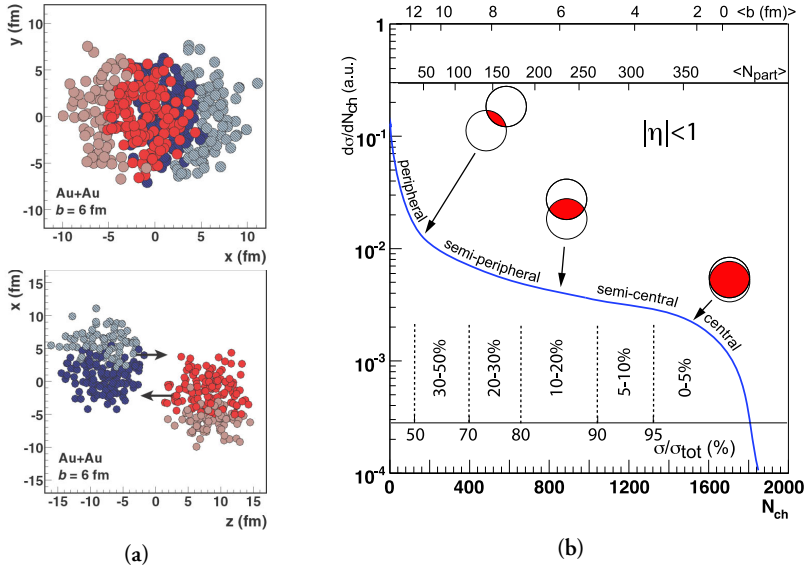


Figure 2.1: (a) Glauber Monte Carlo event of a Au+Au collision at $\sqrt{s_{\text{NN}}} = 200 \text{ GeV}$ shown in the transverse plane (top panel) and along the beam axis z (bottom panel). The darker circles represent participating nuclei and their area corresponds to σ_{NN} . (b) Illustrative diagram of the dependence of final-state event multiplicity on the initial-state quantities, number of participants N_{part} and impact parameter b . [50]

¹It also shows the scaling between the numbers of participants and binary collisions, which is approximately $N_{\text{coll}} \approx 0.35 N_{\text{part}}^{4/3}$.

2.2 Quark-gluon plasma

In agreement with lattice QCD predictions [54], the QGP has been measured in ultra-relativistic collisions of heavy nuclei at RHIC [55, 56], LHC [57], and even SPS [58]. Although it cannot be observed directly, a wealth of evidence from three decades of research combining various observables reveals the effects of the produced QGP medium. Whilst somewhat context-dependent, the following features make QGP the most extreme phenomenon observed in terms of its:

- *Temperature*: QGP temperatures reach values on the order of hundreds of MeV, which corresponds to approximately 2×10^{12} K.² [59]
- *Viscosity*: the shear viscosity to entropy density ratio η/s reaches the minimum quantum limit of $1/4\pi$ (for water at room temperature, $\eta/s \approx 8$), making it an almost perfect liquid. [44]
- *Vorticity*: in semi-peripheral collisions, the rotating plasma reaches a vorticity of approximately $9 \times 10^{21} \text{ s}^{-1}$. [60]
- *Magnetic field*: in non-central collisions, the magnetic fields in the system may peak at $\sim 10^{19}$ T. [61]

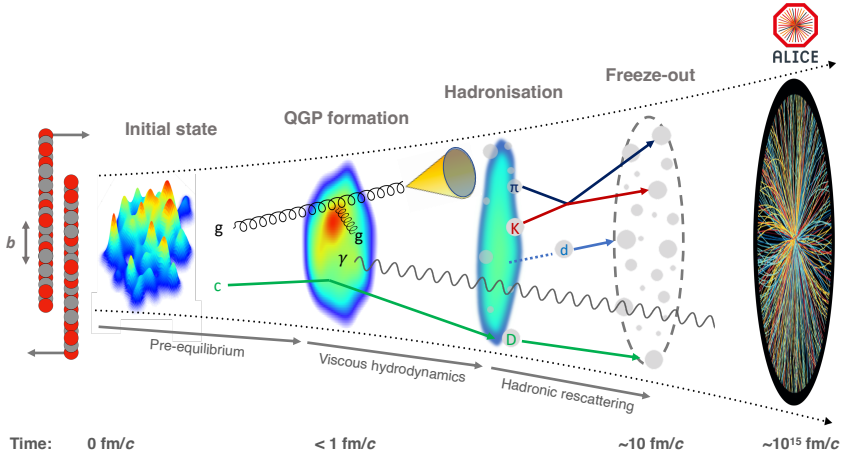


Figure 2.2: Evolution of heavy nuclei collisions at LHC energies, depicting the different stages. [62]

²Contrasting some of the lowest temperatures required for the super-conducting magnets of the LHC, $T \approx 1.9$ K.

Figure 2.2 illustrates the common paradigm for the different stages of a collision between heavy nuclei:

1. The Lorentz-contracted heavy nuclei approach each other at ultra-relativistic speeds.
2. *Pre-hydrodynamisation stage* ($\tau \equiv \sqrt{t^2 - z^2} \leq 1$ fm/c): “hard” particles are produced in scatterings with the highest momentum transfer Q^2 . Produced matter expands rapidly in the longitudinal direction and starts expanding in the radial direction.
3. *Hydrodynamisation* ($1 \leq \tau \leq 10$ fm/c): abundantly produced partons create a deconfined medium, which can be described by hydrodynamic equations.
4. *Chemical freeze-out* ($\tau \sim 10$ fm/c): the system cools down and hadronises. The produced hadrons then stop interacting inelastically and the system’s chemical content is stabilised.
5. *Kinetic freeze-out* ($\tau \lesssim 20$ fm/c): hadrons no longer interact elastically and their kinematics stabilize.
6. Long-lived particles can be measured in the detector volume.

The following subsections outline some of the essential phenomena related to the production of QGP.

2.2.1 Quarkonium dissociation and sequential suppression

Heavy quarkonia are vector meson states consisting of $c\bar{c}$ and $b\bar{b}$. They include J/ψ , $\psi(2S)$, $\Upsilon(1S)$, $\Upsilon(2S)$, $\Upsilon(3S)$, which can be relatively easily measured in LHC experiments via their di-lepton decay channels. They are created solely in the first phases of the collision and then experience the entire evolution of the QGP medium:

$$t_{\text{creation}}^{Q\bar{Q}} < t_{\text{creation}}^{\text{QGP}} < t_{\text{lifetime}}^{\text{QGP}} \ll t_{\text{lifetime}}^{Q\bar{Q}} . \quad (2.2)$$

Additionally, due to their large binding energies, their radii may remain smaller than the plasma screening radius $r_D(T)$, and thus, survive the dissociation. For instance, considering their in-vacuum radii determined from the $q\bar{q}$ potential, $r_{\Upsilon(1S)} \sim 0.14$ fm, $r_{\Upsilon(2S)} \sim 0.28$ fm, $r_{\Upsilon(3S)} \sim 0.39$ fm, which contrast the $r_\pi \sim 0.7$ fm [63]. This implies that different temperatures result in the dissociation of different states, and measuring the production of different states can help infer the QGP temperature, as illustrated in Fig. 2.3 [64, 65].

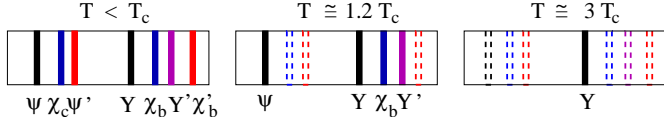


Figure 2.3: Spectral lines corresponding to various charmonium and bottomonium states for different medium temperatures , relative to the QGP critical temperature. [65]

The production of heavy quarkonia in AA collisions is compared to that in pp collisions (scaled by the average number of binary collisions) through the nuclear modification factor, R_{AA} . This quantity is widely used in various other measurements and is defined as:

$$R_{AA} = \frac{dN_{AA}/dp_T}{\langle N_{coll} \rangle dN_{pp}/dp_T} . \quad (2.3)$$

R_{AA} can take on the following values:

1. $R_{AA} = 1$: The result one would expect if the AA collision is a mere superposition of nucleon-nucleon collisions. There is no net effect on the production, corresponding to the absence of the QGP medium and other nuclear effects, or their mutual cancellation.
2. $R_{AA} < 1$: The production is overall suppressed, for example, due to dissociation.
3. $R_{AA} > 1$: The plasma and nuclear effects systematically enhance the measured production.

At LHC energies, the abundance of charm quarks in the QGP is high enough that charmonia can be formed after dissociation, which somewhat complicates the interpretation of charmonia suppression. However, the $\Upsilon(3S)$ bottomonium has R_{AA} consistent with zero at $\sqrt{s_{NN}} = 5.02$ TeV, as shown in Fig. 2.4 [59]. This complete suppression is a clear signature of the QGP and can be used together with models to estimate the QGP temperature at these energies as $T \approx 630$ MeV [66].

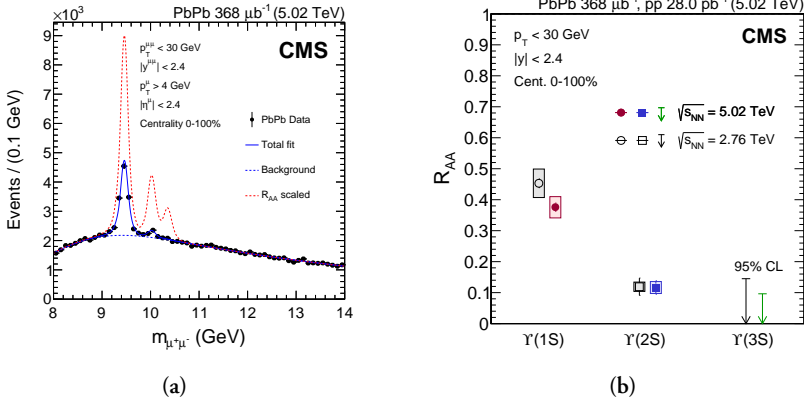


Figure 2.4: (a) Muon invariant mass distributions in Pb-Pb collisions at $\sqrt{s_{NN}} = 5.02$ TeV, also showing a scaled result from pp collisions at same energies (red dashed line). (b) Nuclear modification factors of the three bottomonium states. [59]

2.2.2 Strangeness enhancement

In the production of hadrons in vacuum, strangeness is suppressed relatively to light quarks not only due to the higher mass of the strange quark ($m_s \approx 0.1 \text{ GeV}/c^2$), but also due to the much higher constituent mass ($m_K \approx 0.5 \text{ GeV}/c^2$). However, in the QGP, due to the high gluon densities and $T \sim m_s$, strangeness production may equilibrate with u and d quarks through gluon fusion:

$$gg \rightarrow s\bar{s} \quad .$$

This phenomenon was proposed as one of the first signatures of QGP observation in colliders [67, 68]. Indeed, an enhancement in the production of strange hadrons is observed in AA collisions, which is dependent on the event activity and increases with increasing strangeness content of the hadron [69]. Figure 2.5 displays these results.

Furthermore, the yields of hadrons measured in AA collisions can be accurately described by statistical models [70, 71] which, generally, assume that the dense system is in thermal and chemical equilibrium at the point of its freeze-out. In these models, strangeness is assumed to be conserved on average, which corresponds to a grand-canonical ensemble with a strange chemical potential μ_S .

In small systems, the conservation of strangeness must be taken into account for each interaction, locally. This necessitates the use of a canonical ensemble and introducing a parameter, V_0 , to describe the volume of this locality requirement [72]. With this approach, strangeness enhancement can be reproduced by increasing V_0 and transi-

tioning from the canonical ensemble in small systems to the grand-canonical ensemble in AA collisions, as depicted in Fig. 2.5.

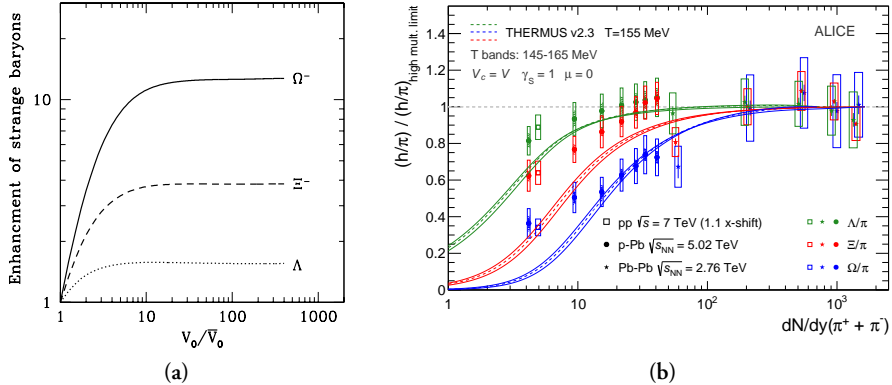


Figure 2.5: (a) Dependence of strange baryon densities on the parameter V_0 characterising the volume where strangeness is locally conserved in models describing strangeness suppression in small systems as canonical suppression. The volume is normalised to a typical AA value of $\bar{V}_0 = 7.4 \text{ fm}^3$. [72]. (b) Ratios of yields of strange baryons to pions in pp, p-Pb, and Pb-Pb collisions as a function of the pion multiplicity normalised to the high-multiplicity limit in 0 – 60% most central Pb-Pb collisions. The results are compared with a statistical model combining the canonical and grand-canonical approach. [69, 71]

2.2.3 Collective flow

The strongly interacting plasma exhibits a collective expansion which can be described by hydrodynamic equations, since the mean free paths of the constituents are much smaller than the system size ($\lambda \ll L$). The non-uniform energy density in the initial state results in varying pressure gradients, which drive this expansion. Since the centre of the plasma has greater pressure than its outside regions, common expansion velocity field develops, which results in the so-called *radial flow*. Similarly, the medium also translates the directionally-dependent anisotropies in the initial state, which stem from the almond-shape geometry of the collision overlap region as well as nucleonic fluctuations, to the final-state. This is the so-called *anisotropic flow*.

Together with hadronic re-scattering, the flows are reflected in the kinematics of the final-state hadrons. When comparing p_T spectra in central AA collisions to those in peripheral or in pp collisions, a broadening as well as a momentum boost can be observed (see Fig. 2.6), caused by the radial expansion as well as the less important thermal motion [73, 74, 75]. The expansion effect depends on the mass of the hadrons, as the amount of additional p_T acquired is proportional to their mass and the collective expansion velocity field, $p \approx m\beta c$. A notable exception to this trend is the ϕ

quarkonium; although comparable with the proton ($m_\phi \approx 1.02 \text{ GeV}/c^2 \sim m_p$), its scattering cross-section is much smaller [76].

The p_T spectra influenced by radial flow can be described by the Blast-Wave parametrisation [77]. In this approach, the radial expansion is accounted for as a common velocity field profile $\beta(r)$ affecting thermal spectra,



where β_s , R , and n are the expansion velocity on the surface of the plasma, its radius, and an extra parameter usually ranging $0.7 - 1.0$ in central collisions [73], respectively. The effects of radial flow can also be reproduced in AA collisions with hydrodynamic models using an equation of state from LQCD and hadronic re-scattering [76], and in pA collisions with the EPOS3 model, which also incorporates hydrodynamic evolution in QGP droplets [78].

Ratios of baryons to mesons, such as p/π or $(\Lambda^0 + \bar{\Lambda}^0)/(2K_s^0)$, as a function of event activity are often used to demonstrate the effect of radial flow, as shown in Fig. 2.6. In these ratios, the modification of p_T spectra results in the following effects on the high-event-activity ratios:

1. The peak in the ratio is shifted to higher p_T by up to $1.5 \text{ GeV}/c$,
2. there is an enhancement of baryons in the intermediate p_T $1.5 < p_T < 6 \text{ GeV}/c$ region,
3. and a corresponding depletion of baryons at low p_T .

Figure 2.7 shows a typical shape of the initial state with its azimuthal anisotropy and the resulting pressure gradients. Anisotropic flow can be quantified by decomposing the azimuthal particle distribution into its Fourier series [79]:

$$\frac{dN}{d\varphi} \propto 1 + 2 \sum_{n=1}^{\infty} v_n e^{in(\varphi - \Psi_n)} , \quad v_n = \langle \cos[n(\phi - \Psi_n)] \rangle , \quad (2.5)$$

where Ψ_n is the symmetry plane of the n -th harmonic and v_n is the Fourier coefficient corresponding to that harmonic, also known as the flow coefficient. In this context, a finite initial state ellipticity ϵ_2 leads to a finite *elliptic flow* v_2 , triangularity ϵ_3 to a *triangular flow* v_3 , and so on [80, 81].

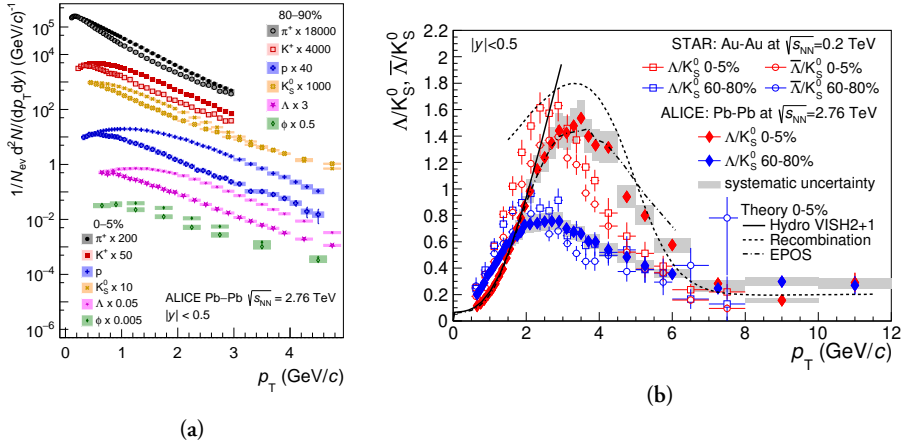


Figure 2.6: (a) Transverse momentum spectra of light-flavour hadrons in central 0–5% and peripheral 80–90% Pb-Pb collisions scaled by arbitrary factors to enhance the visibility. [62, 73, 74, 75] (b) Λ to K_S^0 ratios of transverse momentum spectra in Pb-Pb collisions at the LHC and Au-Au collisions at RHIC for central 0 – 5% events (red) and peripheral 60 – 80% events (blue). [74]

The flow coefficients can be experimentally extracted using various methods, including two-particle azimuthal correlations (as shown in Fig. 2.7), and are typically studied as a function of event multiplicity. It is important to note that these azimuthal correlations between particles due to anisotropic flow are long-range, i.e. present consistently across the entire pseudorapidity range $\Delta\eta$ (the so-called “ridge”) [82], which makes them distinguishable from similarly appearing “non-flow” short-range correlations coming from jet fragmentation and resonance decays.

Moreover, measurements of v_2 in AA collisions for different particle species reveal a mass dependence in the low- p_T region, and a baryon/meson dependence in the intermediate p_T region, with baryons having approximately 1.5 times higher values [83]. This suggests that the flow of hadrons is built up from its deconfined constituents.

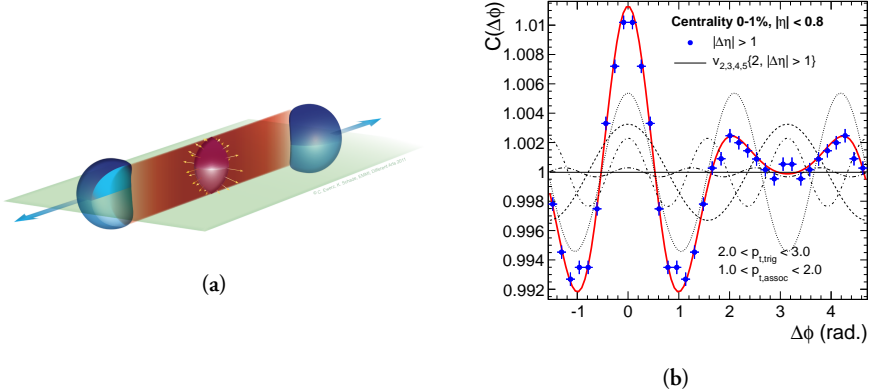


Figure 2.7: (a) Illustration of a collision of ultra-relativistic heavy nuclei and the overlapping region with pressure gradients (yellow). [84] (b) Correlation function of the relative azimuthal angle between a trigger particle and an associated particle, separated by a pseudorapidity gap, measured in central Pb-Pb collisions. The contributions from the elliptical, triangular, quadrupolar, and pentapolar harmonics are shown as different dashed lines. [81]

2.2.4 Jet quenching

In AA collisions, partons produced in hard scattering processes interact with the colour charges in the quark-gluon plasma, resulting in the loss of energy through collisions and gluon bremsstrahlung. This phenomenon is known as jet quenching and modifies or even "quenches" the parton shower [85, 86]. In the factorisation theorem in Eq. 1.13, this corresponds to the medium-modification of the fragmentation functions. Studies of parton energy loss and jet quenching often use the transport coefficient \hat{q} , which describes the average p_T loss of a parton per a mean free path in the plasma and corresponds to the medium opacity

Jet quenching is one of the most important probes into the structure and dynamical properties of the QGP, since the hard partons experience its entire evolution, similarly to the case of heavy quarkonia discussed in Sec. ???. It can also be compared with a large body of sound theoretical calculations [87] and MC simulations [88] based on QCD. Experimentally, jet quenching can manifest as suppression of the jet yield or even its complete disappearance, due to the energy loss of partons in the medium and their re-scattering. [62]

Figure 2.8 displays such an AA event with a large jet imbalance and juxtaposes it with a pp event, where the leading and the recoil jet need to be balanced in azimuth due to conservation laws. Further effects and fields of study of jet quenching include the modification of jet substructures and shapes.

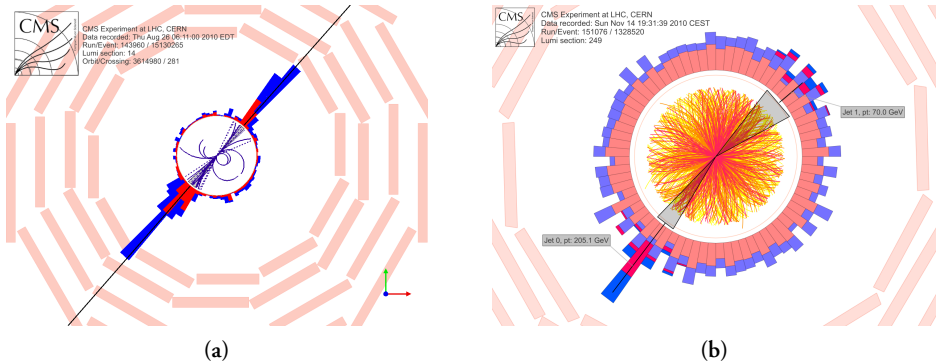


Figure 2.8: Event displays from CMS in azimuthal plane showing a collision of (a) pp and (b) Pb-Pb with a dijet. The red and blue columns correspond to energy deposits in the detector calorimeters. [57, 89]

2.2.5 Cold nuclear matter effects

It should be noted that apart from the QGP, other effects come into play due to the fact that the collision involves two nuclei instead of two protons. These effects are important caveats to bear in mind and include:

1. Nuclear (anti-)shadowing: Reflects the modification in production due to differences in nPDFs and PDFs. [90]
2. Cronin effect: Describes the initial parton energy loss due to scatterings in the nuclear medium and broadens measured p_T spectra. [91]
3. Nuclear absorption: Describes the dissociation of particles due to their interactions with the passing-by nuclear remnants [92]. It is generally negligible at LHC energies.
4. Co-mover absorption: This is the effect of inelastic interactions with the hadron gas. [93]

These effects can be isolated and quantified in pA or very peripheral AA collisions.

2.3 QGP phenomena in small systems

Measurements within the last decade have shown that certain QGP phenomena can also be observed in high-multiplicity events of pp collisions at LHC energies, which

challenges the traditional assumption that QGP is only produced in AA collisions. This has sparked debates about the existence of QGP in pp collisions and, to a lesser degree, about the absence of QGP in AA collisions, despite the extensive experimental evidence.

Furthermore, the observed behavior of these phenomena indicates that the role of event multiplicity N_{ch} may be more significant than the collision system size. This has led to ongoing efforts to establish a consistent and seamless link between the paradigms of pp and AA collisions.

Strangeness and charm enhancement

ALICE measurements on Λ/π , Ξ/π , and Ω/π ratios demonstrate that the production rates of particles containing strange quarks increase faster with multiplicity than those containing only u and d quarks [94]. This also depends on the strangeness content – the effect is the strongest for Ω and vanishes for protons. Furthermore, the evolution to larger systems seems to be continuous with respect to N_{ch} . The measurements can be seen in Fig. 2.9 [62].

To contrast the strangeness measurements with charm, the $J/\psi/\pi$ ratio also shows a clear increase in yield with increasing N_{ch} in pp collisions, as is shown in Fig. 2.9 [95, 96]. However, this comes with an important caveat: high-multiplicity events are biased to have enhanced hard processes, as discussed further in Chapter 7. Moreover, the evolution of this phenomenon is also not continuous with N_{ch} when going from pp collisions at $\sqrt{s} = 13 \text{ TeV}$ to $\sqrt{s_{\text{NN}}} = 5.02 \text{ TeV}$, which can also be explained by the fact that charm quarks are produced solely in hard scattering processes, the rates of which depend on the collision system and center-of-mass energy.

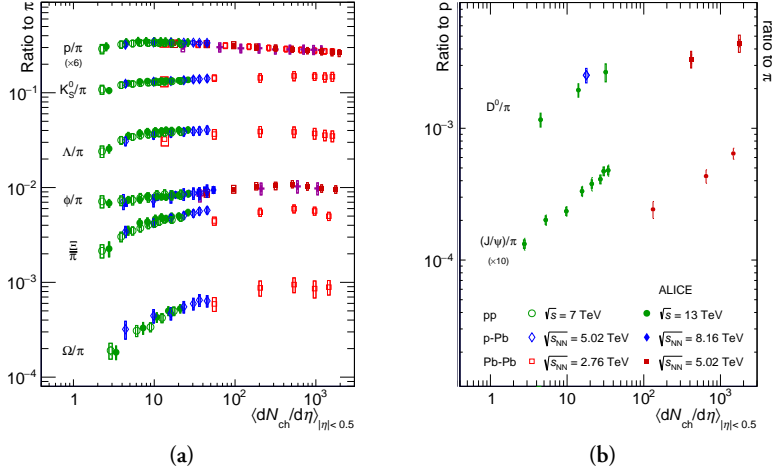


Figure 2.9: Ratios of integrated yields of (a) various light-flavour hadrons [94] and (b) charm mesons [95, 96] to pions as a function of multiplicity in pp, p-Pb, and Pb-Pb collisions. [62]

Anisotropic flow

Azimuthal correlations and anisotropic flow measurements in small collision systems exhibit features similar to those observed in AA collisions, hinting at the presence of collective expansion [97]. However, in small systems, these measurements are particularly challenging due to their large sensitivity to non-flow effects, such as jet fragmentation or resonance decays, which can mimic the features of collective flow.

While models using hydrodynamic-like descriptions seem to be able to describe v_2 results (despite the fact that their assumption $\lambda \ll L$ is not valid) [98], especially at high multiplicities, the interpretation of the results in small systems is still under investigation. The values of elliptic flow v_2 seem to be comparable to those in low-multiplicity Pb-Pb collisions, although the evolution of v_2 across different system sizes does not appear to be smooth. The measurements from CMS displaying a clear ridge in high-multiplicity events [97] and the v_2 results from ALICE [99] can be seen in Fig. 2.10.

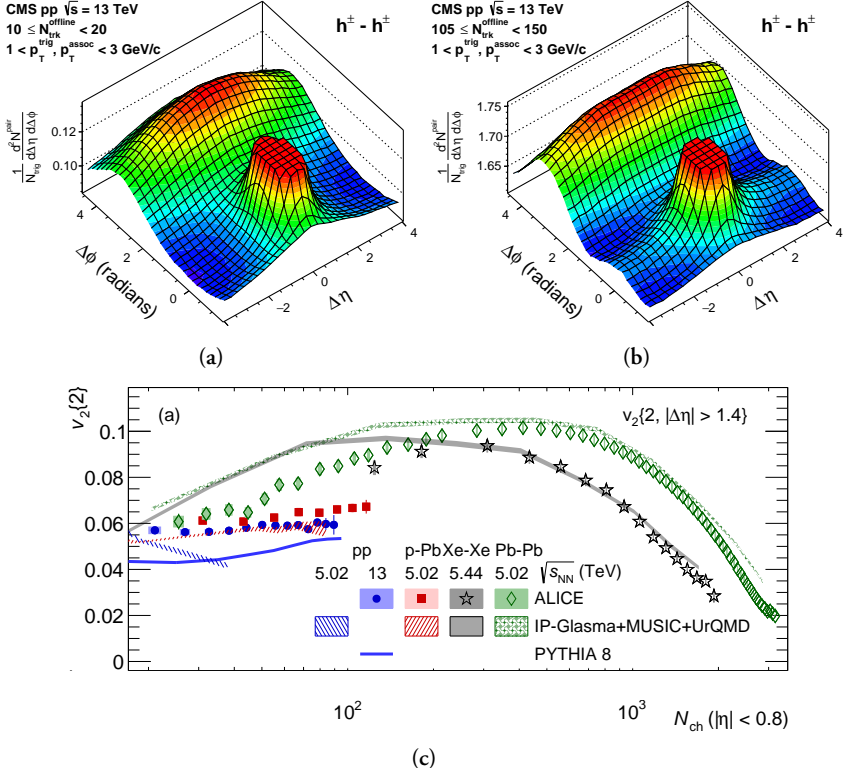


Figure 2.10: (a, b) Two-dimensional two-particle correlation functions of charged hadrons in low (left) and high (right) multiplicity events of pp collisions at $\sqrt{s} = 13 \text{ TeV}$. [97] (c) Elliptic flow measured using two-particle cumulants with a pseudorapidity separation in pp, p-Pb, Xe-Xe, and Pb-Pb collisions as a function of multiplicity. [99]

Radial flow

Measurements of the ratio of Λ to K_S^0 p_T spectra ratio were also studied in pp collisions with differing N_{ch} , see Fig. 2.11 [100]. The boost of a collectively expanding system, as expected in the context of radial flow, should have a greater impact on heavier hadrons, leading to an enhancement of the baryon-to-meson ratio at intermediate p_T . This enhancement is observed in the Λ/K_S^0 ratio, its magnitude increases with increasing N_{ch} and the peak position shifts towards higher values collisions, consistent with the hydrodynamic picture. The increase at intermediate momenta leads to a corresponding depletion at low p_T . High- p_T (as well as integrated) Λ/K_S^0 ratios exhibit essentially no (or minor) multiplicity dependence. This observation also applies to proton-to-pion ratios.

Recent studies have also investigated the charmed baryon-to-meson ratio Λ_c/D^0 , with

similar findings, although measurements with smaller uncertainties are still required. Fig. 2.11 presents the corresponding results.

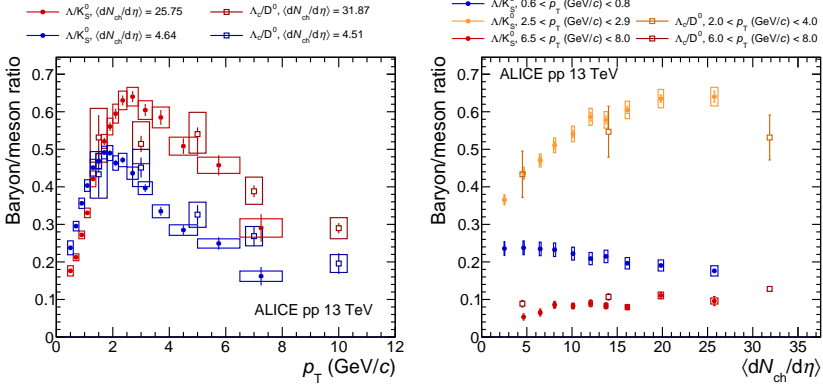


Figure 2.11: Baryon-to-meson ratios shown as the p_T differentials (left) and integrated yields in various p_T ranges as a function of multiplicity (right) for the Λ/K_S^0 and Λ_c/D^0 in pp collisions at $\sqrt{s} = 13$ TeV. [62, 96, 100]

Sequential suppression of Υ states

While defining R_{AA} to compare high-multiplicity and low-multiplicity events is unclear, and measuring yields as a function of N_{ch} is complicated by its biases related to the hardness of primary scatterings, it is worthwhile to investigate the ratio of excited-to-ground states of quarkonia as a function of N_{ch} .

Interestingly, these results [101] exhibit a decrease with increasing N_{ch} , resembling the pattern of sequential suppression due to QGP deconfinement. Even more remarkable, this dependence disappears in low-sphericity, jet-dominated, events (event shape observables such as sphericity are discussed in more detail in Chapter 6). These findings, reported in Fig. 2.12, suggest that the dependence on N_{ch} is solely influenced by the UE, rather than jets. As event multiplicity grows larger, excited Υ states become relatively less likely to be measured compared to the ground state.

These results indicate the need for a better understanding of Υ hadronization and the role UE may play in it. They also raise the question of whether the ground state is enhanced rather than the excited states being suppressed. Additionally, the effects of the mass differences must also be considered. However, the fact that low-sphericity, jet-dominated events have the same ratios as high-sphericity, UE-dominated events at low N_{ch} argues against these ideas.

An important caveat to note is that hadronic decays (which are dominant) of the

heavy Υ states may result in tens of produced particles [102]. Therefore, even minor discrimination against the excited states could hypothetically be correlated with a substantial but trivial increase in the accompanying N_{ch} . To the author's knowledge, there are currently no available phenomenological descriptions of the observed behavior, which further limits potentially groundbreaking interpretations.

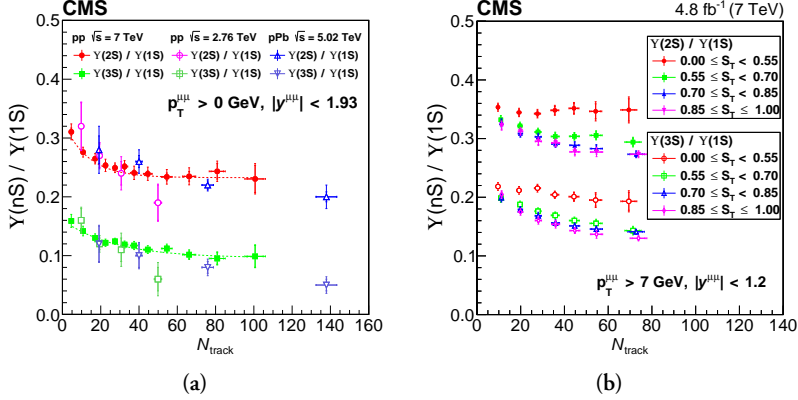


Figure 2.12: The $\Upsilon(2S)/\Upsilon(1S)$ and $\Upsilon(3S)/\Upsilon(1S)$ ratios of measured yields in pp collisions as a function of (a) multiplicity, compared with p-Pb results, and (b) multiplicity and transverse sphericity, with the di-muon transverse momentum $p_T^{\mu\mu} > 7 \text{ GeV}/c$. [101]

Other QGP signatures

If a QGP is formed in small systems with sufficient volumes, the effect of jet quenching should be observed. One can also expect to observe it, due to the fact that in small systems, high- p_T hadrons have been measured to have finite flow v_2 [103], which could indicate that hard partons interact with an expanding medium. Whilst theoretical approaches do not provide unambiguous answers on whether this phenomenon can be observed [104] or not [105], experimental results on jet quenching in both pp and p-Pb collisions are consistent with no observable effect, within uncertainties [106]. These results are mostly based on measuring jet yields as a function of event activity, although such measurements are challenging due to fluctuations and interplays between jet characteristics and event activity.

2.3.1 Role of multiplicity

The observations made above highlight the significance of studying the role of multiplicity N_{ch} . In contrast to AA collisions, high-multiplicity events in pp collisions do not arise from a mere increase in the amount of colliding matter, as the values of

N_{part} and N_{coll} are fixed:

$$N_{\text{part}} = 2, \quad N_{\text{coll}} = 1. \quad (2.6)$$

Additionally, due to the relatively constant initial system volume, high- N_{ch} pp events may exhibit energy densities that exceed the threshold for QGP formation, given that the highest N_{ch} values are similar to those observed in peripheral AA collisions, where QGP formation is observed.

Clearly, the picture is more complex and despite its simplicity as an event activity classifier, N_{ch} poses challenges when it comes to relating data to theory since it cannot be directly linked to the initial state, and multiplicities in different events may originate from entirely different processes.

To address these issues and gain a better understanding of the evolution between low and high multiplicities and the potential for QGP formation, this dissertation focuses on transverse spherocity $S_O^{(p_T=1.0)}$ and underlying event activity R_T measurements. The goal of these studies is to provide a deeper insight into the relevant degrees of freedom involved.

2.4 Phenomenological models

The next parts of this thesis give an overview to phenomenological models and event generators pertinent to the measurements in Chapters 6 and 7. Other generators, such as Herwig 7 [107] or Sherpa [108], are not discussed here.

2.4.1 Pythia

Pythia is a Monte Carlo event generator used to simulate full events of high-energy particle collisions, based mostly on approximately perturbative QCD, with some important non-perturbative aspects. With more than four decades of development, only a brief overview is given in this thesis, whilst detailed description can be found in Ref. [29, 109]. It has a modular structure to simulate different aspects of the collision process and includes the simulation of the initial kinematics, hard scattering, multiple parton interactions, parton showering, and hadronization, which were all discussed in Chapter ???. The various components of the event simulation, such as the matrix element for the primary scattering, or even the parton evolution, can also be replaced with external alternatives.

Its current and in ALICE most widely used version is Pythia 8, specifically its Monash tune [110], incorporating colour reconnections. Pythia has also included the implementation of Angantyr [111], a new model for the simulation of collisions of nuclei.

A pp collision event, as simulated by Pythia, can be seen in the illustration in Fig. 2.13 and crudely structured as:

1. Relevant parton kinematics are determined based on the PDFs of the beam particles and nature of the event is decided (e.g. Z^0 production). Produced resonances decay.
2. All subsequent partonic activity is simulated. This includes the initial- and final-state parton radiation, MPIs, and handling of the beam particle remnants. Eventually, after the full parton shower evolutions, a full partonic structure and string configuration is given.
3. Hadronisation occurs by the Lund string model fragmentation. This part is completely non-perturbative and fully phenomenological. Unstable particles decay and a full final-state particle collection is obtained. [112]

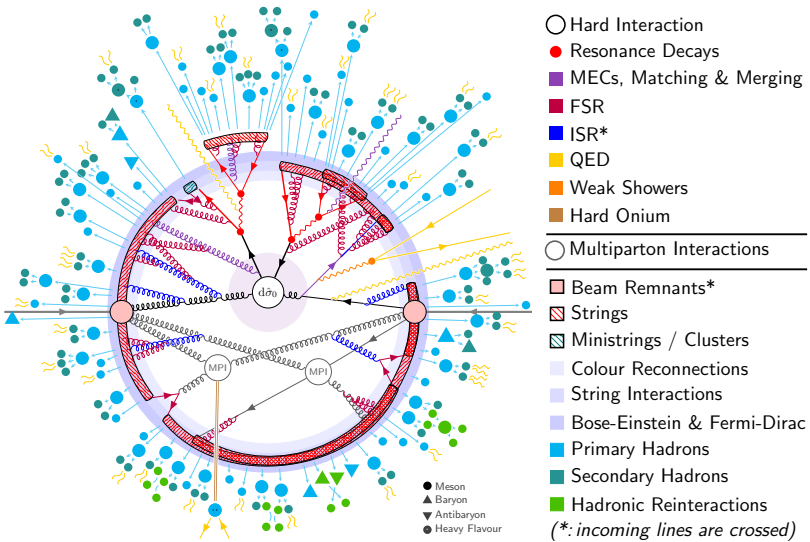


Figure 2.13: Diagram depicting a full simulation of pp collision event with its various components. For full description, see Ref. [29].

2.4.2 String interactions and Ropes

While some effects typically associated with QGP formation, such as radial flow, can be somewhat mimicked in Pythia by colour reconnection [31, 113], as touched upon in Sec. ??, it is not sufficient to describe the strangeness enhancement patterns observed in small systems.

Ideas that overlapping QCD strings in high-density environments interact and form higher-tension ropes date back to modelling AA collisions in 1984 [114] and have been explored further [115], specifically in the framework of the DIPSY model [116]. This “rope hadronisation” approach is also incorporated similarly in Pythia 8 and can be included in its simulations, which in the context of this dissertation will be referred to as the Pythia 8 Ropes tune.

In Pythia, strings are considered overlapping on purely geometrical considerations and utilise a parameter α to quantify the size of strings relatively to the proton radius. Combining two strings follows an algebra based on the SU(3) group, described below, following a more detailed discussion in Ref. [116].

A $q\bar{q}$ string can be viewed as a SU(3) triplet **3**. Stacking another string suggests adding another triplet and forming a multiplet with quantum numbers p , corresponding to the number of coherent triplets **3** (e.g. all red), and q , corresponding to the number of coherent antitriplets **3̄** (e.g. all anti-blue). Using a $\{p, q\}$ notation, the algebra for multiplets is as follows:

$$\{1, 0\} \otimes \{1, 0\} = \{2, 0\} \oplus \{0, 1\} , \quad (2.7)$$

$$\{1, 0\} \otimes \{0, 1\} = \{1, 1\} \oplus \{0, 0\} . \quad (2.8)$$

The first equation, physically, corresponds to merging of two colour strings with colour flows going in the same direction (same $q\bar{q}$ orientation), merging into a rope. When the colours are the same (e.g. both red), the result is a sextet rope **6**, $\{2, 0\}$. In other cases (e.g. red and blue), the result is an anti-triplet rope **3̄**, $\{0, 1\}$ (corresponding to anti-green—green string). This algebra is illustrated in Fig. 2.14.

The second equation describes stacking a triplet **3** with an anti-triplet **3̄** (opposite colour flows and $q\bar{q}$ orientation). This results either in a gluon octet **8**, $\{1, 1\}$, or a singlet **1**, $\{0, 0\}$, with destructive interference and no colour flow.

The tension of the produced rope $\tilde{\kappa}$ is proportional to the quadratic Casimir operator C_2 . When normalising to the tension of a single string κ , e.g. a $\{1, 0\}$ triplet, the

relative increase is given by

$$\frac{\tilde{\kappa}}{\kappa} = \frac{C_2(\{p, q\})}{C_2(\{1, 0\})} = \frac{p^2 + q^2 + pq + 3p + 3q}{4} , \quad (2.9)$$

so in the example of adding two red triplets, the resulting $\{2, 0\}$ rope tension is $\tilde{\kappa} = 5/2$.

During hadronisation, the rope is assumed to break not entirely at once, but rather one string at a time. For the purpose of considering the probability of creating new quarks in (1.15), the effective tension from the $\{p, q\} \rightarrow \{p - 1, q\}$ transition is given by (2.9) and corresponds to

$$\tilde{\kappa}_{\text{eff}} = \frac{2p + q + 2}{4} \kappa . \quad (2.10)$$

This means that in the example of the $\{2, 0\}$ rope breaking, the first quark creation comes with relative effective tension $\tilde{\kappa}_{\text{eff}} = 3\kappa/2$, and the second one with the normal value of $\tilde{\kappa}_{\text{eff}} = \kappa$.

The strangeness production suppression factor in (1.16) then becomes modified as

$$\tilde{\rho} = \rho^{\frac{\kappa}{\tilde{\kappa}_{\text{eff}}}} , \quad (2.11)$$

which makes it evident that overlapping many strings ($\tilde{\kappa}_{\text{eff}} \rightarrow \infty$) results in $\tilde{\rho} \rightarrow 1$ and strange quarks are produced at the same rate as up and down.

Furthermore, ideas for further interactions between strings, such as “string shoving”, wherein overlapping strings may repel each other due to transverse pressure from their excess energy, have also been developed. Such mechanisms produce effects similar to a hydrodynamically expanding medium, e.g. long-range anisotropic flow. [117]

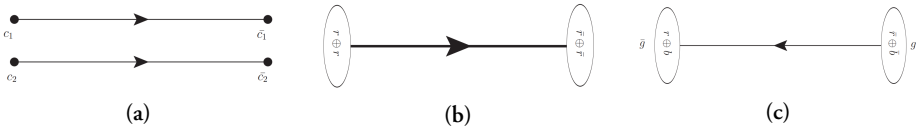


Figure 2.14: (a) Illustration of stacking two colour flow strings, triplets with colours c_1 and c_2 . (b) Rope sextet resulting from adding two coherent triplets, $c_1 = c_2, \{2, 0\}$. (c) Resulting rope anti-triplet coming from adding two incoherent triplets, $c_1 \neq c_2, \{0, 1\}$. Illustrations are by C. Bierlich.

2.4.3 EPOS LHC

EPOS is an event generator built on the Gribov-Regge theory [118], wherein several partons undergo multiple scatterings, each consisting of the hard scattering component as well as initial and final state linear parton emission. Together, they form

a so-called parton ladder and correspond to a “cut” pomeron exchange [119]. The parton ladder represents a (mostly) longitudinally flowing colour field, a “flux tube”, which may hadronise via pair production.

To model the full collision process, EPOS combines a two-component core-corona approach. When the density of flux tubes in a given volume exceeds a parameter ρ_0 , the core is formed. Conversely, flux tubes escaping the volume (usually with higher p_T) make up the corona. The core is assumed to evolve hydrodynamically, corresponding to a QGP droplet, and then hadronises collectively, where smaller core segments form hadrons following a statistical ensemble. Since the relative amount of core- and corona-related particle production can vary continuously, EPOS models can be used to describe pp, pA, and AA collisions using a single paradigm. [120]

EPOS models have been successful particularly at modelling soft-QCD physics and, apart from collider physics, are also widely used in studies of cosmic rays [121]. Throughout this dissertation, an adaptation of EPOS called EPOS LHC [120] is mostly used and shown, which only parametrises the flow dynamics of the core instead of implementing a full hydrodynamic simulation. Diagrams illustrating the partonic structure and core-corona mixing can be seen in Fig. 2.15.

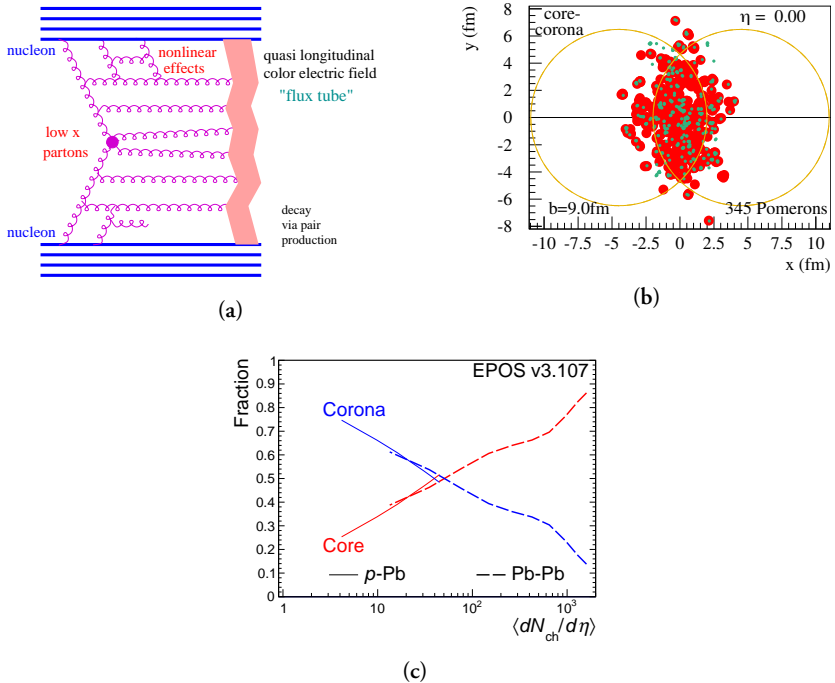


Figure 2.15: (a) Illustration of the partonic structure in the form of a parton ladder. [120] (b) Visualisation of the core (red) and corona (green) components in a peripheral 20 – 40% collision of Pb-Pb with 345 initial multiple scatterings, modelled by EPOS3 [122] (c) Fractions of particle production associated with the core (red) and corona (blue) regions in p-Pb and Pb-Pb collisions, modelled by EPOS3. [123]

Part II

Experimental Setup and Methodology

Chapter 3

ALICE's adventures at the LHC

The experimental measurements conducted as part of this dissertation in Chapters 6 and 7 have been carried out on data from proton-proton collisions at the Large Hadron Collider at CERN, collected with the ALICE detector. The aim of this chapter is to introduce these facilities.

3.1 CERN and the LHC

Conseil européen pour la recherche nucléaire (CERN) is a scientific institution dedicated to study particle physics, nuclear physics, and related fields. It was established in 1954 as a European collaborative endeavour and currently has 23 member states. The CERN laboratories employ almost 3000 on-site staff and host approx. 13000 users from universities and research institutions across the world. The biggest achievements of CERN include discoveries of the W^\pm , Z^0 , [124] and the Higgs bosons [4, 5], the first creation of anti-atoms, advancements to proton therapy and medical imaging technologies such as PET, and finally, being a birthplace to the World Wide Web.

The Large Hadron Collider (LHC) is the main particle accelerator at CERN. This synchrotron with circumference of almost 27 km can accelerate protons to energies up to 7 TeV, making it world's most powerful particle accelerators. Apart from collisions of protons measured at $\sqrt{s} = 13$ TeV, it also studies collisions of nuclei, such as lead (Pb-Pb) at $\sqrt{s_{NN}} = 5.02$ TeV, or proton-lead p-Pb at $\sqrt{s_{NN}} = 8.16$ TeV. Particles in the synchrotron are accelerated by electric fields within RF cavities and kept on their semi-circular trajectory using magnetic dipoles. Higher-polar magnets are used for beam focusing and adjustment. The particles circulate in larger bunches (of $\sim 10^{11}$ protons or $\sim 7 \times 10^7$ Pb nuclei) in two separate rings, which intersect at

sites of large experiments, detecting their collisions. Apart from ALICE, discussed in the next sections, these are:

- **ATLAS** (*A Toroidal LHC ApparatuS*) [125]: the LHC’s largest experiment and a general purpose detector, with its foci including Higgs physics, scrutiny of the SM, and BSM searches.
- **CMS** (*Compact Muon Solenoid*) [126]: also a general purpose detector, with similar physics goals, but with a different technical design than ATLAS. It has also been a prominent contributor to QGP physics, particularly the study of small systems.
- **LHCb** (*Large Hadron Collider beauty*) [127]: a detector focused mostly on precise measurements of b physics and CP violation.

Table 3.1: Selection of parameters of the Large Hadron Colliders. [128]

Parameter	Value
Circumference	26.7 km
Energy at injection	450 GeV
Magnetic field at 7 TeV	~ 8.3 T
Number of magnets	~ 9300
Revolution frequency	~ 11 kHz
Number of bunches in a beam	2808
Bunch spacing	25 ns
Design luminosity	$\sim 10^{34} \text{ cm}^{-2}\text{s}^{-1}$
Max. bunch crossing (BC) rate	~ 40 MHz
Number of inel. interactions per BC	10 – 20
Beam lifetime	~ 10 h

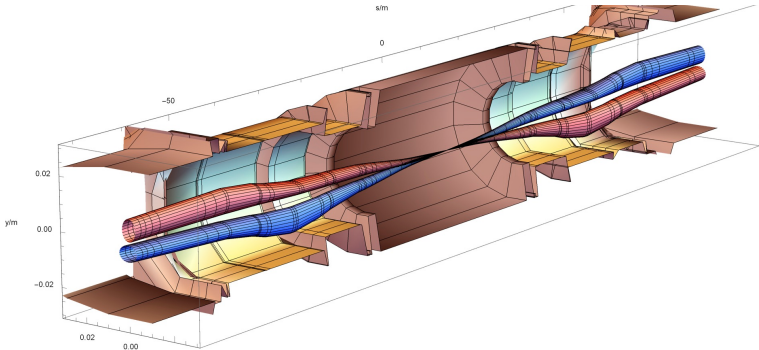
Some of the LHC parameters are summarised in Tab. 3.1 and an aerial photo of the LHC with locations of the IPs can be seen in Fig. 3.1.

3.2 The ALICE experiment

The ALICE (A Large Ion Collider Experiment) [131?] is the detector at the LHC dedicated to studying collisions of heavy nuclei and the properties of QCD matter, such as quark-gluon plasma. Its biggest strengths are precise tracking and momentum determination all the way down to $p_T > 0.15 \text{ GeV}/c$ as well as superior particle identification (PID). Its sub-detectors are subjected to a magnetic field of 0.5 T to



(a)



(b)

Figure 3.1: (a) Aerial photo of the LHC area, also depicting the location of the LHC tunnel (approx. 100 m underground), spanning over Switzerland and France. Geneva, Lac Léman, and the Mont Blanc can be seen in the background. [129] (b) Visualisation of the beam crossing at the ALICE experiment. Bunches of Beam 1 move from left to right in the blue beam envelope and bunches of Beam 2 move from right to left in the red beam envelope. The envelopes indicate the beam orbits and transverse size. [130]

allow momentum measurements from the track curvatures (in natural units, $p_T \approx 0.3Br$, $p_T \in [\text{GeV}/c]$, $B \in [\text{T}]$, $r \in [\text{m}]$).

The ALICE detector, shown in Fig. 3.2, consists of several sub-systems, each fulfilling their function. Some of them which pertain to the measurements carried out within this dissertation are listed in Tab. 3.3. The following descriptions are based on their status when the data was collected, which corresponds to Run 2.

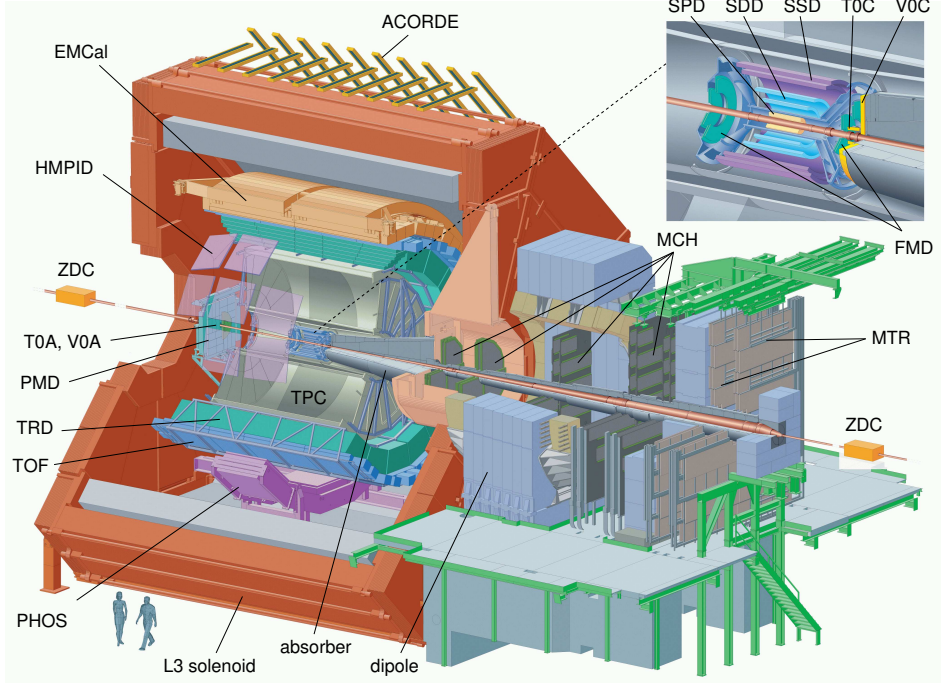


Figure 3.2: The ALICE experiment at the LHC, showing its sub-systems. The central barrel is subjected to a magnetic field from the solenoid (red). The ZDC detectors are approximately ± 113 m distant from the IP. [132]

Table 3.2: Selection of ALICE sub-detectors relevant to this thesis. Acceptance is given in terms of pseudorapidity, the azimuthal coverage for the detectors presented is full. The z -axis is defined anticlockwise to the LHC. [132]

Detector	Acceptance	Position (cm)	Technology	Main purpose
ITS SPD	$ \eta < 2.0$	$r = 3.9$ cm	Si pixel	tracking, PV, triggering
ITS SPD	$ \eta < 1.4$	$r = 7.6$ cm	Si pixel	tracking, PV, triggering
ITS SDD	$ \eta < 0.9$	$r = 15.0$ cm	Si drift	tracking, PID
ITS SDD	$ \eta < 0.9$	$r = 23.9$ cm	Si drift	tracking, PID
ITS SSD	$ \eta < 1.0$	$r = 38.0$ cm	Si strip	tracking, PID
ITS SSD	$ \eta < 1.0$	$r = 43.0$ cm	Si strip	tracking, PID
TPC	$ \eta < 0.9$	$r = 85.0$ cm	Ne drift, MWPC	tracking, PV, PID
V0A	$2.8 < \eta < 5.1$	$z = 329.0$ cm	scintillator	centrality, triggering
V0C	$-3.7 < \eta < -1.7$	$z = -88.0$ cm	scintillator	centrality, triggering

3.3 Time Projection Chamber

The Time Projection Chamber (TPC) [133] is ALICE’s primary tracking detector and investigation tool for hadronic observables. It is located in the central barrel. The cylinder, illustrated in Fig. 3.3 is filled with a mixture of gases and a central 100-kV high-voltage electrode subjects it to a longitudinal electric field. Charged particles traversing the gas medium ionise it and the electrons then drift to the end-caps with a drift time of approx. $90\ \mu\text{s}$. There, they are detected in Read-out Chambers (ROCs), using Multi-Wire Proportional Chambers (MWPC), and together with the drift duration time, a three-dimensional information can be determined. The ROCs are radially divided (IROCs and OROCs) and segmented into 18 sectors in azimuth. Each ROC has 159 rows and its signals are processed by attached Front-End Cards (FECs). The MWPC principle and the ROC design, visualised with a charged particle track crossing all its rows, can be seen in Fig. 3.4.

In addition to the tracking information, the TPC is also used in PID, by measuring the charged particles’ specific ionisation loss dE/dx . Measurements of dE/dx for different particle species as a function of the particle momentum and charge is displayed in Fig. 3.3. A selection of TPC parameters not discussed above is given in Tab. ??.

Table 3.3: Selection of parameters of the Time Projection Chamber. [131]

Parameter	Value
Radial position (active volume)	$84.8 < r < 246.6\ \text{cm}$
Length (active volume)	$2 \times 250\ \text{cm}$
Detector gas	Ne/CO ₂ /N ₂ or Ar/CO ₂
Spatial resolution	$0.8 - 1.1\ \text{mm}\ \text{in}\ r\phi$ $1.1 - 1.2\ \text{mm}\ \text{in}\ z$
dE/dx resolution	$\sim 5.0\%$
Material budget X/X_0	3.5% near $\eta = 0$

3.3.1 Upgrade for Run 3: GEM read-outs

In the Run 2 setup, to avoid build-up of space charge in the TPC due to backflow of ions from the amplification region in MWPCs, a gating grid is used. This limits the operating rate of the TPC to approx. 3.5 kHz. However, for the Run 3 operation, the TPC has been planned to enable a continuous read-out mode of Pb-Pb collisions at the interaction rate 50 kHz. For this reason, a new read-out technology, the Gas Electron Multiplier (GEM), is used. The technology and upgraded are discussed in more

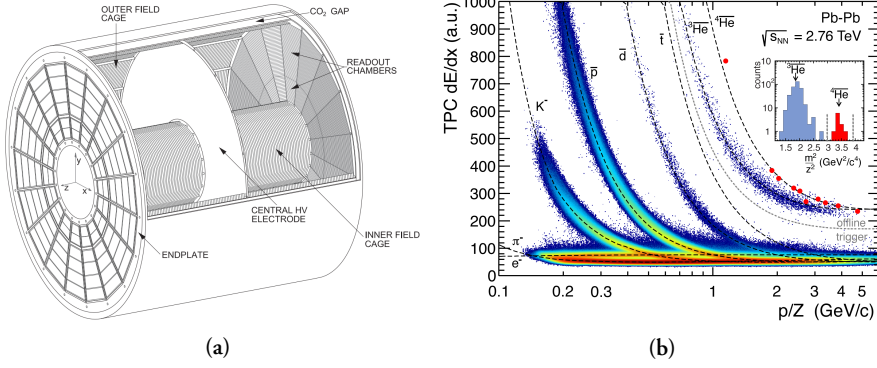


Figure 3.3: (a) Illustration of the TPC detector. [133]. (b) Ionisation energy loss of charged particles as a function of their momentum normalised by their charge as determined by the TPC. The dashed lines represent predictions from calculations. [132]

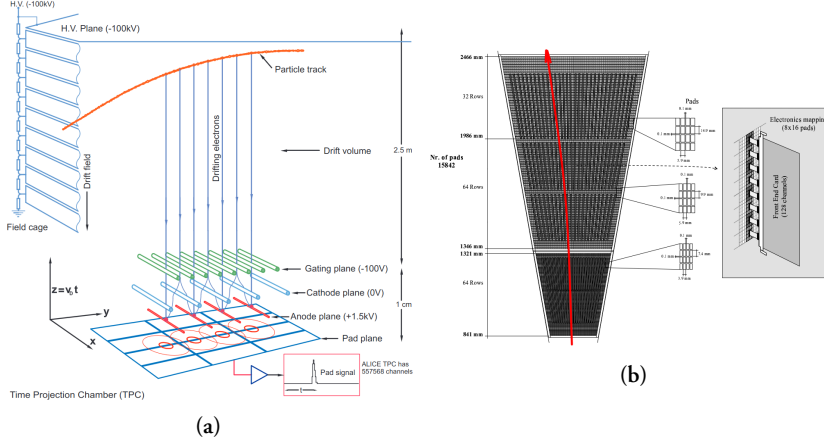


Figure 3.4: (a) Depiction of the operating principle at the ROCs, using MWPC. [134] (b) The IROC (bottom part) and OROC (top part) visualised with their number of rows and the signal-processing FECs. Also shown is a charged particle trajectory (red), which in this case crosses all 159 rows. [133] (modified)

detail in Ref. [135]. Commissioning of this upgraded TPC comprised the author's qualification task.

The GEM uses $50\text{-}\mu\text{m}$ thin foils of insulating material, coated with conductive layers of thickness $2 - 5 \mu\text{m}$ at each side, to which a potential difference of $200 - 400 \text{ V}$ is applied. The foil is perforated with double-conical holes of diameters ~ 70 and $\sim 50 \mu\text{m}$ and a pitch of ~ 140 or $\sim 280 \mu\text{m}$. The electric field in the holes then causes avalanche multiplication. Four GEM layers are stacked on top of each other in a way, where the holes have different positions and densities, which reduces the ion backflow. Typically, for one electron, the gain is around 2000, with 20 ions flowing

back into the drifting region. The GEM setup at ALICE is displayed in Fig. 3.5.

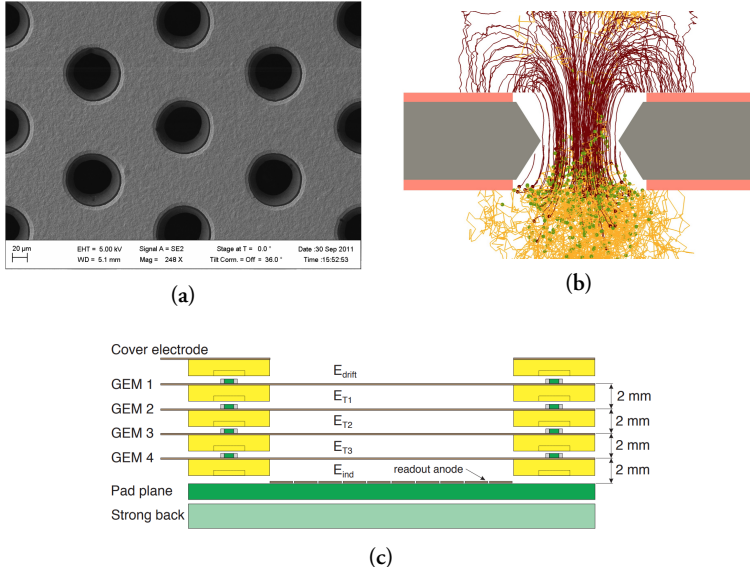


Figure 3.5: (a) Electron microscope photograph of a GEM foil with hole pitch $140\ \mu\text{m}$. [134] (b) Simulation of the charges in GEM holes. Dark lines represent ions and light lines electrons. Green dots mark multiplication site. (c) Schematic of the GEM setup at the upgraded ALICE TPC. [133]

3.4 Inner Tracking Systems

The Inner Tracking System [131, 136] is a set of semiconductor-based detectors also located in the central barrel, but much closer to the beam pipe. ALICE uses the ITS for its great spatial resolution, which complements the TPC tracking and allows for precise determination of the primary vertex (PV) as well as secondary vertices of short-lived particle decays. Moreover, thanks to its fast processing, it is also used for triggering. The ITS consists of three detectors, each of two layers, which use different silicon detector technologies:

- Silicon Pixel Detector (SPD): uses an extremely granular pixel matrix closest to the IP, where particle densities are the highest.
- Silicon Drift Detector (SDD): uses a similar technology based on drift cells. It is slightly less granular than the SPD but allows measuring of the deposited charge and thus PID based on dE/dx .

- Silicon Strip Detector (SSD): uses a silicon detector with two arrays of strips, misaligned with $\Delta\phi \approx 2$ deg, forming a lattice, on which a spatial coordinate can be determined. Similarly to the SDD, dE/dx can also be measured.

Important parameters of the ITS sub-system can be found in Tab. 3.4 and the operating principles of the different silicon-based detector technologies used is discussed e.g. in Ref. [137, 138].

Table 3.4: Selection of parameters of the Inner Tracking System. [131]

Detector	SPD	SDD	SSD
Parameter			
Area (m^2)	0.07 and 0.14	0.42 and 0.89	2.09 and 2.68
Cell size (μm)	50×425	150×300	95×40000
Number of cells (M)	9.84	23	2.6
Spatial resolution (μm)	12 in $r\phi$, 100 in z	38 in $r\phi$, 28 in z	20 in $r\phi$, 830 in z
Mat. budget, layers X/X_0	1.14% and 1.14%	1.13% and 1.26%	0.83% and 0.86%
Mat. budget, supp. X/X_0	0.52%	0.25%	0.53%

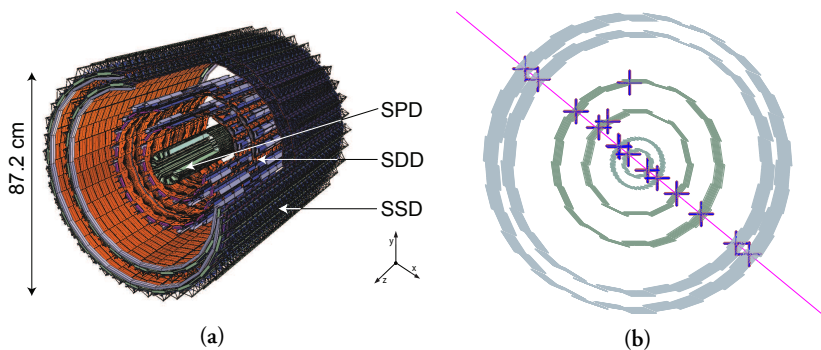


Figure 3.6: (a) Three-dimensional model of the ITS sub-system in ALICE detector simulations. (b) Display of a cosmic event detected by the ITS. [136]

3.5 V0A and V0C

The V0A and V0C¹ are two arrays of plastic scintillator counters, with PMT read-outs, together forming the V0 sub-system [139]. They are placed asymmetrically on the z -axis with respect to the IP in order to accomodate the hadron absorber used in

¹In ALICE, the “A-side” points in the counter-clockwise and the “C-side” in the clockwise direction of the LHC beam pipe, aligned with the z -axis. The C-side contains the muon system.

the muon tracking system of ALICE. Their inner and outer radii are 4.3 and 42.2 cm for the V0A and 4.5 and 32 cm for the V0C. Furthermore, they are segmented into 8 sectors azimuthally and 4 sectors radially. This is usually not granular enough for tracking, but sufficient for forward multiplicity estimation (combining amplitudes of both parts, referred to as V0M) or determination of the event plane.

Thanks to its speed, the V0 is also used for triggering. Additionally, since they can be used in coincidence, interactions of the protons/nuclei with residual gas in the beam pipe outside of the IP can be identified based on the different time information and rejected. The two detectors are visualised in Fig. 3.7.

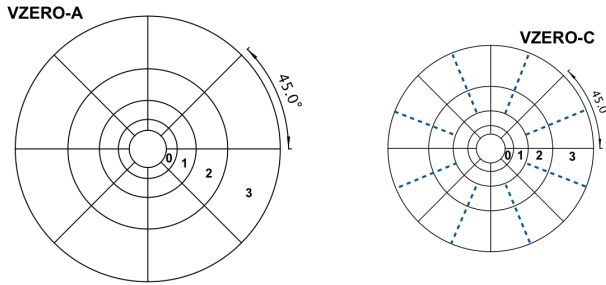


Figure 3.7: Schematic of the V0A and V0C scintillator arrays. [139]

Chapter 4

Events, Tracks, and Vertices

This Chapter provides an overview of the triggering and data preparation procedures at the ALICE experiment. The aim is to give the reader an understanding of the process of obtaining final objects representing the particles produced in hadronic inelastic collisions at the interaction point of the LHC, utilizing the experimental apparatus that was described in the previous chapter.

4.1 Events and triggers

The ALICE experiment uses a trigger system [132, 140] to accommodate the different detector read-out times, limited data storage, and to select interesting physics events from collisions with rates of roughly 8 kHz for Pb-Pb collisions and up to 300 kHz for pp collisions. The Central Trigger Processor (CTP) collects input data from the trigger detectors and makes a decision about whether to take or reject the event, with the trigger decision split into three levels: L₀, L₁, and L₂.

The L₀ trigger level makes its decision based on the fastest detectors (e.g. the SPD and V0) and sends the decision back to detectors in $\sim 1.2 \mu\text{s}$. The L₁ trigger decision is based on all remaining fast detector inputs (also including e.g. the Zero Degree Calorimeters located 113 m far from the IP) and arrives back into detectors in $6.5 \mu\text{s}$. The final L₂ trigger level waits for all the detector readouts, including the slowest TPC detector, happening in about $105 \mu\text{s}$ time. Several trigger classes can be collected simultaneously during the data taking. Once an event passes the trigger decisions of the CTP, it is sent to the Data Acquisition System (DAQ) for more detailed processing and compression of the final data.

In ALICE measurements, the following names are commonly used for some of the triggered events:

- kINT7 : the usual minimum bias (MB) class in pp collisions, based on a coincidence of the V0A and V0C detectors,
- kINT1 : also a MB class, requiring at least two signals among V0A, V0C, and the SPD,
- $|INEL>0|$: requires a MB class and at least one SPD “tracklet” within $|\eta| < 1$, which is reconstructed in the two SPD layers.

4.2 Event and track reconstruction

Reconstruction of the event information in the central barrel follows a procedure discussed in Ref. [] and summarised in Fig. 4.1. It begins with clusterisation, where the detector data is transformed into clusters, or *reconstruction points*, that include the spatial information, signal amplitude, signal time, and associated errors. The clusterisation is carried out locally for each detector, for instance, for the TPC, a cluster corresponds to a crossed row in the ROCs. The next steps are discussed in this section.

– Next, preliminary primary vertex (PV) is determined by utilising clusters in the first two ITS layers (SPD). The Kalman filter technique is employed to perform track finding and fitting in TPC and ITS. The discovered tracks are then matched to other detectors in the central barrel and fitted. The reconstructed tracks are used to determine the final interaction vertex. The central-barrel tracking procedure concludes with a search for photon conversions, strange hadron decays ($K^0 S/\bar{K}$, Ξ^\pm , and Ω^\pm), and Vo particles. The steps are discussed in greater detail in this section.

4.2.1 First primary vertex determination

A preliminary primary vertex (PV) is determined using tracklets formed in the two SPD layers of the ITS. A three-dimensional reconstruction is performed in pp and pA collisions, iteratively, so that events with in-bunch pile-up can be treated. With each iteration, clusters with tracklets already pointing to a vertex are removed. By construction, the first found vertex has the highest number of corresponding tracklets and is defined as primary. If this method fails, the PV is determined only in the z -dimension. This is also the default in AA collisions. These methods are visualised in Fig. 4.2.

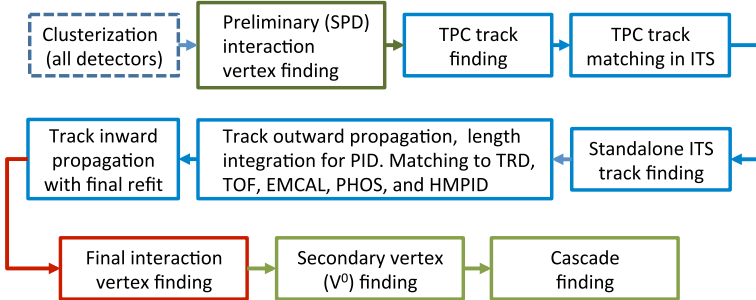


Figure 4.1: Work flow diagram of the event information reconstruction in the central barrel. [130]

4.2.2 Tracking

Track finding (recognition) and track fitting (reconstruction) is carried out simultaneously using the Kalman filter technique in three steps: inwards, outwards, inwards [142]. The entire process is illustrated in Fig. 4.3.

First, for *primary* tracks, i.e. tracks hypothesised to originate from the PV, seeds are found from the preliminary SPD PV and pairs of TPC clusters at the highest radii, where track densities are the lowest. For *secondary* tracks, coming for instance from weak decays with displaced secondary vertices, three TPC clusters are used instead of considering the PV. The track seeds are then projected inwards, adding clusters fulfilling given proximity cuts, and updating the track parameters at each step, until the inner TPC radius is reached. Preliminary dE/dx is also stored. Moreover, tracks sharing multiple clusters (approx. more than 25%) are discarded in favour of their higher-quality doubles.

The TPC tracks are then extrapolated to the ITS, where they continue to get updated. This tracking efficiency in the TPC, displayed in Fig. ??, drops significantly below $\approx 200 \text{ MeV}/c$, where energy loss and multiple scatterings start playing a role. For this reason, the ITS also runs a standalone Kalman filter algorithm, using clusters that are not associated with the TPC track. There, similarly to the TPC, candidates are considered both with and without a PV constraint.

In the second step, tracks are extrapolated to the point of closest approach (PCA) with respect to the PV and back-propagated to the TPC outer radius, using the previously added clusters. Now, track lengths are also considered and an expected time-of-flight (TOF) information is calculated based on the stored dE/dx . The tracks are then extrapolated to the Transition Radiation Detector (TRD), TOF, and possibly other detectors with clusters, where they can be matched with them. The ITS standalone tracks are propagated only to the ITS outer radius.

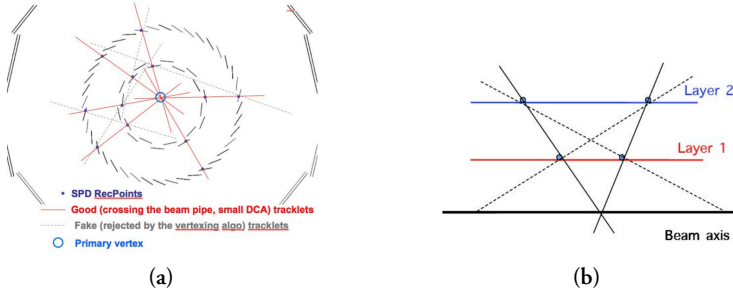


Figure 4.2: (a) Preliminary three-dimensional reconstruction of the primary vertices, also depicting tracklets rejected by the algorithm. (b) Preliminary one-dimensional reconstruction of the PVs. [141]

Finally, the tracks updated with the TRD and TOF (and possible other) information are re-fitted in each detector inwards again, starting at the TPC outer radii and propagating to the PV PCA. As a result of using the Kalmar filter, the track parameters are then finalised and given unambiguously, at the point of the primary vertex. More than 90% of the reconstructed tracks are primary tracks. This ratio can be significantly enhanced by imposing transverse and longitudinal cuts on the distance of closest approach (DCA) to the PV.

The ITS- and TPC-combined tracks enjoy the highest momentum resolution, which is plotted as a function of the track p_T in Fig. 4.4. It corresponds to values of about 1% at 1 GeV/c and then continues increasing as higher- p_T tracks are less curved, thus less constrained, and more likely to have a larger part in the detector's inactive regions. The disadvantage of the ITS-TPC tracks is their azimuthal non-uniformity due to gaps in the ITS acceptance, particularly the SPD.

Final PV determination

Subsequently, the ITS-TPC *global* tracks are used to determine the PV with a higher precision than when using the SPD tracklets alone. Tracks are also weighted to minimise the effect of outliers and the nominal beam position can also be used as a space point. In high pile-up runs, an iterative vertex process is performed. Standard deviation of the vertex position in the transverse region ranges from ~ 1 mm in events with one track to ~ 0.1 mm in events with five tracks and more.

4.2.3 Finding secondary vertices

After the track and primary vertex reconstruction, an algorithm is ran to find secondary vertices corresponding to photon pair conversions, the so-called V^0 s (weak

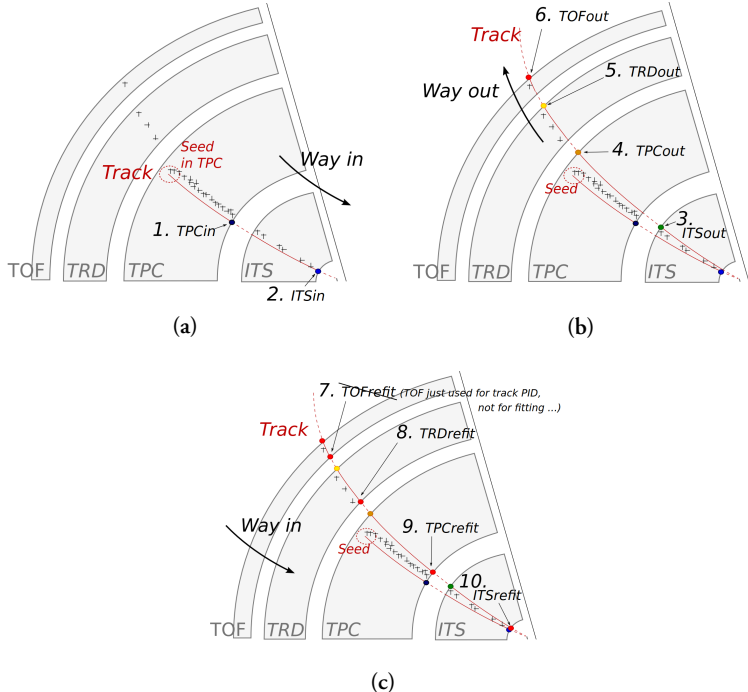


Figure 4.3: Diagrams illustrating the inward-outward-inward approach in central barrel tracking. (a) First: track seeding and propagation to ITS and PV. (b) Second: back-propagation through ITS and TPC and extrapolation to TRD and TOF. (c) Third: final re-fit. [143]

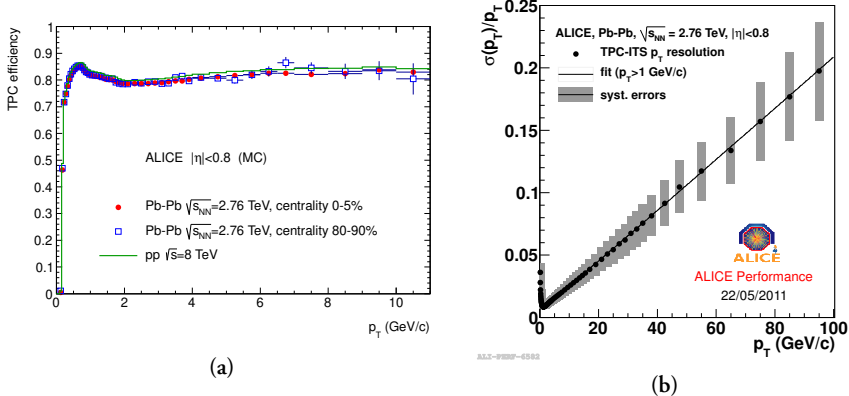


Figure 4.4: (a) Efficiency of track finding in the TPC for primary particles in pp collisions (green) and Pb-Pb collisions at different centralities (blue and red), determined from simulations. [132] (b) Transverse momentum resolution of the combined ITS-TPC tracking in Pb-Pb collisions. [144]

decays of e.g. the K_S^0 and Λ) and the so-called *cascades* (Ξ and Ω), based on the topology shown in Fig. 4.5. First, pairs of unlike-signed tracks with a given DCA

with respect to the PV are formed (more than 0.5 mm in pp or 1.0 mm in Pb-Pb). Furthermore, loose cuts on the topology of the decay (discussed in more detail in Chapter ??) are imposed. Specifically,

1. the PCA of the two tracks with respect to each other needs to be closer to the PV than the inner-most cluster of either of them, which corresponds to the fact that the daughters are produced in the vertex,
2. the DCA of the two tracks needs to be smaller than 1.5 cm,
3. if the two-track momentum exceeds $p_T > 1.5 \text{ GeV}/c$, cosine of the *pointing angle* (CPA) between the formed momentum vector and the straight line connecting the two-track PCA and the PV needs to be larger than 0.9.

The V^0 s search can occur “online” during the tracking, using a full information of the clusters, or “offline”, at a later stage, where it is based on the reconstructed tracks and can be re-configured. Subsequently, a search for cascades is performed: the found secondary vertices are matched with other secondary *bachelor* tracks if

1. the invariant mass of the found pair is consistent with that of a Λ , assuming a p and π mass hypothesis for the two tracks,
2. the bachelor DCA to the PV exceeds 0.2 cm.

4.3 Centrality and multiplicity measurements and their caveats

In Pb-Pb collisions, the experimentally measured multiplicity can be related to the centrality using the Glauber picture, as discussed in Chapter ??, which maps the final state to the percentage of the total hadronic cross section based on the collision geometry. This picture assumes that the multiplicity due to the different N_{part} dominates over contributions from specific event sub-structures (e.g. a hard jet), and that the effect of fluctuations is small enough to play a role. In ALICE, this procedure is performed typically using the V0M estimator (as it has the highest centrality resolution [132]). The V0M is a summed amplitude in the two V0A and V0C forward-rapidity scintillators, and the mapping procedure is discussed in detail in e.g. Ref. [145].

Apart from the V0M, multiplicity can also be estimated at mid-rapidity, using the SPD, which allows for taking into account particles with even very low momenta. This can be defined as either

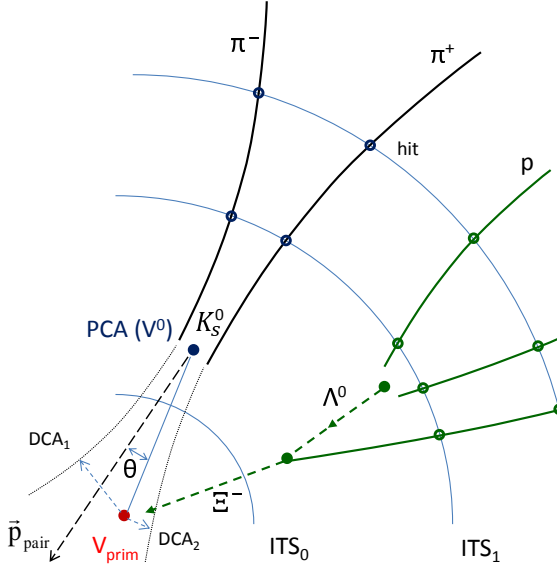


Figure 4.5: Diagram showing topology of a V^0 decay (in this case K_S^0) and a cascade decay (in this case Ξ) in the central barrel. Here, the decays occurred within the ITS volume, but this is not a requirement for the reconstruction. The radii are not to scale. [132]

- the number of clusters in the first layer of the SPD, also known as CL1,
- or the number of formed tracklets in the SPD at $|\eta| < 0.8$. This is also used in the studies done in this thesis and is referred to as N_{SPDTrkts} .

In pp collisions, the choice of mid-rapidity estimators comes with an important caveat when measuring particle spectra. Since event classification and tracking are performed in the same region, and fluctuations are not negligible compared to the multiplicities, an auto-correlation bias occurs. This can be seen in Fig. 4.6, which compares the integrated yields of charged kaons to neutral K_S^0 , scaled by a factor of two. As the multiplicity increases, the two yields become different, because requiring a large number of charged particles to classify the event as high multiplicity biases the charged kaon yields to higher values.

Furthermore, it should be noted that apart from this auto-correlation bias, spectra measured as a function of mid-rapidity and forward-rapidity multiplicity may still exhibit differences, as the choice of rapidity also plays a role when accessing and classifying the underlying dynamics of particle production in the event. This is illustrated in Fig. 4.7, which shows a different dependence of the mean number of MPIs $\langle n_{\text{MPI}} \rangle$ in Pythia 8 on the multiplicity selected by the two classifiers.

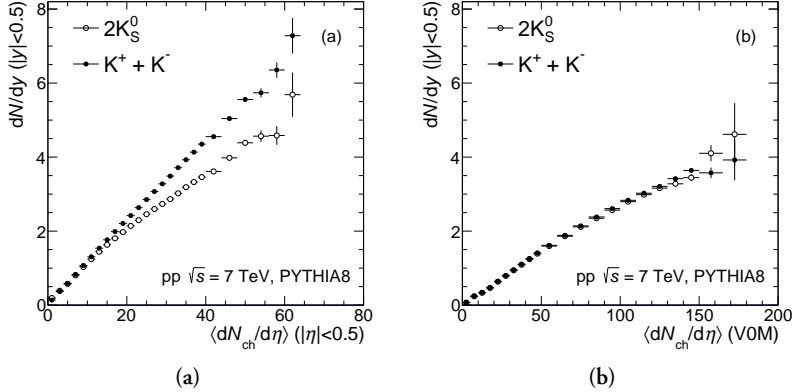


Figure 4.6: Dependence of charged and neutral kaon yields in pp collisions on the multiplicity determined **(a)** at mid-rapidity using the N_{SPD_Trkts} estimator and **(b)** at forward rapidity using the V0M estimator, as simulated by Pythia 8. [146]

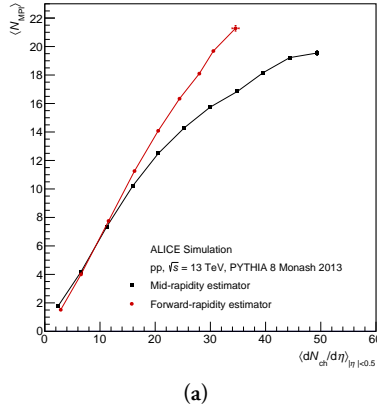


Figure 4.7: Mean number of MPIs as a function of multiplicity determined at mid-rapidity (black) and forward rapidity (red) in pp collisions at $\sqrt{s} = 13$ TeV, as simulated by Pythia 8. [62]

4.4 Used tracks

The following tracks are often used in ALICE analyses and in the measurements within this dissertation:

- **ITSTPC2011:** The highest-quality ITS-TPC tracks, also referred to as “global” tracks. They require TPC and ITS re-fit, TPC goodness-of-fit $\chi^2/n_{\text{cluster}}^{\text{TPC}} < 4$, ITS goodness-of-fit $\chi^2/n_{\text{cluster}}^{\text{ITS}} < 36$, 70 crossed TPC rows, minimum 80% of findable clusters based on geometrical considerations, clusters in the SPD,

longitudinal DCA to the PV within 2 cm, and no associated kink topology¹.

- **TPCOnly:** Tracks with better azimuthal uniformity, which require TPC goodness-of-fit $\chi^2/n_{\text{cluster}}^{\text{TPC}} < 4$, 50 crossed TPC rows, longitudinal DCA to the PV within 3.2 cm, transverse DCA to the PV within 2.4 cm, and no associated kink topology.
- **V0daughter:** Secondary tracks used to find candidates for weakly-decaying K_S^0 and Λ (discussed further in Chapter ??), representing their charged daughters. They require a TPC re-fit, 70 crossed TPC rows, and no kink topology.
- Hybrid tracks: discussed below.

4.4.1 Hybrid tracks

For measurements requiring high track quality and momentum precision, such as for particle p_T spectra, the ITS-TPC tracks are usually used. As mentioned, these suffer from azimuthal non-uniformity due to the SPD acceptance. In situations where this is unacceptable, such as when using event shape observables or azimuthal topology classifications, “hybrid tracks” can be used instead. These correspond to a union of ITS-TPC tracks and *complementary tracks*, which are subjected to identical requirements save for the SPD cluster information. Furthermore, they must be constrained to the PV. A track can be classified as complementary only if it does not pass the ITS-TPC cuts first.

This union significantly improves the azimuthal uniformity, as displayed in Fig. 4.8.

4.4.2 Geometrical cuts on tracks

In measurements using a high-momentum trigger particle, additional geometrical constraints can be utilised to ensure the low-curvature particle trajectory does not significantly cover an inactive sector of the TPC.

In order to have just one set of requirements independent of the magnetic polarity and the particle charge, the azimuthal $\phi' = \phi$ is modified:

1. if $B < 0$, then $\phi' = 2\pi - \phi'$,
2. then if $q < 0$, then $\phi' = 2\pi - \phi'$,

¹In ALICE, decays of charged particles into one charged and one neutral daughter, e.g. $\pi^- \rightarrow \mu^- \bar{\nu}_\mu$, can be identified in the TPC from a characteristic “kink” topology.

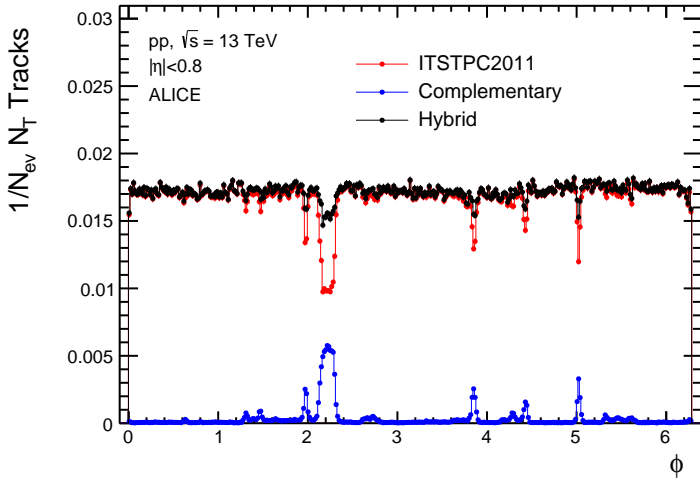
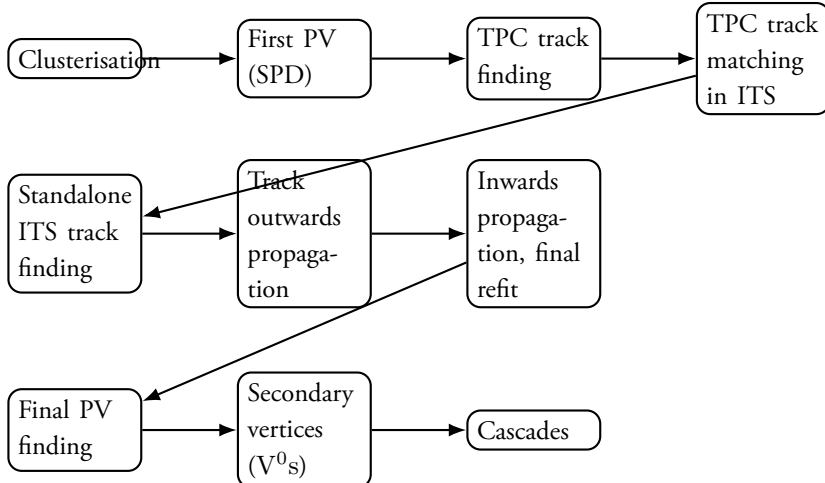


Figure 4.8: Azimuthal distributions of the standard ITS-TPC tracks (red), complementary tracks (blue), and their union: hybrid tracks (black), in events used for measurements presented in this thesis.

3. and finally, $\phi' = \phi' + \frac{\pi}{18}$.

Subsequently, the following cut is applied to reject tracks:

1. if $(\phi' \bmod \frac{\pi}{9}) < 0.12/p_T + \frac{\pi}{18} + 0.035$,
2. AND if $(\phi' \bmod \frac{\pi}{9}) > 0.1/p_T^2 + \frac{\pi}{18} - 0.025$.



Part III

Author's measurements

Chapter 5

Reconstruction of neutral strange particles with ALICE

Hadrons K_S^0 and Λ ($\bar{\Lambda}$) are unstable neutral primary particles that usually decay within the volume of the detector through the weak interaction. Their mean lifetimes are $\sim 2.7 \text{ cm}/c$ and $\sim 7.9 \text{ cm}/c$, respectively.[147] Their dominant decay channels, which are also used for their measurement, are:

$$K_S^0 \rightarrow \pi^+ \pi^- \quad (5.1)$$

$$\Lambda \rightarrow p \pi^- \quad (5.2)$$

$$\bar{\Lambda} \rightarrow \bar{p} \pi^+ . \quad (5.3)$$

Because of how these hadrons' decay topologies appear in the detector (an undetectable neutral particle decaying into a V-shaped pair of detectable tracks), they are commonly nicknamed V^0S^1 .

5.1 Analysed datasets

TBA Description of data, collection years, some QA Monte Carlo The Monte Carlo data are simulated using a physics event generator (in this measurement, Pythia 8[29]) and a model describing the propagation of particles through the detector environment (GEANT[148, 149]).

¹Not to be confused with V0A and V0C—the forward calorimeters in ALICE, or V0M—the related multiplicity estimator using the calorimeters' signal.

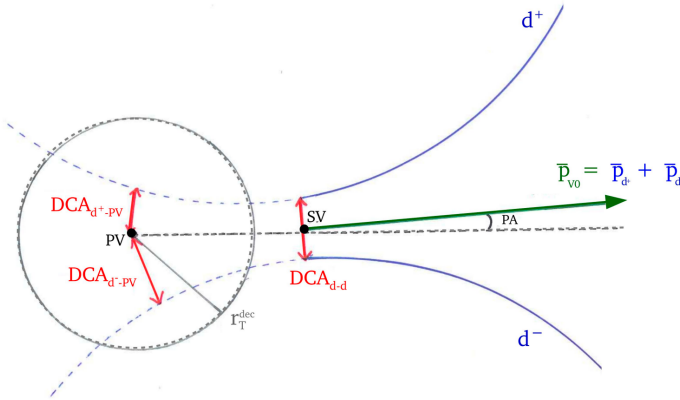


Figure 5.1: Typical topology of V^0 decay. PV stands for primary vertex, SV for secondary vertex. [? , p. 102]

5.2 Identification of V^0 s using ALICE

A centrally developed ALICE algorithm, the ALICE V^0 finder, is used to collect suitable V^0 candidates from pairs of oppositely charged tracks with the relevant topology. This typical topology is illustrated in Fig. ?? Additional selection criteria (“cuts”) are further applied to suppress the background among those candidates. These include:

- cuts on kinematics of the mother and the daughters,
- constraints on the topology of the decay,
- constraints on the reconstruction quality of the daughter tracks,
- cuts on the specific ionisation energy loss of the daughters,
- rejection of contributions from pile-up using “fast detector” information,
- rejection of other competing V^0 candidates based on their invariant mass.

The full list of used cuts is listed in Tab. 5.1.

5.3 Signal extraction

The V^0 signal is separated from the background in distributions of M_{inv} in several p_T intervals using the so-called sideband method. Assuming the signal peaks around $\Delta m_{V0} = M_{\text{inv}} - M_{V0} = 0$ and approximating the background in this region as linear, the subsequent procedure is followed:

Table 5.1: Cuts used in the identification of the K_S^0 , Λ , and $\bar{\Lambda}$ particles.

Cut Variable	Cut Value for K_S^0 (Λ , $\bar{\Lambda}$)
Topology	
V^0 pseudorapidity	$-0.8 < \eta < 0.8$
Transverse momentum	$1.0 < p_T < 25.0 \text{ GeV}/c$
V^0 DCA	$\text{DCA}^{d-d} < 1.0$
Pointing angle	$\cos \text{PA} > 0.97(0.995)$
Decay radius	$0.5 \text{ cm} < R_{xy}$
Daughter Tracks Selection	
DCA of daughters to PV	$\text{DCA}_{xy}^{\text{d-PV}} > 0.06 \text{ cm}$
TPC PID of daughters	$< 5\sigma$
Track pseudorapidity	$-0.8 < \eta < 0.8$
TPC crossed rows	$N_{\text{cr}} > 70$
TPC crossed rows to findable ratio	$N_{\text{cr}}/N_f > 0.8$
Candidate Selection	
Proper lifetime (transverse)	$(R_{xy} \times m_{(\Lambda, \bar{\Lambda})}/p_T < 30 \text{ cm})$
Competing mass	$> 4\sigma$

- the sideband regions are defined. The M_{inv} spectra are fitted in the $-0.03 < M_{\text{inv}} < -0.03 \text{ GeV}/c^2$ interval using a χ^2 -fit with the distribution

$$f = [0] + [1] \cdot M_{\text{inv}} + [2] \cdot \mathcal{N}(\mu, \sigma_1^2) + [3] \cdot \mathcal{N}(\mu, \sigma_2^2), \quad (5.4)$$

where \mathcal{N} is a Gaussian distribution. This is done in all p_T bins and illustrated in Fig. 5.4.

- In each p_T bin, parameter σ is obtained as the RMS of $[2] \cdot \mathcal{N}(\mu, \sigma_1^2) + [3] \cdot \mathcal{N}(\mu, \sigma_2^2)$. To calculate the RMS, the distribution is sampled 10^5 times.
- Variables μ_{V^0} and σ_{V^0} as functions of p_T are interpolated using χ^2 fit and the parametrisations:

$$\mu_{K_S^0}(p_T) = \begin{cases} [0] + [1] \cdot p_T + [2] \cdot p_T^2 & \text{if } p_T < 1.6 \text{ GeV}/c, \\ [3] & \text{if } p_T \geq 1.6 \text{ GeV}/c, \end{cases} \quad (5.5)$$

$$\mu_{\Lambda, \bar{\Lambda}}(p_T) = \begin{cases} [0] + [1] \cdot p_T + [2] \cdot p_T^2 & \text{if } p_T < 1.9 \text{ GeV}/c, \\ [3] + [4] \cdot p_T & \text{if } p_T \geq 1.9 \text{ GeV}/c, \end{cases} \quad (5.6)$$

$$\sigma_{V^0}(p_T) = [0] + [1] \cdot p_T + \frac{[2]}{p_T}. \quad (5.7)$$

The fitted parametrisations can be seen in Fig. 5.3.

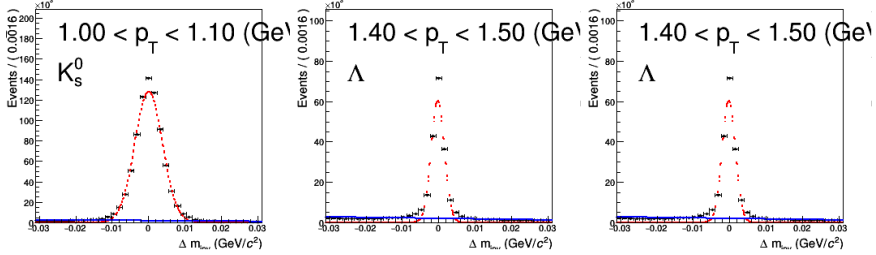


Figure 5.2: Determination of the signal peak mean and width using a fit of the Gaussian distribution for K_S^0 , Λ , and $\bar{\Lambda}$ particles.

4. In each p_T bin, we define the signal region N as $(\mu_{V0} - 6\sigma_{V0}; \mu_{V0} + 6\sigma_{V0})$ and the sidebands A and B as $(\mu_{V0} - 12\sigma_{V0}; \mu_{V0} - 6\sigma_{V0})$ and $(\mu_{V0} + 6\sigma_{V0}; \mu_{V0} + 12\sigma_{V0})$. In these regions, we sum together the entries and acquire N, A, B . The choice of $6\sigma_{V0}$ is rather liberal to avoid biases from incorrect determination of the μ_{V0} or the imperfect description of the signal peak width σ_{V0}
5. Since the background is assumed to be linear, the sum of the two sideband integrals is an accurate estimation of the background in the signal region. Particle yields Y and the corresponding statistical uncertainties σ_Y are calculated as

$$Y = N - A - B \quad (5.8)$$

$$\sigma_Y = \sqrt{N + A + B} , \quad (5.9)$$

due to the fact that the statistical uncertainties in the signal and sideband regions are fully uncorrelated. Illustrations of this step can be seen in Fig. ??.

5.3.1 Validation using simulations

The accuracy of the sideband method is tested with “MC closure”—in MC simulated data, the p_T -spectra acquired blindly from the V^0 candidates are compared with p_T -spectra of identified V^0 . The ratios can be seen in Fig. ?? and show a $\sim 5\%$ effect at high- p_T . This is caused by the fact that in ALICE MC simulations, the V^0 mass peaks have somewhat longer tails than in data and thus the signal can enter the background regions. This has to be taken into account when defining reconstruction efficiency using MC data.

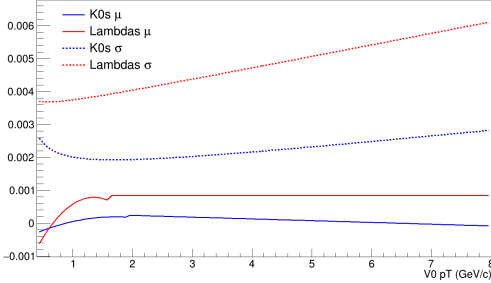


Figure 5.3: Parametrisation of the signal peak mean and width as a function of p_T .

Alternative approach

Originally, methods involving a likelihood fit and an unbinned likelihood fit of two Gaussian distributions as well as other background descriptions were tested. However, although more sophisticated, these methods proved considerably less precise. This is due to the fact that the signal peaks cannot be accurately described by the two Gaussian distributions, particularly in highly populated p_T bins. That said, they are sufficient to determine the σ_{V^0} for above-stated purposes.

Mass resolution of secondary Λ and $\bar{\Lambda}$ particles

Approximately 20% of the Λ yields measured are produced as secondary particles coming from decays of the Ξ baryon in most cases – also called feeddown. Investigations of the simulated data revealed that the invariant mass of these secondaries suffers from a worse resolution (ca. 3 times higher σ). Subsequently, this gives our signal extraction a ca. 75% efficiency for secondaries, and ca. 95% efficiency for inclusive Λ yields at intermediate p_T . This has to be taken into consideration when calculating corrections for the feeddown yields. This effect can be seen in Fig. 5.5.

5.4 Normalisation

The reconstructed K_S^0 , Λ , and $\bar{\Lambda}$ yields $Y(\eta, p_T)$ are normalised according to

$$\frac{d^2N^{\text{raw}}}{dydp_T} = \frac{1}{N_{\text{ev}}} \frac{1}{J} \frac{1}{\Delta\eta} \frac{1}{\Delta p_T} Y(\eta, p_T) \quad , \quad (5.10)$$

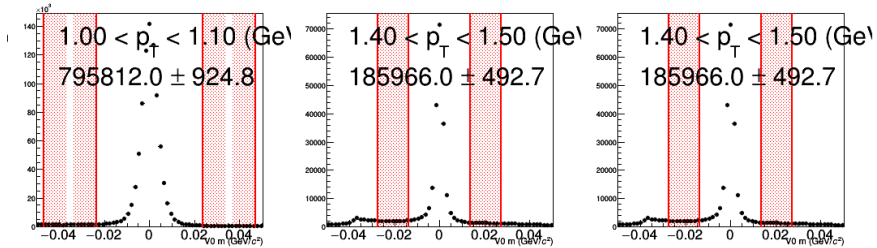


Figure 5.4: Visualisation of the sideband regions, from which the background is estimated, for K_S^0 , Λ , and $\bar{\Lambda}$ particles.

where N_{ev} is the number of selected events, J the Jacobian of the $\eta \rightarrow y$ transformation, and $\Delta\eta$ and Δp_T the widths of the pseudorapidity and transverse momentum intervals, respectively.

TBA Jacobian

TBA Event loss correction

5.5 Corrections to the reconstructed production

To acquire results with scientific relevance, the raw yields of V^0 s observed with ALICE need to be corrected for geometrical acceptance, detector effects, and, in the case of Λ ($\bar{\Lambda}$), also for secondary contribution.

5.5.1 Secondary contribution correction

Only ca. 80% of the measured inclusive Λ and $\bar{\Lambda}$ yields are produced directly in the pp collision or near-instantaneously in non-weak decays of resonances, as primary particles. The remainder is produced secondarily, as products of weak decays of heavier baryons. The dominant, and the only relevant, reactions are:

$$\Xi^- \rightarrow \Lambda \pi^- , \quad (5.11)$$

$$\Xi^0 \rightarrow \Lambda \pi^0 , \quad (5.12)$$

$$\Xi^+ \rightarrow \bar{\Lambda} \pi^+ , \quad (5.13)$$

$$\Xi^0 \rightarrow \bar{\Lambda} \pi^0 . \quad (5.14)$$

For the K_S^0 , the secondary production (such as from ϕ mesons) is negligible.

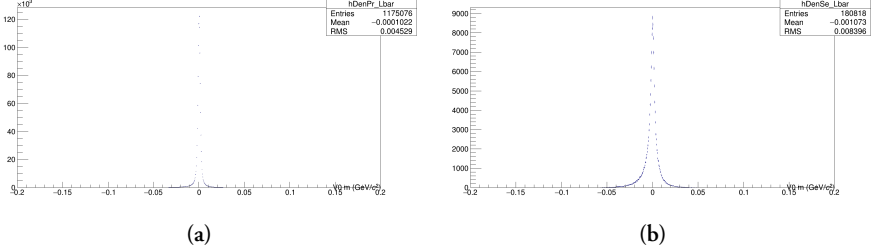


Figure 5.5: TBA.

The primary Λ yields can be estimated using the following equation,

$$\Lambda^{\text{raw}}(p_T^i) = \Lambda_{\text{measured}}^{\text{raw}} - \Lambda_{\text{secondary}}^{\text{raw}} \quad (5.15)$$

$$= \Lambda_{\text{measured}}^{\text{raw}} - \sum_j F_{ij}^\Lambda \int_{p_T^j} dN \frac{dN}{dp_T}(\Xi^-) \quad , \quad (5.16)$$

where F_{ij} is the so-called feeddown matrix giving the probabilities of a produced Ξ^- or Ξ^0 particle in a p_T interval j decaying into reconstructed Λ in a p_T interval i , and $\frac{dN}{dp_T}(\Xi^-)$ the measured Ξ^- spectra. This approach assumes that the Ξ^0 decay contribution is identical to Ξ^- and is used because Ξ^0 baryons are challenging to measure. For the $\bar{\Lambda}$, the equation is analogous but uses Ξ^+ .

The feeddown matrix is calculated in ALICE MC simulations of MB events,

$$F_{ij}^\Lambda = 2 \cdot \frac{N_{\text{rec.}}(\Lambda)|_{p_T^\Lambda=i}^{p_T^\Xi=j}}{N_{\text{gen.}}(\Xi)|_{p_T^\Xi=j}} \quad , \quad (5.17)$$

where Ξ represent both Ξ^- and Ξ^0 . There is an assumption that the probabilities, and thus, the matrix, do not depend on multiplicity of the event. It is taken into account in systematic uncertainties.

An alternative approach is constructing F_{ij}^Λ from charged Ξ solely, and then multiplying $\Lambda_{\text{secondary}}^{\text{raw}}$ by two and was used to determine the systematic uncertainty.

As discussed previously, due to the worse mass resolution of secondary Λ , a M_{inv} cut of $5\sigma_{V0}$ (determined in the sideband definition procedure). Since a large amount of the secondaries enter the background regions, a negative weight -1 has to be applied to achieve the best MC closure validation. Other configurations ($6\sigma_{V0}$ and -1 weight, $4\sigma_{V0}$ and 0 weight) were also tested.

The feeddown matrices F_{ij}^Λ , $F_{ij}^{\bar{\Lambda}}$ are displayed in Fig. 5.6.

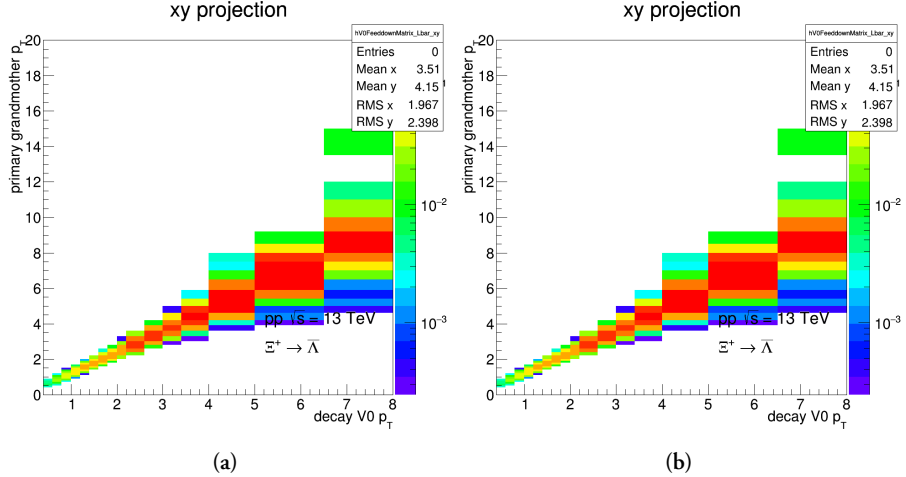


Figure 5.6: Feeddown matrices (a) F_{ij}^Λ and (b) $F_{ij}^{\bar{\Lambda}}$ from Ξ baryons.

Ξ spectra

Fitting. TBA

5.5.2 Reconstruction efficiency

The total reconstruction efficiency, including the acceptance, for V^0 s in our events with ALICE can be determined using the Monte Carlo simulated data. It is calculated as

$$\epsilon(p_T) = \text{acceptance} \times \epsilon_{\text{rec}} \quad (5.18)$$

$$= \frac{\# \text{ associated reconstructed } V^0\text{s}}{\# \text{ generated } V^0\text{s within } |\eta| < 0.8}, \quad (5.19)$$

in events that passed the selection criteria. The association is done by comparing the mother's and daughters' PDG ID as well as the MC generator label. Particles in the numerator have to satisfy all selection cuts. The reconstruction efficiency for K_S^0 , Λ , and $\bar{\Lambda}$ is plotted in Fig. 5.8.

As mentioned before, in ALICE simulations, the M_{inv} resolution worsens with increasing p_T ; in high- p_T bins, the simulated V^0 s are sometimes reconstructed with higher M_{inv} than what is considered realistic. This would lead to a lower efficiency as those V^0 s can fall out of the signal region, and an overestimation of the total measured spectra. For this reason, a $4\sigma_{V^0}$ cut is required for the V^0 s M_{inv} in the numerator.

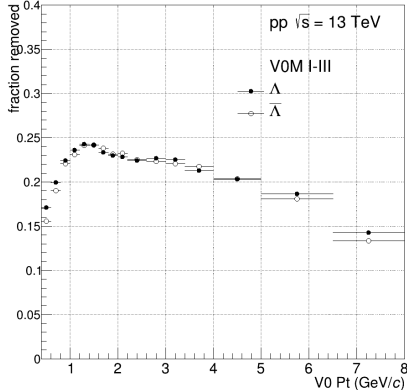


Figure 5.7: TBA.

Alternatively, one could use a cut of $6\sigma_{V0}$ and applying a negative weight -1 in cases where it is not satisfied.

The reconstruction efficiency is defined in MB events, assuming the reconstruction in pp collisions does not largely depend on multiplicity, geometrical event classification, or event sub-structure. This assumption is taken into account in systematic uncertainties.

5.6 Transverse momentum spectra

Using the corrections on the normalised yields, one acquires the measured transverse momentum spectra, which are comparable with production cross sections and thus theoretical predictions.

$$\frac{d^2N}{dydp_T} = \epsilon(p_T) \times \frac{d^2N_{\text{primary}}^{\text{raw}}}{dydp_T} \quad (5.20)$$

5.6.1 Comparisons with previously published results

The acquired results were tested against previously published measurements of K_S^0 , Λ , and $\bar{\Lambda}$ transverse momentum spectra at the ALICE experiment in MB as well as high-multiplicity (V0M I and V0M III) events in pp collisions at $\sqrt{s} = 13$ TeV.

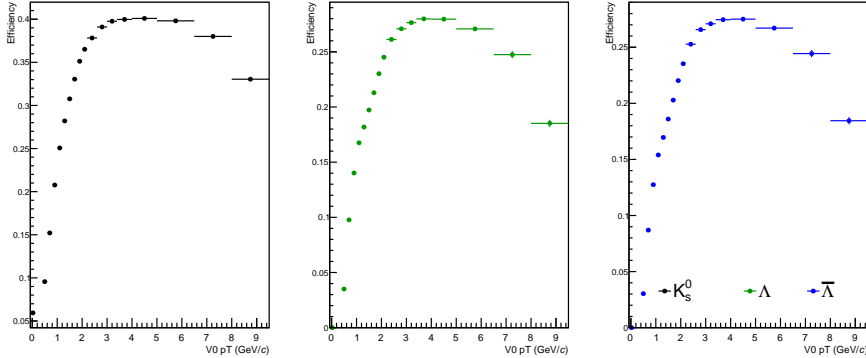


Figure 5.8: TBA.

$$K_S^0$$

The published K_S^0 results were measured in kINT7 events. [] Thus, in order to compare on an equal footing, a trigger efficiency scaling factor $\epsilon_{\text{trig}} = 0.7448$, taken over from [], was applied to this analysis.

The comparison of this analysis to the published results can be seen in Fig. 5.9a. In high-multiplicity events, the spectra are in a good agreement across the entire p_T range (most points lie within $\sim 5\%$ difference). In MB events, there is a difference ($\sim 10\%$) at the lowest p_T values. This is understood as a loss of signal in events with no reconstructed charged tracks and is usually corrected for. Since the correction plays a role only in MB – events which are of little interest to this thesis’ work – it is not taken into account.

$$\Lambda + \bar{\Lambda}$$

The published $\Lambda + \bar{\Lambda}$ results were measured in same events as this analysis, (INEL>0), therefore, ϵ_{trig} was not applied. [] They are compared to this analysis in Fig. 5.9b and show a satisfactory agreement (most points lie within $\sim 5\%$ difference).

5.7 Systematic uncertainties

Experimentally measured values always come with uncertainties – statistical and systematic. Whereas statistical uncertainties are caused by the limited number of measurements and can be decreased by increasing the statistical sample analyzed, system-

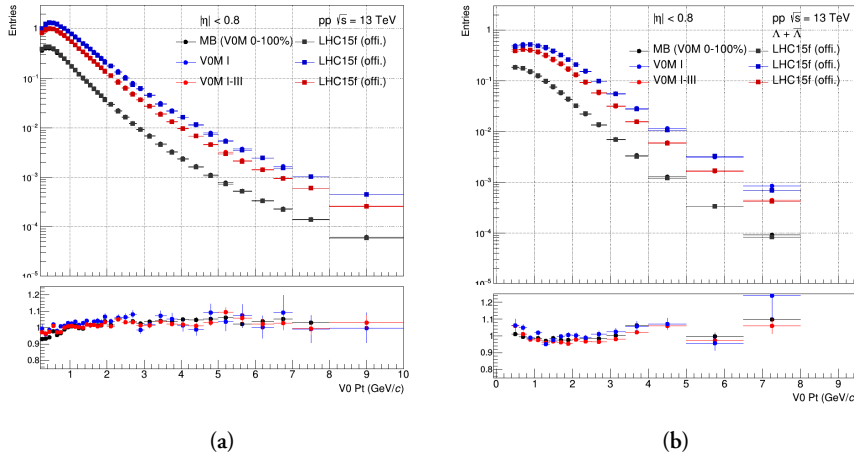


Figure 5.9: Cross-checks of this analysis' p_T spectra of (a) K_S^0 and (b) $\Lambda + \bar{\Lambda}$ in MB, VOM I, and VOM I-III events in pp collisions at against $\sqrt{s} = 13$ TeV results previously published by ALICE.

atic uncertainties represent the imprecision or the bias of the experimental methodology itself. Calculation of statistical uncertainties is given directly from frequentist statistics. Definition of systematic uncertainties, however, is not always straightforward – one cannot simply re-do the measurement with several completely different experimental setups and data analysis techniques. Therefore, a lot of effort needs to go into identifying all possible sources of systematic uncertainties.

In this measurement, the following sources of systematic uncertainty were identified as relevant:

- **Variation of selection criteria**

In determining the reconstruction efficiency, it is assumed that in ALICE MC simulations, all observables used for the identification of V^0 s and for assuring the quality of daughter tracks represent reality. Their inaccurate description, however, results in a bias. This bias is estimated by testing the sensitivity of the final results to varying the selection criteria on these observables.

- **Signal extraction method**

The biases of the sideband background estimation procedure are tested against increasing and reducing the signal and background regions, by varying the number of σ_{V^0} . Variations of 5 and 7 σ_{V^0} were used.

- **Multiplicity dependence of $\epsilon(p_T)$**

Studies of the reconstruction efficiency in pp collisions reveal a small, albeit

significant dependence on the collision final state. A constant uncertainty of $\sim 2\%$ is applied on the spectra to account for this.

- **Feeddown correction**

Three sources of uncertainty on the contribution of secondary particles were identified – variation of the Ξ yields, multiplicity dependence of the feeddown matrix, and an alternative method.

- **Material budget**

This uncertainty reflects that implementing ALICE’s material composition in simulations comes with limitations. Previous studies in ALICE [] which varied parameters of the description of the apparatus showed that this effect corresponds to a constant 4% uncertainty on the measured spectra.

When testing the default method A against an alternative method B , one can implement the deviation of the ratio of their measured values $\Delta = B/A$ from unity as an uncertainty. To ensure that this difference is statistically significant and not just an effect of a limited data sample, the deviation is considered only if it exceeds its own uncertainty, defined as

$$\sigma_\Delta = \frac{\sqrt{|\sigma_B^2 - \sigma_A^2|}}{A} , \quad (5.21)$$

where σ_A and σ_B are the uncertainties of the results from methods A and B , respectively.

5.7.1 Variation of selection criteria

To investigate the differences between description of variables in measured data and ALICE simulations, and determine sensible cut variations λ_i , raw yield loss F was studied. It was measured in MB events and defined as

$$F(\lambda) = 1 - \frac{Y(\lambda)}{Y(\lambda_0)} , \quad (5.22)$$

where $Y(\lambda)$ is the raw yield as a function of the cut value λ and λ_{LOOSEST} the loosest variation (corresponding to the highest yield).

For most observables, the systematic effect can be estimated from alternative methods using λ_{LOOSEST} and $\lambda_{\text{TIGHTEST}}$. To ensure the stability and possible non-linearity, less strict λ_{LOOSE} and λ_{TIGHT} are also tested. If applicable it is reasonable to choose λ_i such that $F(\lambda_i)$ does not exceed approximately 10%.

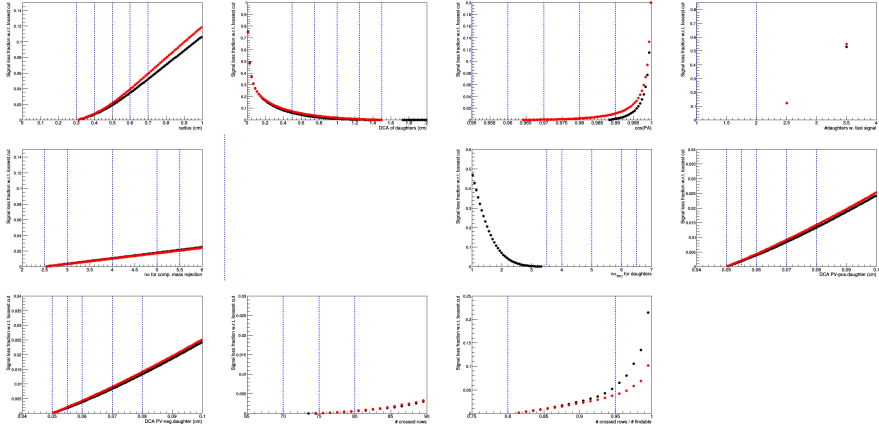


Figure 5.10: TBA

The $F(\lambda)$ for the different selection criteria, and with the chosen λ_i are shown in Fig. 5.10, Fig. 5.11, and Fig. 5.12 for K_S^0 , Λ , and $\bar{\Lambda}$, respectively. The pile-up rejection cut, which requires “fast detector” information for at least one daughter is of a binary nature. So, its variation was tested by requiring a different amount of “fast detector” hits between the two daughters. The selected values of λ_i are summarised in Tab. 5.2.

Table 5.2: Cut variation parameters for the K_S^0 (Λ and $\bar{\Lambda}$).

Quality	loosest	loose	default	tight	tightest
radius	0.3	0.4	0.5	0.6	0.7
DCA between daughters	1.5	1.25	1.0	0.75	0.5
cos PA	0.95 (0.993)	0.96 (0.994)	0.97 (0.995)	0.98 (0.996)	0.99 (0.997)
pile-up removal cut	-	-	1	2	-
comp. mass number of σ	2.5	3.0	4.0	5.0	5.5
lifetime	-	(35.0)	(30.0)	(25.0)	-
TPC PID number of σ	6.5	6.0	5.0	4.0	3.5
DCA to PV of pos. track	0.05	0.055	0.06	0.07	0.08
DCA to PV of neg. track	0.05	0.055	0.06	0.07	0.08
TPC crossed rows	-	-	70	75	80
TPC find. ratio	-	-	0.8	0.95	-

5.7.2 Feeddown correction

As mention before, first, the Ξ spectra, from which the feeddown is calculated, are varied within their reported uncertainties. In both variations, the yields are then extracted using a fit. Second, similarly to $\epsilon(p_T)$, the assumption of no multiplicity

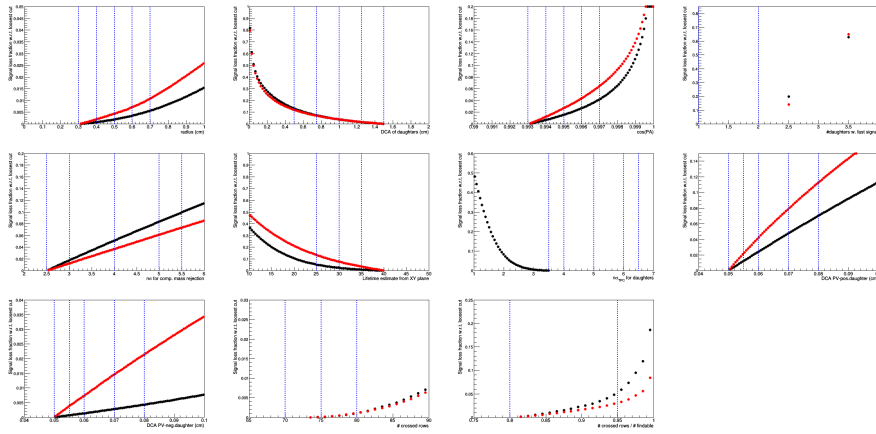


Figure 5.11: TBA

dependence of the feeddown matrix is accompanied by a constant uncertainty of 2% on the secondary yields (corresponding to ca. 0.6% uncertainty on the primary yields).

Lastly, an alternative method of estimating the feeddown just from charged Ξ baryons, and multiplying by a factor of two, was also tested and contributes a systematic uncertainty. It is considered significant and applied when $|\Delta - 1| > \sigma_\Delta$. The difference between the two methods can be seen in Fig. 5.13. It should be noted that whilst the secondary yields suffer from a rather large systematic uncertainty, the effect on the primary spectra is significantly smaller, as the uncertainties enter as $\frac{1-B}{1-A}$ and the secondary yields do not exceed $\sim 30\%$.

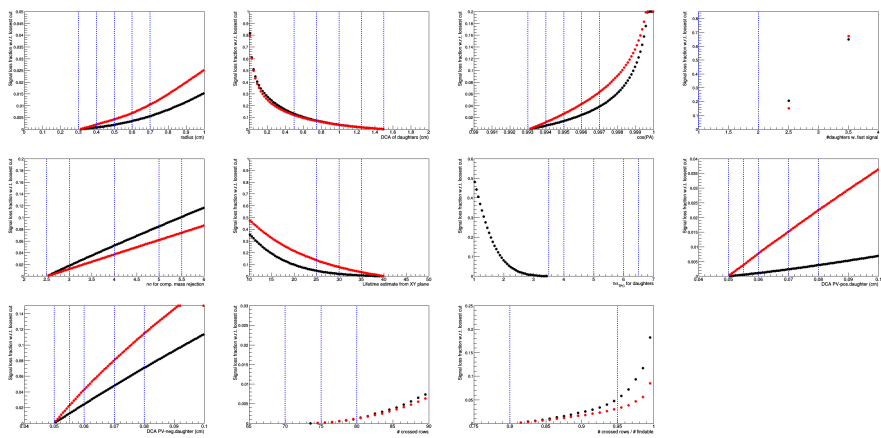


Figure 5.12: TBA

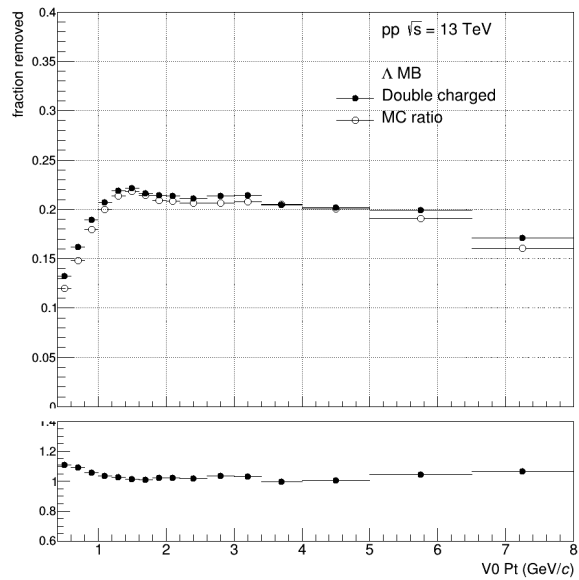


Figure 5.13: TBA

Chapter 6

Transverse Spherocity

In this chapter, measurements of K_S^0 , Λ , and $\bar{\Lambda}$ are reported as a function of transverse spherocity $S_O^{(p_T=1.0)}$, a measure of the event's topology in the transverse xy -plane.

6.1 Transverse spherocity

6.1.1 Motivation for studying event topology

As explained in Sec. 2.3, there is overwhelming evidence that some phenomena associated with QGP, such as collective flow and strangeness enhancement, also arise in pp and p–A collisions at LHC energies and high event multiplicities. This challenges the conventional assumption that the hadron densities and densities of colour fields between partons are too low to interact with each other. Consequently, high-multiplicity pp (and p–A) collisions cannot be treated as a superposition of mostly independent parton-parton (or parton-hadron) scatterings and a more in-depth approach is required to fully understand these phenomena.

Event shape observables have been used historically in lepton experiments to study fundamental QCD properties such as the gluon spin [150], and also at Tevatron and the LHC in events with very high p_T ($\gtrsim 100$ GeV/c) jets to further test pQCD predictions [151]. There are various observables, including sphericity S_T , spherocity S_O , thrust T , F-parameter, and Ellis-Karliner angle, most of which are collinear- and infrared-safe and therefore moderately easily calculable[152]. An illustration of two events with different topologies and calculated values of selected observables can be seen in Fig. 6.1.

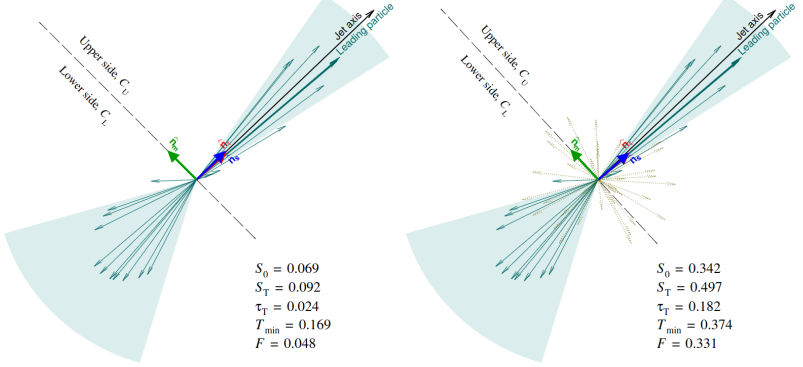


Figure 6.1: Visualisation of two events in the azimuthal plane: **(left)** more “jetty” and **(right)** more isotropic. Values for the transverse spherocity S_0 are given as well as for some other event shape observables: sphericity, thrust, thrust-minor, and F-parameter. The vector minimising the S_0 calculation is denoted as a blue arrow. [151]

With the discoveries of QGP phenomena in high-multiplicity collisions of small systems, event shape observables become attractive for different reasons. This is because pQCD (“hard”) processes are responsible for a significant fraction of particle production and are likely to impact the character of QGP phenomena in non-trivial ways. The role of non-perturbative (“soft”) processes is particularly interesting to study as their mechanisms are not fully understood and their interpretation relies on phenomenological models that require clear experimental measurements with high discriminatory power.

Event shape observables allow us to quantify events according to the dominant contributing processes. For instance, collisions with single large p_T transfer scatterings are likely to lead into events with two back-to-back, highly collimated showers, which create a pencil-like shape in the transverse plane. Conversely, collisions with multiple lower p_T transfer partonic interactions will exhibit a high degree of azimuthal isotropy. Therefore, event shape measurements help us gain a deeper understanding of high-multiplicity events and a better control over the magnitudes of the hard and soft contributions. Ultimately, these measurements may help determine whether QGP formation is necessary in small systems or uncover new physical behaviours.

6.1.2 S_0 and $S_0^{(p_T=1.0)}$ as experimental observables

Traditionally, spherocity S_0 is defined as:

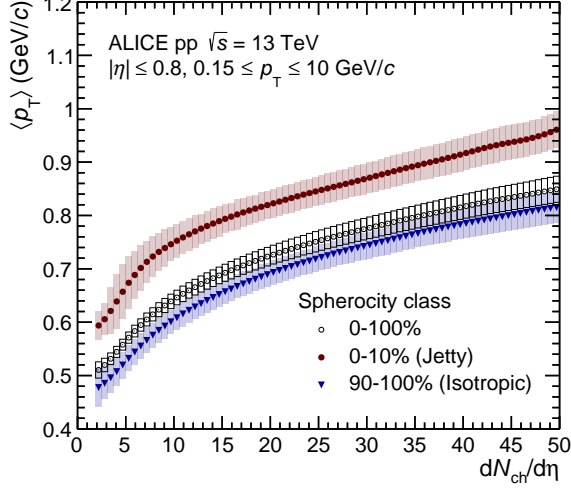


Figure 6.2: Dependence of the transverse momentum spectrum of charged particles as a function of event multiplicity at mid-rapidity. Cases for jetty, isotropic, and spherocity-unbiased events are displayed. Systematic uncertainties are indicated by the boxes and shaded areas. [153]

$$S_O = \frac{\pi^2}{4} \min_{\hat{n}} \left(\frac{\sum_i |p_{T,i} \times \hat{n}|}{\sum_i |p_{T,i}|} \right)^2 , \quad (6.1)$$

where $p_{T,i}$ represents the vector of transverse momentum of a particle i and \hat{n} is the event-dependent unit vector that minimises the sum. The sum runs over all charged particles in the event within the detector acceptance.

Previous ALICE measurements [153] studied characteristics of charged particles in pp collisions and discovered their strong dependence of $\langle p_T \rangle$ on spherocity S_O , which validates the previously discussed motivation. This relationship is shown in Fig. 6.2. Additionally, phenomenological studies of S_O in Pythia 8 further demonstrate its classifying power by finding strong dependence of $\langle n_{\text{MPI}} \rangle$ as well as the mean number of reconstructed jets $\langle n_j \rangle$ on S_O [154, 155]. These results can be seen in Fig. 6.3.

This work uses a modified definition of this observable, *unweighted* transverse spherocity $S_O^{(p_T=1.0)}$, defined as follows:

$$S_O^{(p_T=1.0)} = \frac{\pi^2}{4} \min_{\hat{n}} \left(\frac{\sum_i |\hat{p}_{T,i} \times \hat{n}|}{N_{\text{trks}}} \right)^2 , \quad (6.2)$$

where $\hat{p}_{T,i}$ represents the *unit* vector of transverse momentum of a particle i and N_{trks} the number of charged particles entering the sum.

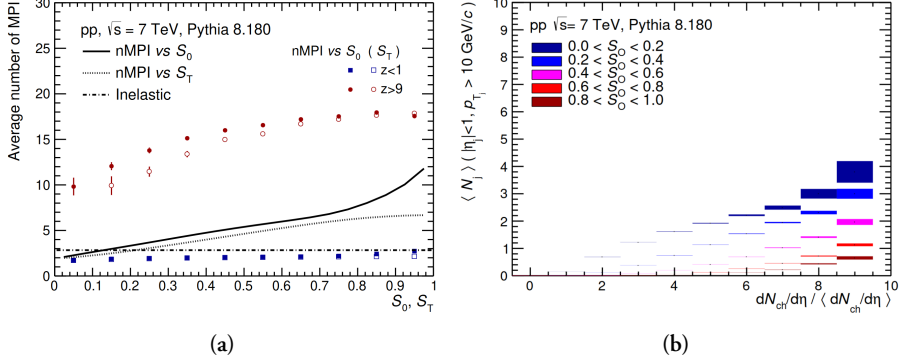


Figure 6.3: (a) Correlation between the mean number of MPIs and transverse spherocity (and sphericity) in pp collisions at $\sqrt{s} = 7$ TeV predicted by Pythia 8, shown as solid and dotted lines. The horizontal line shows the average for minimum bias inelastic events. Events with high (red) and low (blue) self-normalised event multiplicity z are also studied and depicted as datapoints. [154] (b) Average number of reconstructed jets as a function of self-normalised event multiplicity in pp collisions at $\sqrt{s} = 7$ TeV with varying values of spherocity, as predicted by Pythia 8. [155]

In this thesis, unless stated otherwise, the terms transverse spherocity and spherocity are both used to refer to this unweighted transverse spherocity $S_O^{(p_T=1.0)}$.

Applying the spherocity $S_O^{(p_T=1.0)}$, events in two geometrical limits can be studied:

- $S_O^{(p_T=1.0)} \rightarrow 0$: the “jetty” limit, where a pencil-like topology is selected. These events are dominated by hard pQCD processes. In this limit, with perfectly collimated back-to-back particles, \hat{n} aligns with them. Thus, the sum of vector products in Eq. 6.2 contains only zero values as $\sin 0 = \sin \pi = 0$.
- $S_O^{(p_T=1.0)} \rightarrow 1$: the “isotropic” limit, where a circular topology is selected. Such events are dominated by multiple softer non-perturbative processes¹. In this limit of $N \rightarrow \infty$ uniformly distributed unit vectors within $(0, 2\pi)$, the choice of \hat{n} becomes arbitrary and calculation of the sum in Eq. 6.2 leads to:

$$\frac{1}{N} \sum_{n=1}^N \left| \sin \frac{2\pi n}{N} \right| \approx \frac{1}{N} \int_0^N \left| \sin \frac{2\pi x}{N} \right| dx \quad (6.3)$$

$$= \frac{2}{N} \int_0^{N/2} \sin \frac{2\pi x}{N} dx = \frac{1}{\pi} \int_0^\pi \sin u du \quad (6.4)$$

$$= \frac{1}{\pi} [-\cos x]_0^\pi = \frac{2}{\pi} \quad (6.5)$$

¹However, it is important to mention that anisotropic collective flow such as v_2 , a non-perturbative phenomenon, reduces the event isotropy.

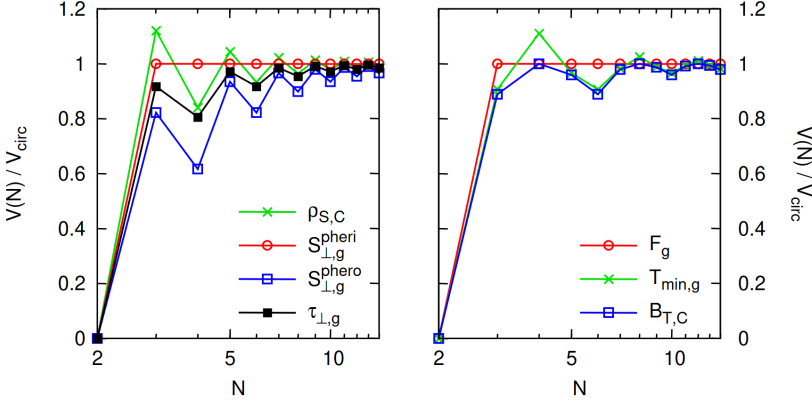


Figure 6.4: Graphs showing how rapidly the different event shape observables approach the circular limit V_{circ} corresponding to $N \rightarrow \infty$, based on the number of perfectly isotropically distributed particles N . Transverse spherocity, here denoted as $S_{\perp,g}^{\text{sphero}}$, exhibits the slowest rise, and never exceeds unity.[152]

and therefore $S_O^{(p_T=1.0)} = 1$.

Figure 6.4 illustrates how spherocity slowly approaches the circular limit value with increasing N compared to other event shape observables. This property makes spherocity favoured by experimentalists in these measurements, as it provides the highest discrimination power of isotropic events [151].

6.1.3 Relationship between $S_O^{(p_T=1.0)}$ and S_O

In ALICE, only charged particles are considered when calculating spherocities. This introduces biases when measuring charged and neutral species of hadrons. For instance, even topologically identical events with dominant high- p_T leading π^+ and π^0 can yield significantly different values of the traditional p_T -weighted spherocity S_O , despite being comparable in all relevant aspects. In contrast, unweighted spherocity $S_O^{(p_T=1.0)}$ offers a more similar quantification of the two events, as shown in Fig. 6.5. However, it should be noted that this modified definition is only applicable to events with many tracks (i.e., $N_{\text{trks}} > 10$).

In addition, while not a large concern in high-multiplicity collisions [153], $S_O^{(p_T=1.0)}$ also offers improved resolution compared to S_O , as the failure to reconstruct a high- p_T track has a smaller impact. Overall, S_O and $S_O^{(p_T=1.0)}$ exhibit similar values and interpretations, with a strong correlation between the two, as illustrated in Fig. 6.6.

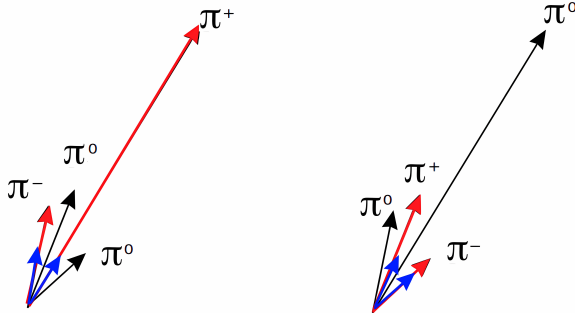


Figure 6.5: Illustration of two topologically identical events with swapped charged and neutral particles. Momentum vectors entering the p_T -weighted spherocity (red) and p_T -unweighted (blue) calculations are displaying, showing a larger difference between the two scenarios for the former than the latter. (Needs to be remade or credited)

6.1.4 Track and event selection

The measurements are carried out on MB events with $\text{INEL} > 0$, requiring at least one hit in the V0A or V0C scintillators and one charged particle reconstructed within $|\eta| < 1$. The primary vertex is reconstructed using hits in the SPD and is required to be within 10 cm of the interaction point. The fast read-out time of the SPD allows rejection of out-of-bunch pile-up. In-bunch pile-up is further removed by excluding events with multiple reconstructed vertices. The presented results are based on high-multiplicity events, selected by the classifiers V0M (forward rapidity) and $N_{\text{tracklets}}^{|\eta| < 0.8}$ (mid-rapidity), and require a minimum of 10 reconstructed tracks within $|\eta| < 0.8$ and with $p_T > 0.15 \text{ GeV}/c$.

To ensure a high level of azimuthal acceptance uniformity, which is important for event shape measurements, the following, rather loose, selection criteria are employed:

1. The SPD is not used due to its inactive sectors, at the expense of a lower momentum resolution.
2. A track is required to have at least 50 clusters in the TPC and be matched to hits in the ITS to improve tracking precision and further reject pile-up.
3. DCA cuts are applied in both the longitudinal ($|\text{DCA}_z| < 3.2 \text{ cm}$) and transverse ($|\text{DCA}_{xy}| < 2.4 \text{ cm}$) planes to ensure that the reconstructed TPC track points to the primary vertex.

It should be noted that charged decay products of V^0 s with low p_T ($\lesssim 1 \text{ GeV}/c$) and small decay radius may enter and influence $S_O^{(p_T=1.0)}$ determination.

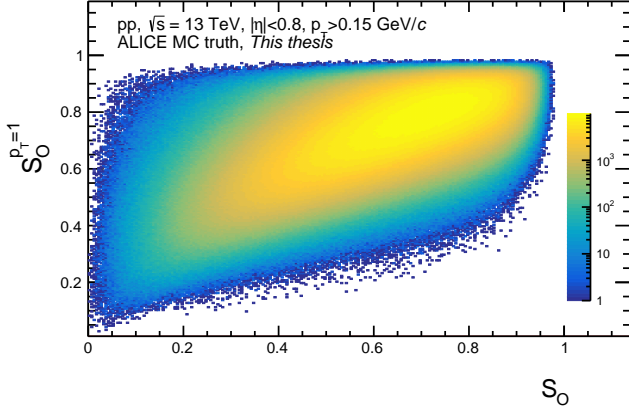


Figure 6.6: Two-dimensional histogram showing the correlation between the traditional transverse spherocity S_O and the unweighted transverse spherocity $S_O^{(p_T=1.0)}$ employed in this measurement, obtained from ALICE MC simulations.

6.1.5 Multiplicity selection and its interplay with $S_O^{(p_T=1.0)}$

Spherocity exhibits a twofold correlation with multiplicity that is not particularly informative. First, the definition of $S_O^{(p_T=1.0)}$ results in higher values for events with more uniformly distributed particles, as shown in Fig. 6.4. Second, in models such as Pythia, high multiplicity is often associated with more MPI, which tend to lead to higher isotropy due to the increased number of emission sources. To gain a more nuanced understanding of the relationship between spherocity and multiplicity, the effect of $S_O^{(p_T=1.0)}$ on measured particles was analysed in high-multiplicity events determined in two distinct rapidity regions, as described above. Specifically, the top 1% (10%) quantiles are used, denoted as V0M I and $N_{\text{SPD}_{\text{Trkts}}} \text{ I}$ (V0M I-III and $N_{\text{SPD}_{\text{Trkts}}} \text{ I-III}$).

Figure 6.7 shows the effect of $S_O^{(p_T=1.0)}$ on the pion yields and $\langle p_T \rangle$. Pions are measured in the high-multiplicity events and in top and bottom 10% and 1% quantiles of $S_O^{(p_T=1.0)}$. The result reveals that when measuring multiplicity in forward rapidity (V0M I), the effect of $S_O^{(p_T=1.0)}$ causes a change of approximately 100% in the yields when going from jetty to isotropic limits, whereas the difference in $\langle p_T \rangle$ is only about 10%. Conversely, when determining the multiplicity in mid-rapidity ($N_{\text{SPD}_{\text{Trkts}}} \text{ I}$), the same region where the pion spectra are reconstructed, the change in the yields is only approximately 10% while the change in $\langle p_T \rangle$ is approx. 25%.

For this reason, the following combinations of multiplicity and $S_O^{(p_T=1.0)}$ selections are presented:

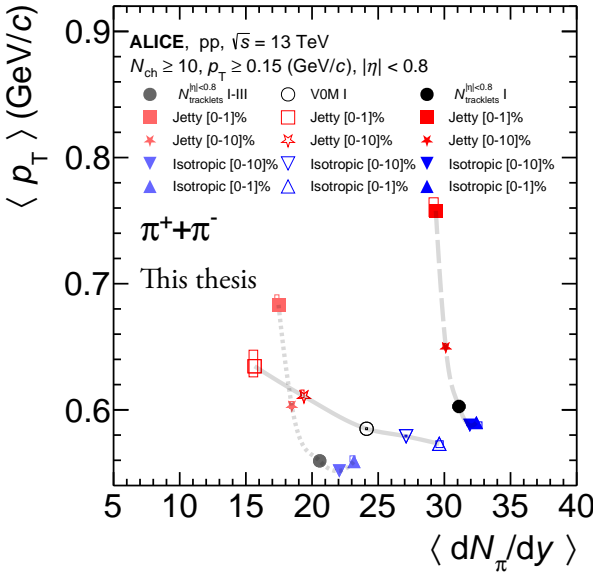


Figure 6.7: Relationship between the mean transverse momentum of charged pions and their yields in events with different $S_O^{(p_T=1.0)}$ values and event multiplicity determined at mid-rapidity (here denoted $N_{\text{tracklets}}^{|\eta|<0.8}$) and forward rapidity (VOM). Events in the same multiplicity classes are connected with lines for clarity's sake.

1. $N_{\text{SPD}_{\text{Trkts}}} \text{ I and } S_O^{(p_T=1.0)}$ top and bottom 10% quantiles: This selection emphasises the impact of extreme event topologies on the QCD processes whilst minimising the effect of multiplicity dependence.
2. $N_{\text{SPD}_{\text{Trkts}}} \text{ I-III and } S_O^{(p_T=1.0)}$ top and bottom 1% quantiles: This selection shows the effect of even more extreme event topologies but with overall less and somewhat varying multiplicity.
3. VOM I and $S_O^{(p_T=1.0)}$ top and bottom 10% quantiles: This selection highlights the effect of extreme event topologies with highly varying mid-rapidity multiplicity. It also allows for a comparison with $N_{\text{SPD}_{\text{Trkts}}} \text{ I-III and } S_O^{(p_T=1.0)}$ 1% selection, as the mid-rapidity multiplicity and the $\langle p_T \rangle$ variations are more similar.

The mid-rapidity multiplicities in the different high-multiplicity classes are reported in Tab. 6.1. The measured $S_O^{(p_T=1.0)}$ distributions in $N_{\text{SPD}_{\text{Trkts}}} \text{ I}$, $N_{\text{SPD}_{\text{Trkts}}} \text{ I-III}$, and VOM I-III are shown in Fig. 6.8. They are treated with Bayesian unfolding to account for reconstruction effects. They are also compared with theoretical predictions from

Pythia 8 (Monash [110] and Ropes [116] tunes), EPOS LHC [120], and Herwig 7 [107]. Table 6.2 provides the $S_O^{(p_T=1.0)}$ cut values associated with the quantile selections in data.

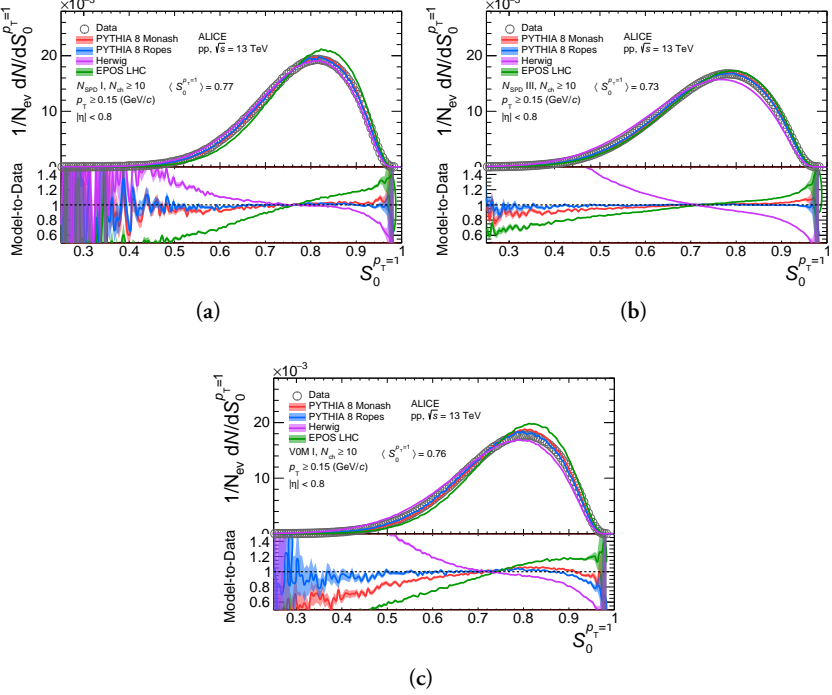


Figure 6.8: The measured and fully corrected $S_O^{(p_T=1.0)}$ distributions for both (a) $N_{\text{SPD}_{\text{Triplets}}} 0\text{--}1\%$, (b) $0\text{--}10\%$ and (c) $\text{V0M } 0\text{--}1\%$. The curves represent different model prediction, where the shaded area represents the statistical uncertainty of the models.

Table 6.1: Mean values of charged particle multiplicity at mid-rapidity in different high-multiplicity event classes.

Event class	$N_{\text{SPD}_{\text{Triplets}}} \text{ I}$	$N_{\text{SPD}_{\text{Triplets}}} \text{ I-III}$	V0M I
$\langle dN_{\text{ch}}/d\eta \rangle$	33.01 ± 0.55	21.57 ± 0.32	26.02 ± 0.35

6.1.6 Comparison of V^0 production with MC generators

Further on in this chapter, the results of K_S^0 , Λ , and $\bar{\Lambda}$ as a function of $S_O^{(p_T=1.0)}$ are presented and compared with predictions from phenomenological models Pythia 8 [29], EPOS LHC [120], and Herwig 7 [107] obtained from MC simulations. To mitigate the effect of reconstruction on the experimental results and make the com-

Table 6.2: Cut values of the different quantiles of the uncorrected $S_O^{(p_T=1.0)}$ distribution used for the event selections in this analysis.

Event class	$N_{\text{SPD}_{\text{Trkts}}} \text{ I}$	$N_{\text{SPD}_{\text{Trkts}}} \text{ I-III}$	V0M I
Jetty			
$S_O^{(p_T=1.0)} \text{ 0-1\%}$	< 0.487	< 0.408	< 0.433
$S_O^{(p_T=1.0)} \text{ 0-10\%}$	< 0.624	< 0.561	< 0.589
Isotropic			
$S_O^{(p_T=1.0)} \text{ 90-100\%}$	> 0.892	> 0.871	> 0.882
$S_O^{(p_T=1.0)} \text{ 99-100\%}$	> 0.942	> 0.930	> 0.936

parison with these predictions as comparable as possible, the following strategies were employed based on findings using the ALICE MC simulations:

- The results were compared using the same quantiles of the $S_O^{(p_T=1.0)}$ distributions in both the MC and the data, instead of relying on the experimental $S_O^{(p_T=1.0)}$ ranges determined by specific cut values. This approach reduced the effects of $S_O^{(p_T=1.0)}$ resolution.
- In the MC simulations, the $S_O^{(p_T=1.0)}$ calculations included neutral particles K_S^0 , Λ , and $\bar{\Lambda}$, despite their neutral charge. This helped minimize differences between the true and reconstructed/corrected MC results, possible due to the potential contribution of charged daughters to the $S_O^{(p_T=1.0)}$ calculation.

Any discrepancies that still persisted between the true and reconstructed/corrected transverse momentum spectra were accounted for as systematic uncertainties.

6.2 Systematic uncertainties

The systematic uncertainties associated with the p_T spectra of K_S^0 , Λ , and $\bar{\Lambda}$ were evaluated separately for $N_{\text{SPD}_{\text{Trkts}}} \text{ I}$ and V0M I events with no $S_O^{(p_T=1.0)}$ selection, as well as for the top and bottom 10% isotropic and jetty quantiles, using the methodology described in Section ???. The relative systematic uncertainties obtained from these configurations were also applied to the $N_{\text{SPD}_{\text{Trkts}}} \text{ I-III}$ and V0M I-III event classes with different jetty/isotropic quantiles.

Figures 6.9, 6.10, and 6.11 illustrate the maximal deviations of variations resulting from alternative cut values, extraction parameters, or feeddown methods in V0M I, $S_O^{(p_T=1.0)}$ -unbiased events for K_S^0 , Λ , and $\bar{\Lambda}$, respectively.

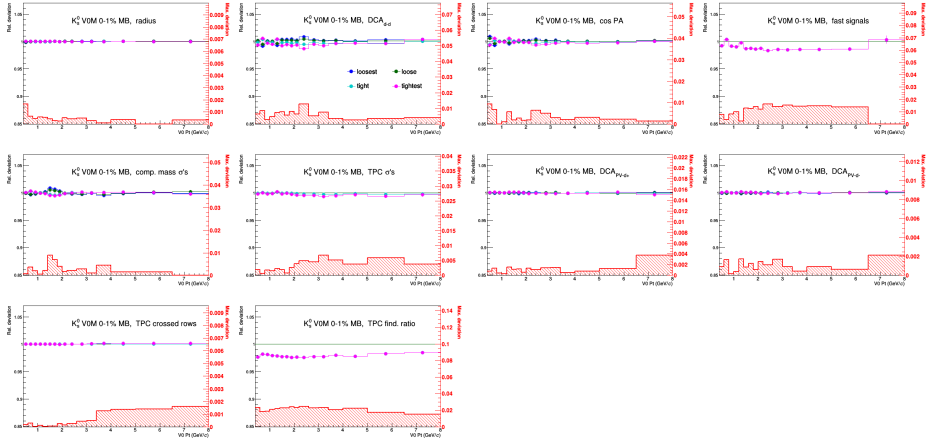


Figure 6.9: NEEDS TO BE REDRAWN IN CONSISTENT STYLE WITH RT CHAPTER: Deviations of the corrected spectra w.r.t. the different cut variations used for the K_S^0 . The maximum deviation is added in quadrature to the total, if it's larger than σ_{RB} (depicted as errorbars) from unity.

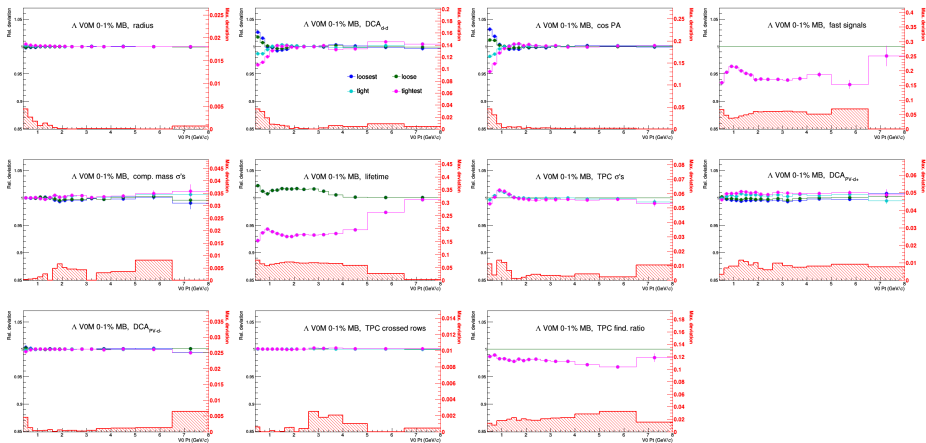


Figure 6.10: NEEDS TO BE REDRAWN IN CONSISTENT STYLE WITH RT CHAPTER: Deviations of the corrected spectra w.r.t. the different cut variations used for the K_S^0 . The maximum deviation is added in quadrature to the total, if it's larger than σ_{RB} (depicted as errorbars) from unity.

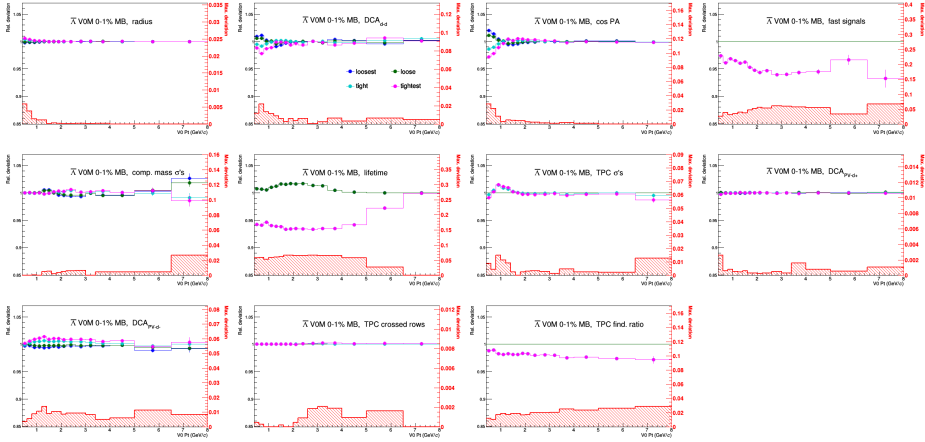


Figure 6.11: NEEDS TO BE REDRAWN IN CONSISTENT STYLE WITH RT CHAPTER: Deviations of the corrected spectra w.r.t. the different cut variations used for the K_S^0 . The maximum deviation is added in quadrature to the total, if it's larger than σ_{RB} (depicted as errorbars) from unity.

6.2.1 Experimental bias

To estimate the experimental bias of the $S_O^{(p_T=1.0)}$ selection, Monte Carlo closure tests were used, studying the ratios of true p_T spectra in jetty/isotropic quantiles of the true $S_O^{(p_T=1.0)}$ distribution to the measured and corrected p_T spectra in quantiles of the measured $S_O^{(p_T=1.0)}$ distribution.

Due to the loose DCA cuts used in the $S_O^{(p_T=1.0)}$ determination, it is expected that the V^0 daughters may enter its calculation. Thus, to make the predictions from simulations more comparable to the data, the K_S^0 , Λ , and $\bar{\Lambda}$ particles were included in the true $S_O^{(p_T=1.0)}$ calculation. Although insufficient below $p_T < 1 \text{ GeV}/c$, this works well and corresponds to 1% and 4% discrepancies for isotropic and jetty events, respectively [156].

Alternatively, as discussed further in this dissertation in the R_T measurements in Chapter 7 but not employed here, this effect could be accounted for experimentally, by making the two track sets (spherocity and V^0 daughters) explicitly disjunct by enforcing a DCA cut.

6.2.2 Correlation of uncertainties with $S_O^{(p_T=1.0)}$

Correlations of several systematic uncertainties with respect to the $S_O^{(p_T=1.0)}$ selection are expected. Since the ratios of jetty/isotropic results to $S_O^{(p_T=1.0)}$ -unbiased ones provide important insights, it is necessary to account for these correlations in order to not overestimate the uncertainties, following the methodology described in Fig. ??.

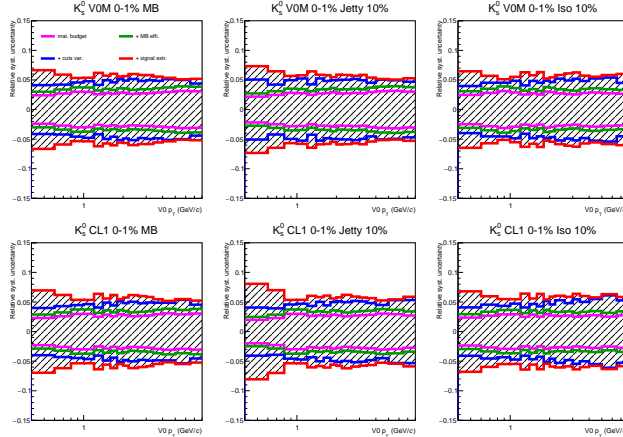
Moreover, the systematic uncertainty associated with the material budget is treated as fully correlated, while assuming the reconstruction efficiency is independent of multiplicity leads to an uncorrelated uncertainty. This assumption would lead to a factor of $\sqrt{2}$ in the ratios of jetty/isotropic to $S_O^{(p_T=1.0)}$ -unbiased for this uncertainty. However, in ALICE, this assumption is generally considered too conservative [146], and thus this factor is dropped. The same approach is used for the uncertainty associated with the multiplicity independence of the feeddown matrix. Detailed results can be found in Appendix ??.

6.2.3 Summary

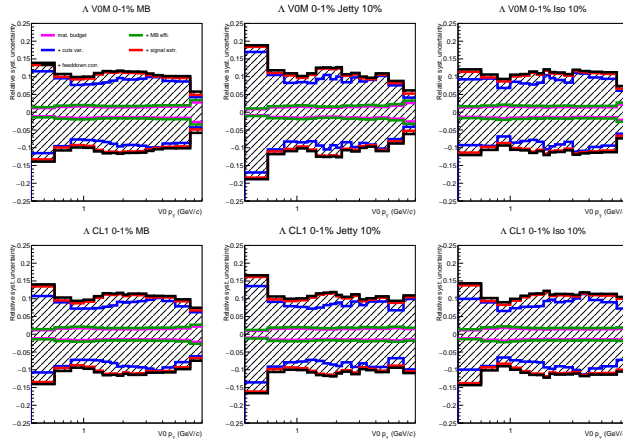
The total systematic uncertainties are reported in Tab. 6.3 and visualised in Fig. 6.12. The dominant contributions are, in no specific order, selection cuts, experimental bias, signal extraction, and the enforcement of signals from fast detectors to prevent track pile-up.

Table 6.3: The most relevant systematic uncertainties for the long-lived particles K_S^0 and $\Lambda(\bar{\Lambda})$ as a function of $S_O^{(p_T=1.0)}$. "HM" in this table represents the $S_O^{(p_T=1.0)}$ -unbiased spectra. Uncertainties are p_T -dependent, and the ranges listed represents the minimum-maximum values presented in the final spectra (see text for details).

Topology:	Jetty	Iso	HM	Jetty/HM	Iso/HM
K_S^0					
Selection cuts	3%	3–4%	3–4%	Negl.	1%
Track pile-up	1%	1–3%	1%	0–2%	0–2%
Signal extraction	1–3%	1–3%	1–3%	Negl.	Negl.
Efficiency	2%	2%	2%	2%	2%
Material budget	4%	4%	4%	—	—
Experimental bias	4%	1%	—	4%	1%
Total uncertainty	7%	6–7%	5–6%	5%	2–3%
$\Lambda(\bar{\Lambda})$					
Selection cuts	1–5%	2–6%	4–5%	0–1%	0–3%
Track pile-up	4–5%	5%	3–5%	0–1.5%	0–1%
Signal extraction	2–6%	2–6%	2–6%	0–2%	0–1%
Feed-down correction	1.0–1.5%	1.0–1.5%	1.0–1.5%	Negl.	Negl.
Efficiency	2%	2%	2%	2%	2%
Material budget	4%	4%	4%	—	—
Experimental bias	4%	1%	—	4%	1%
Total uncertainty	8–10%	8–9%	7–9%	5%	3–4%



(a)



(b)

Figure 6.12: NEEDS TO BE REDRAWN IN CONSISTENT STYLE WITH RT CHAPTER: Total relative systematic uncertainty and individual contributions for the K_S^0 , Λ , and $\bar{\Lambda}$.

6.3 Transverse momentum spectra vs. $S_O^{(p_T=1.0)}$

The corrected spectra in V0M and $N_{\text{SPD}_{\text{Trklts}}}$ high-multiplicity events and the dependence on spherocity for the K_S^0 and $\Lambda + \bar{\Lambda}$ can be seen in Fig. 6.13 and Fig. 6.14, respectively. The trends observed in the spectra are consistent between K_S^0 and Λ and indicate a significant hardening (softening) in the low (high) spherocity selection, relative to the inclusive high-multiplicity event class. These trends are qualitatively generally well captured by all included model predictions, favouring Pythia 8 Ropes. Particularly, EPOS LHC overestimates the yields and Pythia 8 Monash fails in de-

scribing the Λ p_T spectra.

The separation between jetty and isotropic events is more pronounced in the $N_{\text{SPD}_{\text{Trkts}}}$ high-multiplicity events, and shows significant difference in the spectra slopes rather than just an offset, which is somewhat the case for the V0M events.

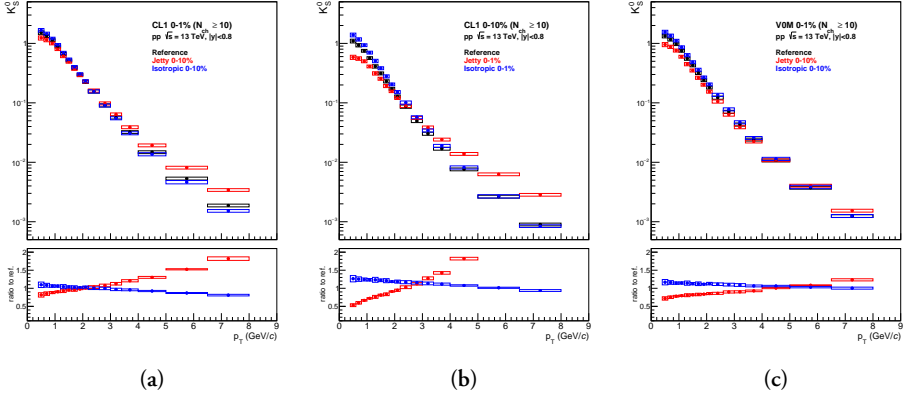


Figure 6.13: Transverse momentum spectra of K_S^0 in high-multiplicity jetty (red) and isotropic (blue) events of pp collisions at $\sqrt{s} = 13$ TeV measured in the (a) $N_{\text{SPD}_{\text{Trkts}}} \text{I}$, (b) $N_{\text{SPD}_{\text{Trkts}}} \text{I-III}$, and (c) V0M I event classes. The bottom panels display ratios to the $S_0^{(p_T=1.0)}$ -unbiased spectra. Statistical and systematic uncertainties are indicated with error bars and boxes, respectively. (Needs to be redrawn to also show MC)

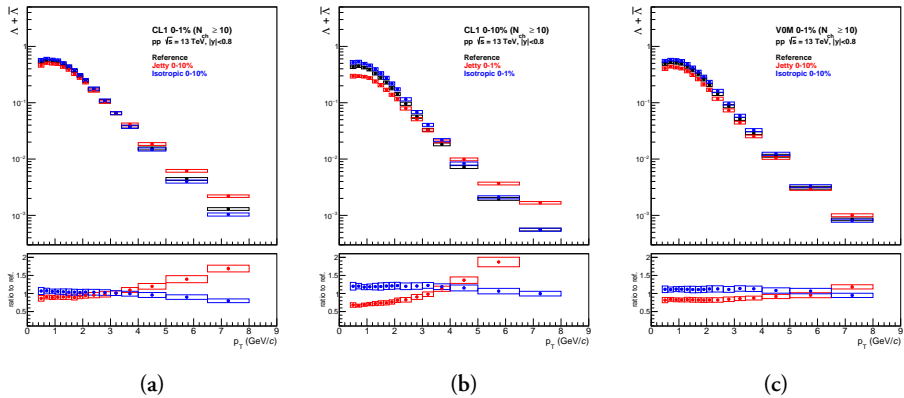


Figure 6.14: Transverse momentum spectra of $\Lambda + \bar{\Lambda}$ in high-multiplicity jetty (red) and isotropic (blue) events of pp collisions at $\sqrt{s} = 13$ TeV measured in the (a) $N_{\text{SPD}_{\text{Trkts}}} \text{I}$, (b) $N_{\text{SPD}_{\text{Trkts}}} \text{I-III}$, and (c) V0M I event classes. The bottom panels display ratios to the $S_0^{(p_T=1.0)}$ -unbiased spectra. Statistical and systematic uncertainties are indicated with error bars and boxes, respectively. (Needs to be redrawn to also show MC and be cut off from 1 GeV)

6.3.1 Ratios of neutral kaons to charged kaons

To verify the robustness of $S_O^{(p_T=1.0)}$ as an event observable, the p_T spectra of neutral and charged kaons are compared in the $N_{\text{SPD}_{\text{Trkts}}}$ I and V0M I classes. The ratios exhibit no dependence on $S_O^{(p_T=1.0)}$ and are consistent with unity, according to expectations. The slight depletion of K_S^0 in the $N_{\text{SPD}_{\text{Trkts}}}$ I class is interpreted as the multiplicity selection bias due to requiring a large number of charged tracks at mid-rapidity, and is also reproducible by simulations. The ratios are shown in Fig. 6.15.

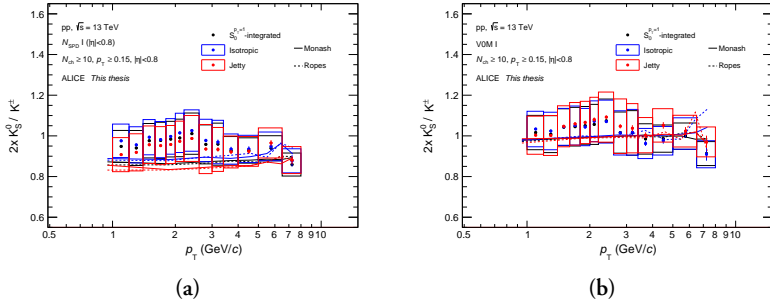


Figure 6.15: Ratios of transverse momentum spectra of K_S^0 to K^\pm in (a) $N_{\text{SPD}_{\text{Trkts}}}$ I and (b) V0M I high-multiplicity events, also showing the effect of spherocity selection. The results are compared with MC predictions of Pythia 8 tunes.

6.4 Mean transverse momenta and integrated yields

The $\langle p_T \rangle$ and particle yields (dN_{ch}/dy) in different $S_O^{(p_T=1.0)}$ bins for the $N_{\text{SPD}_{\text{Trkts}}}$ I class are reported in Fig. 6.16. The measured values of $\langle p_T \rangle$ quantify the observations in the spectra: there is a significant p_T -hardening in jet-like events, consistently seen in both K_S^0 and Λ . Furthermore, the $\langle p_T \rangle$ of the inclusive high-multiplicity events is consistent with that of the isotropic subsample. This result suggests that the average high-multiplicity events and $S_O^{(p_T=1.0)}$ -selected isotropic events are dominated by similar underlying physics processes.

Furthermore, the $S_O^{(p_T=1.0)}$ -integrated event class is not simply the arithmetic average of the jetty and isotropic subsamples. This implies that jetty events are rare outliers of a much more homogeneous group of high-multiplicity events, which will be further focused on in the next sections.

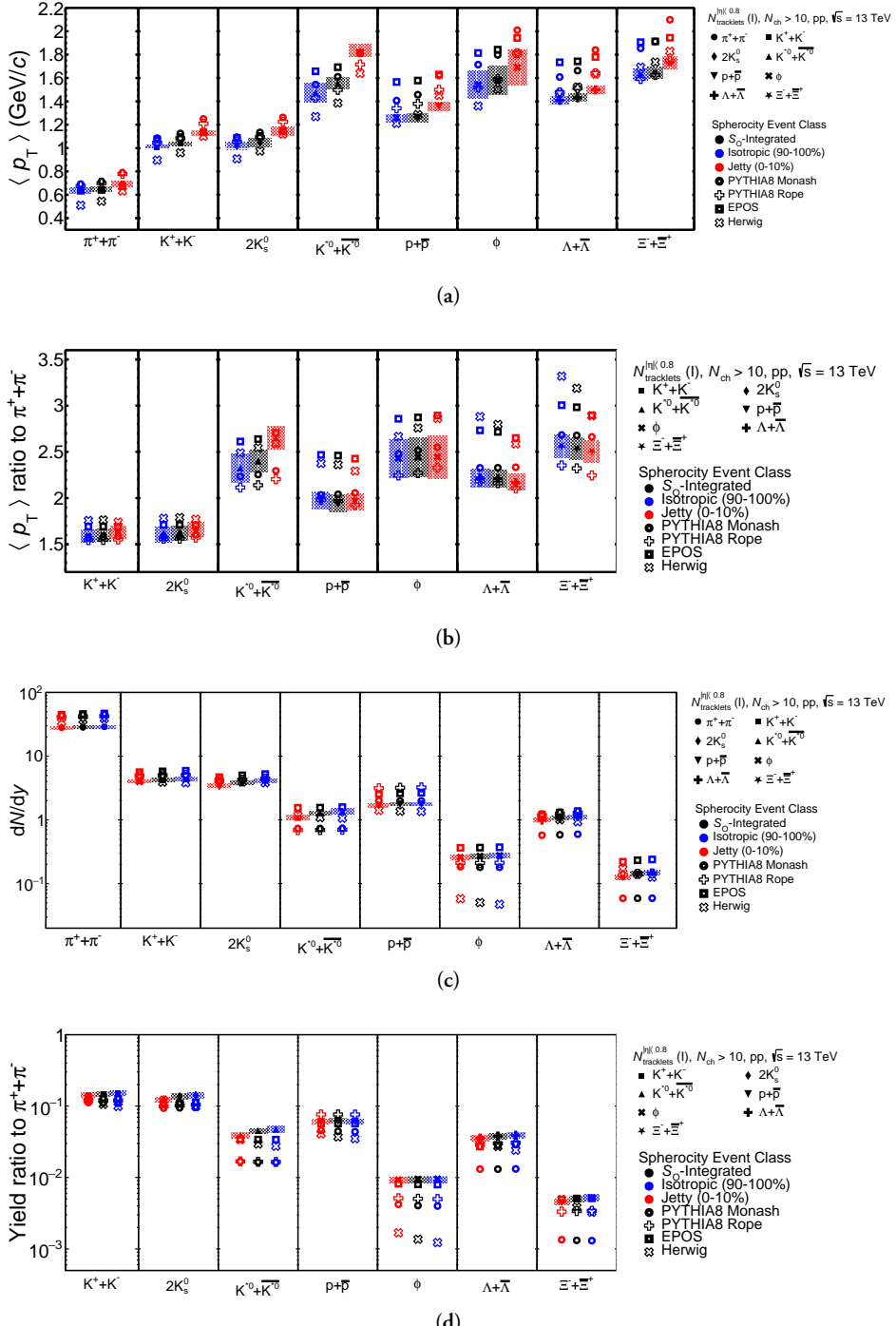


Figure 6.16: (a) Mean transverse momentum and (c) integrated yields of $\pi^+ + \pi^-$, K_S^0 , and $\Lambda + \bar{\Lambda}$ in jetty, isotropic, and $S_O^{(p_T=1.0)}$ -unbiased high-multiplicity events determined at mid-rapidity. (b,d) Their ratios of K_S^0 and $\Lambda + \bar{\Lambda}$ to pions. CROP TO SHOW ONLY pi, K_S^0 , Λ .

The results indicate that not only charged pions but also neutral K_S^0 and Λ show little variation in multiplicity between the different $S_O^{(p_T=1.0)}$ extremes in the $N_{\text{SPD}_{\text{Trkts}}}$ I class, although more so for the latter two. This could be because of their smaller correlation with $S_O^{(p_T=1.0)}$ as they are neutral, or it may suggest strangeness enhancement. The models generally provide good agreement with the measured $\langle p_T \rangle$ of K_S^0 , while the results for Λ are best described by the Pythia Ropes model. The yields for K_S^0 are also largely consistent with the models presented, whereas the Pythia Monash model does not match the Λ yields.

6.5 Ratios to pions

Rather than focusing on the models' inability to match the absolute values, this measurement can provide an opportunity to study the underlying dynamics that affect the heavier and stranger particles. To achieve this, the K_S^0 and $\Lambda + \bar{\Lambda}$ p_T spectra are divided by the $\pi^+ + \pi^-$ spectra. The results are presented in Fig. 6.17 and Fig. 6.18.

The data reveals overall suppression of K_S^0 in jetty events and enhancement in isotropic events in the measured p_T range. The effect is observed, although in different ways, in all three event classes: $N_{\text{SPD}_{\text{Trkts}}}$ I (where spherocity is assumed to change mostly the $\langle p_T \rangle$), $N_{\text{SPD}_{\text{Trkts}}}$ I-III (where spherocity is assumed to change both the $\langle p_T \rangle$ and multiplicity), and V0M I (where spherocity is assumed to change mostly the multiplicity). The Λ ratios behave similarly but an enhancement in low- p_T is observed in the V0M I case, resembling typical radial flow signatures.

The presented models cannot describe the ratios to pions, although the trends relative to the $S_O^{(p_T=1.0)}$ -unbiased case are reproduced well.

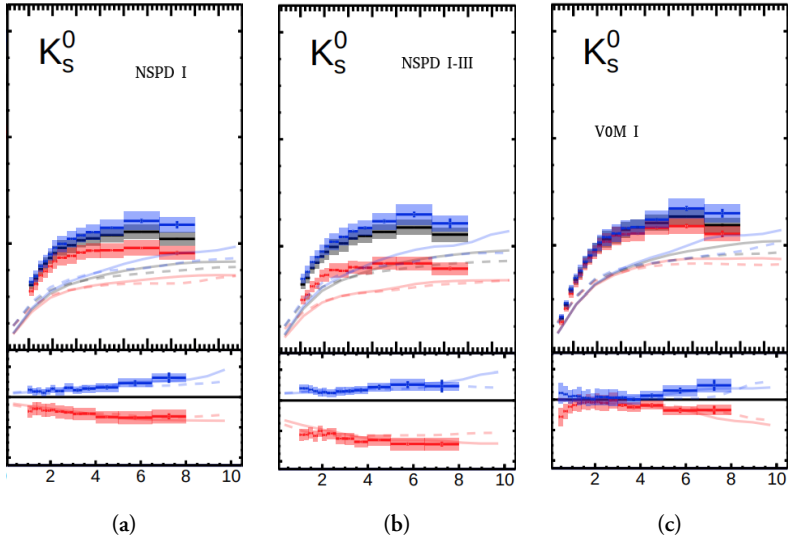


Figure 6.17: Ratios of transverse momentum spectra of K_S^0 to $\pi^+ + \pi^-$ in jetty, isotropic, and $S_0^{(p_T=1.0)}$ -unbiased in events with high-multiplicity classes (a) $N_{\text{SPD-Tkls}}$ I, (b) $N_{\text{SPD-Tkls}}$ I-III, and (c) V0M I. Statistical and systematic uncertainties are depicted as error bars and boxes, respectively.

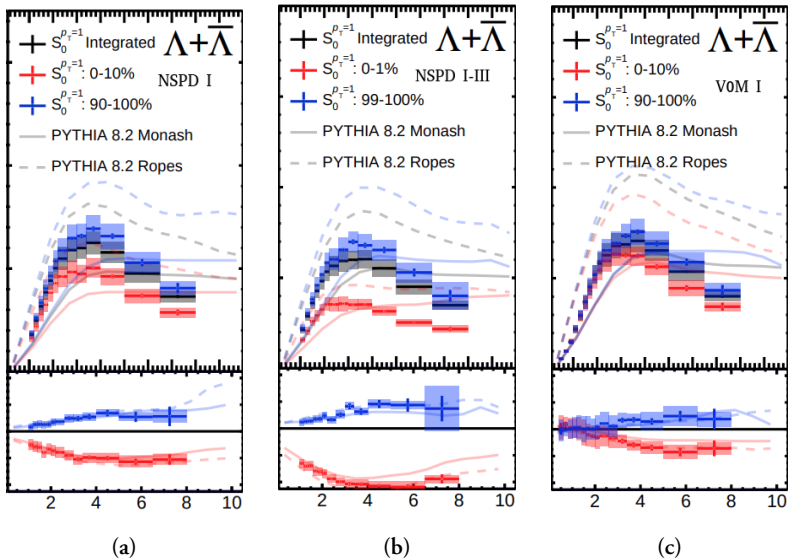


Figure 6.18: Ratios of transverse momentum spectra of $\Lambda + \bar{\Lambda}$ to $\pi^+ + \pi^-$ in jetty, isotropic, and $S_0^{(p_T=1.0)}$ -unbiased in events with high-multiplicity classes (a) $N_{\text{SPD-Tkls}}$ I, (b) $N_{\text{SPD-Tkls}}$ I-III, and (c) V0M I. Statistical and systematic uncertainties are depicted as error bars and boxes, respectively.

6.6 Baryon-to-meson ratio

The baryon-to-meson ratio $(\Lambda^0 + \bar{\Lambda}^0)/(2K_S^0)$ was investigated in this study, as it is a common observable used to measure the effects of radial flow, as discussed in Section X. To focus on the different functions of $S_O^{(p_T=1.0)}$ selection in the different high-multiplicity classes, the results for the $N_{SPD_{Trkls}}$ I and V0M I events are shown in Fig. 6.19. They are also juxtaposed with the p/π ratios [157]. The ratios reveal a significant increase when transitioning from jetty to isotropic events, indicating that the production of heavier Λ is systematically more suppressed in jetty events than K_S^0 . Similar observations have been made in other ALICE measurements studying jets (discussed further in ??) [158].

Although the increase in the ratio is consistent with the typical signatures of radial flow, the $N_{SPD_{Trkls}}$ I results do not reveal the depletion at low p_T and neither results show the shift of the peak to higher p_T , both of which are also its characteristic features. Additionally, the data are compared with the two tunes of Pythia 8, favouring the Ropes configuration.

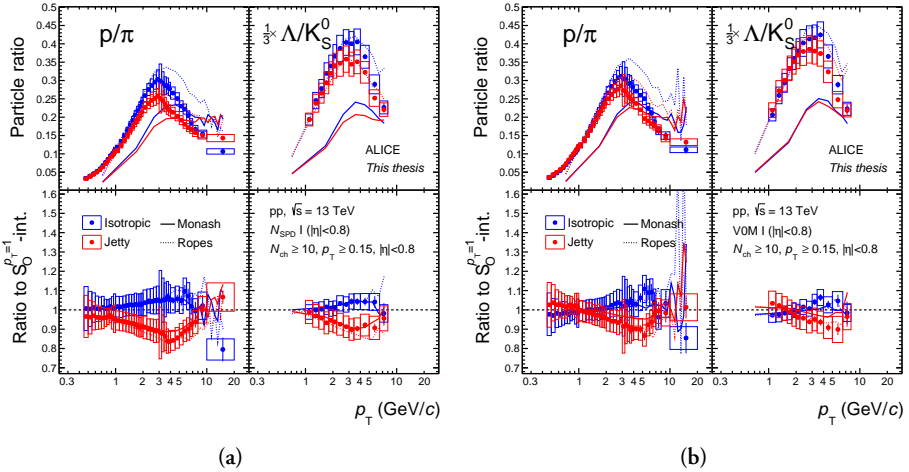


Figure 6.19: Baryon-to-meson ratios of the jetty (0 – 10%) and isotropic (90 – 100%) transverse momentum spectra of $p \rightarrow \pi$ and $\Lambda + \bar{\Lambda} \rightarrow K_S^0$ in the (a) $N_{SPD_{Trkls}}$ I and (b) V0M I high-multiplicity events of pp collisions at $\sqrt{s} = 13$ TeV. The bottom panels display the ratios to the $S_O^{(p_T=1.0)}$ -unbiased case. MC predictions are denoted by lines, statistical uncertainties as error bars, and systematic uncertainties as error boxes.

6.7 Ratio of integrated yields vs. $S_O^{(p_T=1.0)}$

The main contribution of this study is the investigation of strangeness production as a function of $S_O^{(p_T=1.0)}$. Yields of the Λ baryon were determined in $N_{\text{SPD}_{\text{Trkls}}}$ I and V0M I classes in the following intervals of $S_O^{(p_T=1.0)}$: 0–1%, 1–5%, 5–10%, 10–20%, 20–80%, 80–90%, 90–95%, 95–99%, and 99–100%. The integration was done in the measured p_T range rather than extrapolated. The $S_O^{(p_T=1.0)}$ -dependent Λ yields are then divided by $S_O^{(p_T=1.0)}$ -dependent pion yields as a reference. The effects of not extrapolating were studied and found to be unimportant, and while the extrapolation confirms the physics message of the default method, it also increases systematic uncertainties.

The results, together also with $p(|S| = 0)$ and $\Xi(|S| = 2)$ are reported in Fig. 6.20. For the $N_{\text{SPD}_{\text{Trkls}}}$ I events, there is a clear strangeness- and/or mass-dependent enhancement with increasing $S_O^{(p_T=1.0)}$. It is important to emphasize that in this event class, the N_{ch} multiplicity is basically fixed. Therefore, these effects are results of the different underlying dynamics of the collisions, specifically the varying hardness of involved scatterings, rather than merely an effect of increased N_{ch} .

Conversely, the V0M I events show no such dependence, and jetty and isotropic events appear to produce the same relative amount of strangeness. This goes against intuition that varying N_{ch} between jetty ($N_{\text{ch}} \rightarrow 15$) and isotropic events ($N_{\text{ch}} \rightarrow 30$, according to Fig. 6.7) should introduce an effect, in accordance with traditional studies of strangeness enhancement in pp collisions as a function of N_{ch} . This observation is not fully understood, but it suggests that the decrease in strangeness in jetty events due to the decrease in N_{ch} and increase in $\langle p_T \rangle$ is not trivial and counterbalanced by some other factors of the collision.

Finally, the results were compared with MC predictions, and only Pythia 8 Ropes accurately captures the observed trends and, to some extent, the magnitudes.

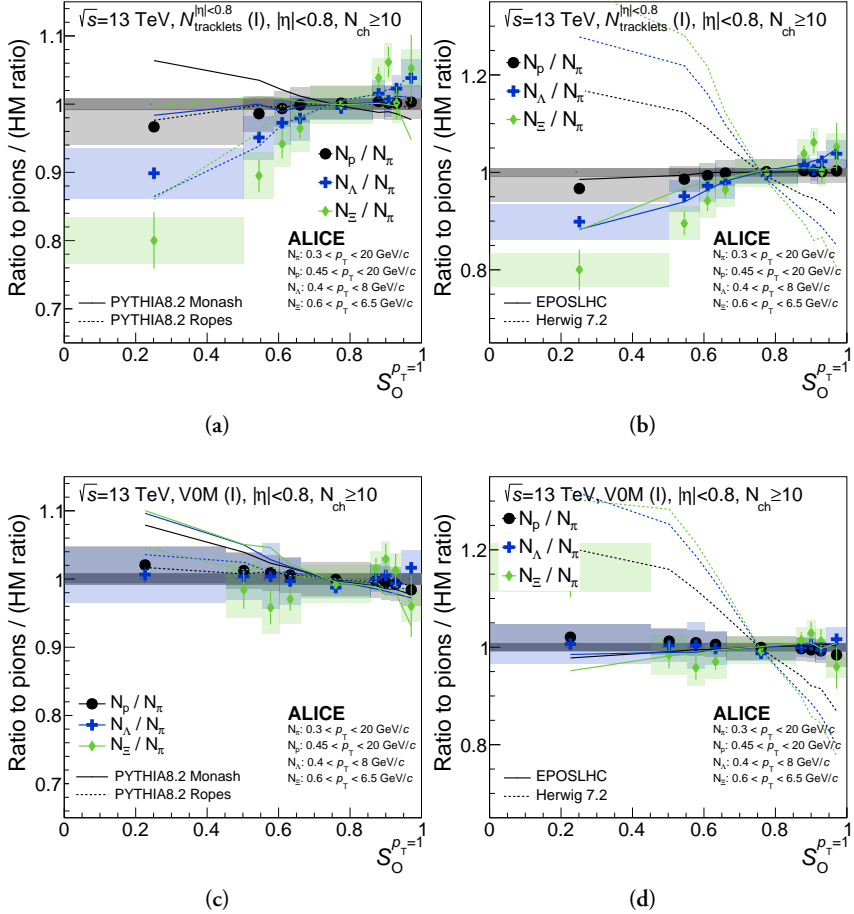


Figure 6.20: Double-ratios of integrated yields with respect to pions as a function of $S_O^{(p_T=1.0)}$ in the $N_{\text{SPD}_{\text{Trkts}}}^{\eta|<0.8}$ I and V0M I events. Statistical and total systematic uncertainties are shown by bars and boxes, respectively. The curves represent different model predictions of the same measurement: (a),(c) Pythia Monash and Ropes, (b),(d) EPOS LHC and Herwig.

Chapter 7

Underlying Event Activity

In this chapter, measurements of K_S^0 , Λ , and $\bar{\Lambda}$ are reported as a function of the underlying event activity classifiers R_T , $R_{T,\min}$, and $R_{T,\max}$. These observables quantify the magnitude of the underlying event and are an experimental proxy of the number of Multiple Partonic Interactions, n_{MPI} .

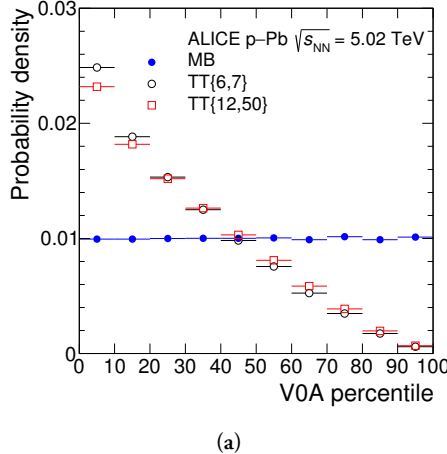
7.1 Motivation for studying event sub-structure

7.1.1 Underlying event

As discussed in Section 1.7, the underlying event is composed of particles that are not directly related to the primary hard scattering and its related fragmentation. It can be studied to extract accurate information about the hard scattering process by subtracting it in precision measurements of jet properties. Moreover, since it is a manifestation of the proton substructure and the parton interactions, it can give us insight into the parton dynamics in the nonperturbative QCD region.

7.1.2 Hard process–multiplicity bias

Studying QGP phenomena in small systems as a function of event activity is challenging due to selection biases that arise when analyzing the data. It is known that selecting events with large momentum transfer leads to a bias towards higher multiplicities (and underlying event) [106], and conversely, selecting events with higher multiplicities (and UE) enhances the hard processes [159]. This bias can be under-



(a)

Figure 7.1: Distribution of event activity measured at forward rapidity (V0A percentile) for minimum bias events (blue points) and for events requiring a high- p_T trigger in the intervals $6 < p_T < 7 \text{ GeV}/c$ (black points) and $12 < p_T < 50 \text{ GeV}/c$ (red points). Lower V0A percentile represent higher event activity. The MB distribution is trivially uniform by construction. [106]

stood in several ways. Firstly, a hard process tends to occur with lower impact parameters, which in turn leads to higher particle multiplicities. Secondly, an event with n partonic interactions has n chances of containing a hard process. Lastly, harder processes fragment into more particles, further contributing to higher event activity. As an example, Figure 7.1 shows how the requirement of a high p_T track can skew the forward-rapidity centrality distribution to lower values (higher event activity), as observed in a result from ALICE [106].

7.1.3 Azimuthal regions and transverse activity

The selection bias of hard processes on UE becomes saturated at high p_T , where the impact parameter bias is fixed and stochastic effects become comparable [?]. This saturation effect can be observed when studying particle production in three topological regions defined with respect to the highest momentum track, which serves as a proxy for the axis of the primary scattering process. The three regions are defined as follows:

1. Towards (also known as "Near"), where $|\phi - \phi^{\text{leading}}| < \frac{\pi}{3}$,
2. Away, where $|\phi - \phi^{\text{leading}}| > \frac{2\pi}{3}$, and
3. Transverse, where $\frac{\pi}{3} < |\phi - \phi^{\text{leading}}| < \frac{2\pi}{3}$.

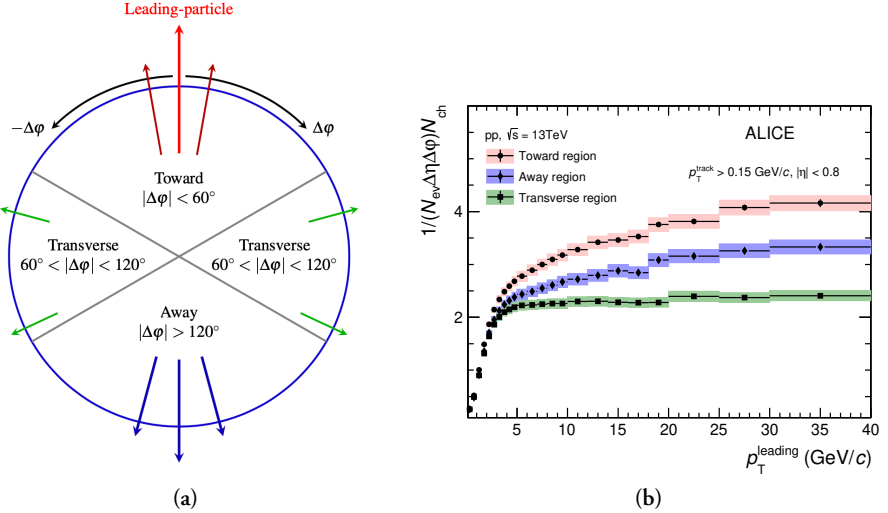


Figure 7.2: (a) Illustration of the three azimuthal regions: Toward, Away, Transverse; defined with respect to the highest- p_T track. [?] (b) Charged particle density distributions as a function of p_T of the leading track in the three azimuthal regions. Error bars indicate statistical uncertainties and shaded areas represent systematic uncertainties. [?]

Here, ϕ^{leading} is the azimuthal angle of the leading track. This definition is illustrated in Figure 7.2.

Studying particle multiplicity (or sum of their p_T) in these regions as a function of the transverse momentum of the leading track p_T^{leading} reveals that in the regions Towards and Away, the multiplicity continues to increase with the hardness of the primary process [160?]. These regions contain the leading and the recoil jet, respectively. In contrast, in the Transverse region, the multiplicity (further denoted as N_T in this thesis but N_{ch}^{trans} is also used in cited literature) reaches a plateau at around 5 GeV/c. In this region, the underlying event becomes independent of the strength of the primary process, and the selection bias is minimized. Notably, this phenomenon is universal regardless of the system size or collision energy [160, 161, 162?]. As an example, measurements from ALICE are shown in Fig. 7.2.

7.2 R_T as an experimental observable

The magnitude of the underlying event can be measured using the self-normalized ratio:

$$R_T = \frac{N_T}{\langle N_T \rangle}, \quad (7.1)$$

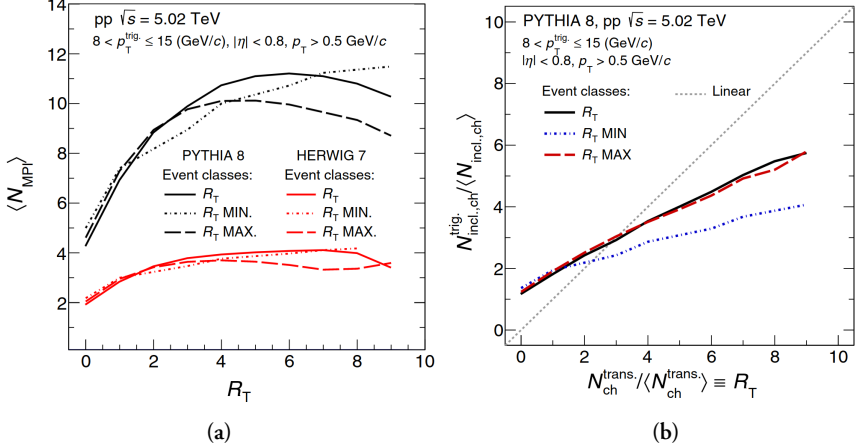


Figure 7.3: (a) Dependence of the mean number of MPIs on the underlying event activity classifiers R_T , $R_{T,\text{min}}$, and $R_{T,\text{max}}$ in pp collisions at $\sqrt{s} = 5.02 \text{ TeV}$, as predicted by Pythia 8 (black) and Herwig 7 (red). [166] (b) Pythia 8 prediction for the correlation of the self-normalised charged particle multiplicity measured at mid-rapidity in events with a high- p_T trigger and the underlying event activity classifiers R_T , $R_{T,\text{min}}$, $R_{T,\text{max}}$. [166]

which is often referred to as the underlying event activity, transverse activity, or relative transverse activity in various literature [163, 164, 165], and also in this thesis. This observable and its uses were suggested in Ref. [163].

By applying R_T , two limits of events can be studied:

- $R_T \rightarrow 0$: the “ee” limit, where events with minimal UE are selected. These events are dominated by a single hard scattering and can be compared to LEP fragmentation models.
- $R_T \rightarrow \infty$: the “AA” limit, where events with very high transverse activity are selected, which can come from many MPIs and/or from transverse jets. These events may exhibit features similar to pA and AA collisions.

7.2.1 Proxy to n_{MPI}

As could be intuitively expected, R_T serves as an experimental proxy for $\langle n_{\text{MPI}} \rangle$. Phenomenological models that incorporate MPIs provide an illustration of this relationship. As shown in Fig. 7.3, Pythia 8 predicts a strong dependence of $\langle n_{\text{MPI}} \rangle$ on R_T until $R_T \lesssim 5$. Similarly, Herwig 7 predicts a dependence until $R_T \lesssim 3$, albeit weaker. Pythia’s prediction for the relationship between R_T and the event multiplicity, which is affine, is also shown in Fig. 7.3.

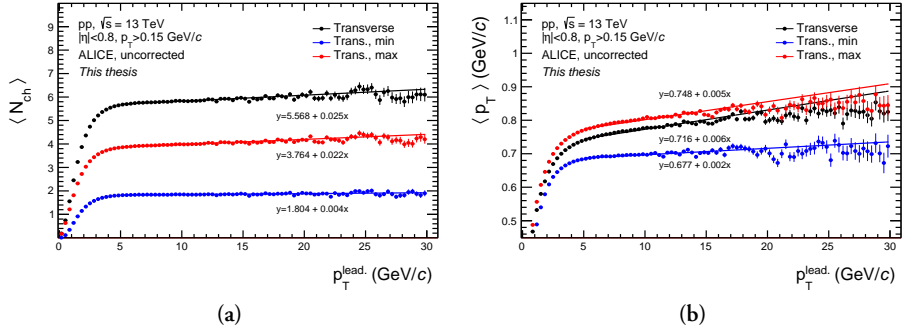


Figure 7.4: TBA

7.2.2 Extension to $R_{T,\text{min}}$, $R_{T,\text{max}}$

Upon closer inspection of Fig. 7.2, it can be observed that the charged particle multiplicity does not completely plateau in the Transverse region either, which was an important factor in motivating R_T measurements. Instead, there is a slight increase with p_T^{leading} , although the effect is small. This rise can be attributed to harder, wide-angle ISR and FSR [167].

To separate the soft and hard components of the underlying event – namely, the MPIs from wide-angle ISR/FSR – the definition of R_T can be extended. The two transverse sub-regions can be further classified as Transverse-min or Transverse-max, based on which sub-region has fewer or more particles. Softer contributions from MPIs will enter both sub-regions, whereas harder radiation should affect mainly the Transverse-max sub-region. This makes Transverse-min more sensitive to particle production from MPIs. Figure 7.4 illustrates how the Transverse-max region captures most of the rise of $\langle N_{ch} \rangle$ and $\langle p_T \rangle$, whereas the Transverse-min region is much closer to plateauing.

Analogously, the following underlying event activity classifiers can be defined:

$$R_{T,\text{min}} = \frac{N_{T,\text{min}}}{\langle N_{T,\text{min}} \rangle} , \quad (7.2)$$

$$R_{T,\text{max}} = \frac{N_{T,\text{max}}}{\langle N_{T,\text{max}} \rangle} , \quad (7.3)$$

where $N_{T,\text{min}}$ and $N_{T,\text{max}}$ are the particle multiplicities in the Transverse-min and Transverse-max sub-regions, respectively. This approach follows measurements developed at UE studies at Tevatron [167] and has been suggested to use in searches for QGP phenomena in small systems based on investigations in phenomenological

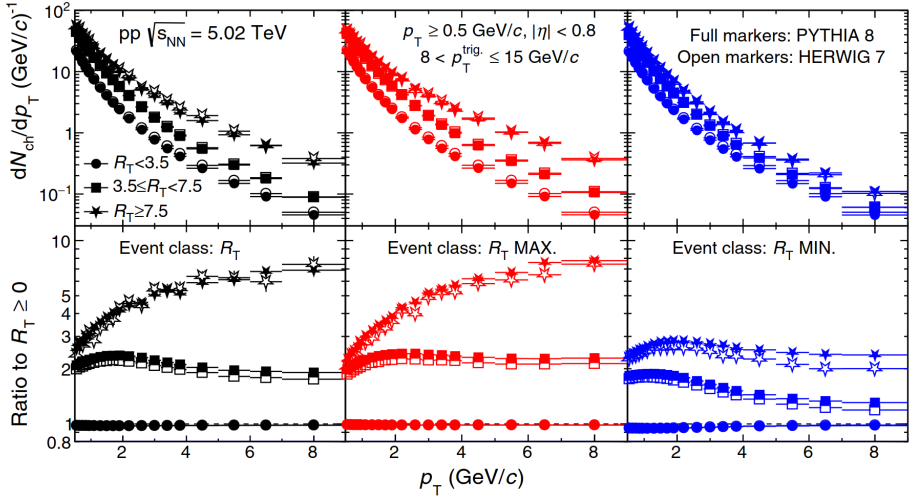


Figure 7.5: Transverse momentum spectra of charged particles produced in three azimuthal regions: (**left**) Transverse, (**middle**) Transverse-max, (**right**) Transverse-min, as a function of the underlying activity $R_{\text{T}}/R_{\text{T},\text{max}}/R_{\text{T},\text{min}}$ in pp collisions at $\sqrt{s} = 5.02 \text{ TeV}$. The bottom row displays the ratios to the UE-activity integrated cases. The predictions are based on Pythia 8 and Herwig 7 simulations. [166]

models [166]. In the rather rare situations with $N_{\text{T},\text{min}} = N_{\text{T},\text{max}}$, the classification is based on the sum of p_{T} instead.

According to Pythia 8, as shown in Fig. 7.3, $R_{\text{T},\text{min}}$ and $R_{\text{T},\text{max}}$ follow different relationships with $\langle n_{\text{MPI}} \rangle$. Whereas $\langle n_{\text{MPI}} \rangle$ starts falling as a function of $R_{\text{T},\text{max}}$ (due to the inclusion of mini-jets) at $R_{\text{T},\text{max}} \approx 5$, it continues rising as a function of $R_{\text{T},\text{min}}$ across the entire range. Furthermore, compared to R_{T} , $R_{\text{T},\text{min}}$ also shows some degree of decorrelation with event multiplicity.

Charged particle p_{T} spectra

Phenomenological models also reveal a different evolution of transverse momentum spectra of inclusive charged particles based on $R_{\text{T},\text{min}}$ and $R_{\text{T},\text{max}}$, as shown in Fig. 7.5. For the highest reported ranges of $R_{\text{T},\text{max}}$ and R_{T} , a significant hardening of the spectrum is observed in both Pythia 8 and Herwig 7, similarly to multiplicity studies [146], indicating a strong auto-correlation. In contrast, $R_{\text{T},\text{min}}$ exhibits a Cronin-like enhancement¹ at intermediate p_{T} and a plateau at $p_{\text{T}} \gtrsim 6 \text{ GeV}/c$, even in the highest $R_{\text{T},\text{min}}$ bin [166]. So far, this behaviour has not been observed in data.

¹Cronin effect refers to the modification of p_{T} spectra in nuclear collisions as a result of partonic scattering in the nuclear medium and can be observed as a characteristic peak in nuclear modification factors at intermediate p_{T} [168].

7.2.3 Track and event selection

The event selection follows the same criteria as the $S_O^{(p_T=1.0)}$ measurement discussed in Section 6.1.4, which conform to the standard analysis of light flavour hadrons versus multiplicity in pp collisions conducted in ALICE. The INEL > 0 events, which require at least one hit in either V0A or V0C scintillators and a track reconstructed within $|\eta| < 1$, are used. The SPD is used for the reconstruction of the primary vertex, which is further required to be close to the nominal vertex ($|\Delta z| < 10$ cm) to reject out-of-bunch pile-up. To remove in-bunch pile-up, events with multiple reconstructed vertices are excluded.

Events are required to have a leading track with reconstructed momentum $5 < p_T^{\text{leading}} < 40 \text{ GeV}/c^2$. These values were chosen to access the plateau in transverse activity and isolate the UE while retaining a large data sample. Maintaining a high momentum and spatial resolution of the leading track is crucial in this measurement. However, this can be compromised at high p_T when a significant portion of the track curvature can fall between two sectors of the TPC. To address this issue, geometrical cuts are used, as discussed in Section ??.

For both the leading particle as well as the particles entering N_T and R_T calculations, tracks are required to be within $|\eta| < 0.8$ and have $p_T > 0.15 \text{ GeV}/c$, and must satisfy the following:

1. “Hybrid tracks”, described in more detail in Section ??, are used for both leading and N_T tracks to ensure a high level of azimuthal acceptance uniformity. These tracks consist of high-quality “global track” requirements, including the SPD information, which leads to azimuthal non-uniformity, and “complementary track” cuts, a looser set requiring only ITS and TPC in cases where the first are not satisfied.
2. For the leading track, strict p_T -dependent DCA cuts are applied in the transverse direction ($|\text{DCA}_{xy}| < 0.0182 + \frac{0.0350}{p_T^{1.01}} \text{ cm}$, $p_T \in [\text{GeV}/c]$), to ensure good momentum resolution and that the track is a primary one.
3. For the N_T tracks, a DCA cut ($|\text{DCA}_{xy}| < 0.06 \text{ cm}$) is required to avoid biases in V^0 measurements, as explained in the text below.

²Note that p_T spectrum is falling very steeply, at an approximately exponential rate, making the upper bound negligibly restrictive compared to the lower bound.

7.2.4 R_T measurements of neutral particles vs. charged particles

The V^0 s are neutral particles and thus, they cannot be leading tracks nor enter N_T ($N_{T,\min}$, $N_{T,\max}$) and R_T ($R_{T,\min}$, $R_{T,\max}$) calculations. This has several implications:

1. V^0 s suffer much less from auto-correlation biases than $\pi/K/p$, which can be seen in azimuthal distributions and in K_S^0/K^\pm ratios. Requiring high/low N_T/R_T can lead to an increase/decrease of charged particles in the Transverse region due to selecting fluctuations in addition to the UE scaling. However, this effect is significantly smaller for neutral V^0 s. This behaviour is shown in Fig. 7.6. It is important to bear this caveat in mind when comparing p_T spectra and yields of $\pi/K/p$ and V^0 s.
2. While N_T is always at least 1 for $\pi/K/p$ in the Transverse region, for V^0 s it can be equal to 0. Similar logic applies to the Transverse-min/max sub-regions and $N_{T,\min}/N_{T,\max}$.
3. The maximum p_T measurable for $\pi/K/p$ in the Toward region is limited to $p_T < 5 \text{ GeV}/c$, at which point the trigger requirement would lead to a trivial increase. For V^0 s, however, this limitation does not apply and their measured p_T range does not need to be restricted.
4. The charged daughters of V^0 s could sometimes enter N_T , leading to significant biases at low p_T in the Toward and Away regions of K_S^0/K^\pm ratios.

In this thesis, the behaviour described in the last point was rectified by making N_T track candidates and V^0 daughter tracks two disjunct sets. This was achieved by applying the $|DCA_{xy}| > 0.06 \text{ cm}$ cut, used in the V^0 reconstruction as discussed in Section 5.2, in opposite ways. This reduces the N_T track candidates by less than 5%. The effect of this solution can be seen in Fig. 7.7.

7.3 Bayesian unfolding procedure

The measurements of V^0 s are conducted as a function of the number of measured tracks N_T^m within the detector acceptance. The measured multiplicity N_T^m includes a fraction of the true primary charged-particle multiplicity N_T^t not lost due to acceptance, efficiency, or track selection, as well as contributions from secondary particles or particles smeared into the measurement's kinematic acceptance due to detector resolution (i.e., from $p_T < 0.15 \text{ GeV}/c$). These effects fluctuate on an event-by-event

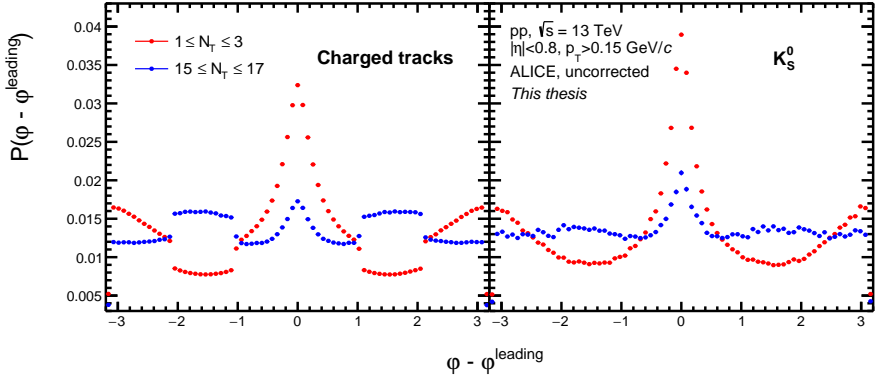


Figure 7.6: Probability distributions of the azimuthal angle of (left) charged tracks and (right) the neutral K_S^0 . Events with low N_T (red) and high N_T (blue) are compared. The results are uncorrected for reconstruction effects and acceptance and show only statistical uncertainties.

basis and thus there is no unique correlation between N_T^m and N_T^t . This means that events with true multiplicity N_T^t can be measured with different N_T^m , contributing to V^0 measurements in multiple N_T^m bins. Therefore, each spectrum contains particles from events with many true multiplicities N_T^t .

This thesis uses a Bayesian unfolding procedure, as discussed in Ref. [169], to convert V^0 's measurements as a function of N_T^m into measurements as a function of N_T^t and thus correct for the mentioned effects.

7.3.1 One-dimensional unfolding

The measured multiplicity distribution $n_{\text{ev}}(N_T^m)$ can be mathematically represented as the result of convolving (or “folding”) the true multiplicity distribution produced by the collisions, $n_{\text{ev}}(N_T^t)$, with the detector’s response function. The response matrix S_{mt} , which represents the conditional probability $P(N_T^m | N_T^t)$ of an event with multiplicity N_T^t being measured with multiplicity N_T^m , can be obtained from MC simulations of the apparatus. Using this matrix, also shown in Fig. 7.8, $n_{\text{ev}}(N_T^m)$ can be expressed in terms of $n_{\text{ev}}(N_T^t)$ as follows:

$$n_{\text{ev}}(N_T^m) = \sum_t S_{mt} \cdot n_{\text{ev}}(N_T^t) \quad , \quad (7.4)$$

To obtain the true multiplicity distribution from the measured distribution, the inverse of S_{mt} could be used, hypothetically, as shown below:

$$n_{\text{ev}}(N_T^t) = \sum_m S_{mt}^{-1} \cdot n_{\text{ev}}(N_T^m) \quad . \quad (7.5)$$

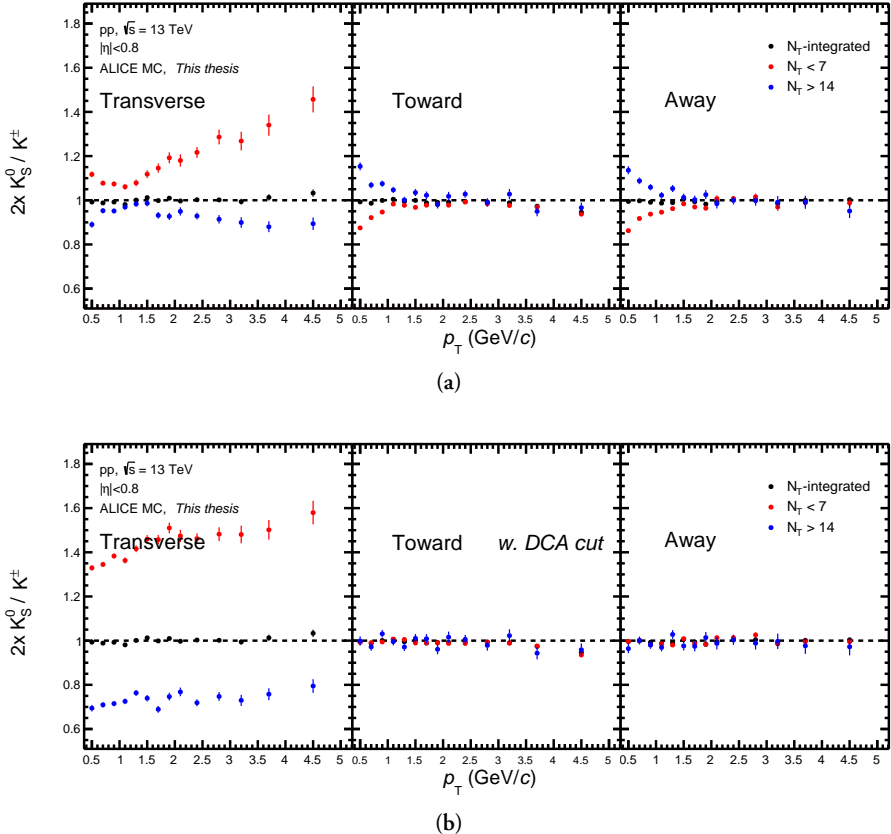


Figure 7.7: Transverse momentum spectra ratios of the neutral K_S^0 to the charged K^\pm without enforcing the DCA cut (top) and after its inclusion (bottom) in the three azimuthal regions. Events with low N_T (red) and high N_T (blue) are compared. The results come from ALICE detector simulations, are uncorrected for reconstruction effects and acceptance, and show only statistical uncertainties.

However, the inverse S_{mt}^{-1} may have multiple or zero solutions, making this approach unfeasible. Alternatively, S_{mt}^{-1} could be obtained directly from MC simulations, just like the detector response. However, this matrix would then strongly depend on the generated N_T^t distribution and be significantly model-dependent, as physics generators vary in their N_T^t predictions. In contrast, the detector response is mostly affected by the accuracy of the particle propagation simulations, which is a lot better understood. Therefore, an iterative numerical procedure based on Bayes' theorem is used to obtain the unfolding matrix M_{mt} , which represents the conditional probabilities $P(N_T^t | N_T^m)$ [169].

In this application, Bayes' theorem can be expressed in terms of N_T^m and N_T^t as fol-

lows,

$$P(N_T^t | N_T^m) = \frac{P(N_T^m | N_T^t) P(N_T^t)}{P(N_T^m)} , \quad (7.6)$$

where $P(N_T^t)$ and $P(N_T^m)$ are probability distributions for an event occurrence with N_T^t and N_T^m , respectively. Assuming that $P(N_T^t)$ is known, $P(N_T^m)$ can be calculated as follows:

$$P(N_T^m) = \sum_t P(N_T^m | N_T^t) P(N_T^t) . \quad (7.7)$$

Therefore, using Eq. 7.6, the conditional probability in the unfolding matrix can be written as follows:

$$P(N_T^t | N_T^m) = \frac{P(N_T^m | N_T^t) P(N_T^t)}{\sum_{t'} P(N_T^m | N_T^{t'}) P(N_T^{t'})} . \quad (7.8)$$

However, $P(N_T^t)$ (the “prior”) is initially unknown and must be arbitrarily chosen. The unfolding matrix can be calculated using this prior, and the unfolded distribution can be obtained as follows:

$$\hat{n}_{\text{ev}}(N_T^t) = \sum_m P(N_T^t | N_T^m) n_{\text{ev}}(N_T^m) . \quad (7.9)$$

This unfolded multiplicity can subsequently be used to update the prior as follows:

$$\hat{P}(N_T^t) = \frac{\hat{n}_{\text{ev}}(N_T^t)}{\sum_{t'} \hat{n}_{\text{ev}}(N_T^{t'})} , \quad (7.10)$$

starting a new iteration. The updated $\hat{P}(N_T^t)$ is closer to the true $P(N_T^t)$ than the initial guess because the arbitrarily chosen prior is constrained by the $n_{\text{ev}}(N_T^m)$ observable, which contains information about $P(N_T^t)$. The statistical uncertainties are propagated according to the discussion in Ref. [169].

Multiple approaches can be taken to choose the prior: a uniform distribution, the N_T^t distribution generated by a model, or the N_T^m distribution acquired from data. In this thesis, the prior choice was found to not play a role and the N_T^m distribution was used.

The χ^2/ndf is calculated to determine the validity of the correction and the stopping point for the iterative process. It is calculated by comparing the N_T^t distribution – known a priori in the simulations – and the unfolded $\hat{n}_{\text{ev}}(N_T^t)$ distribution, where ndf refers to the number of degrees of freedom, in this case the number of data points

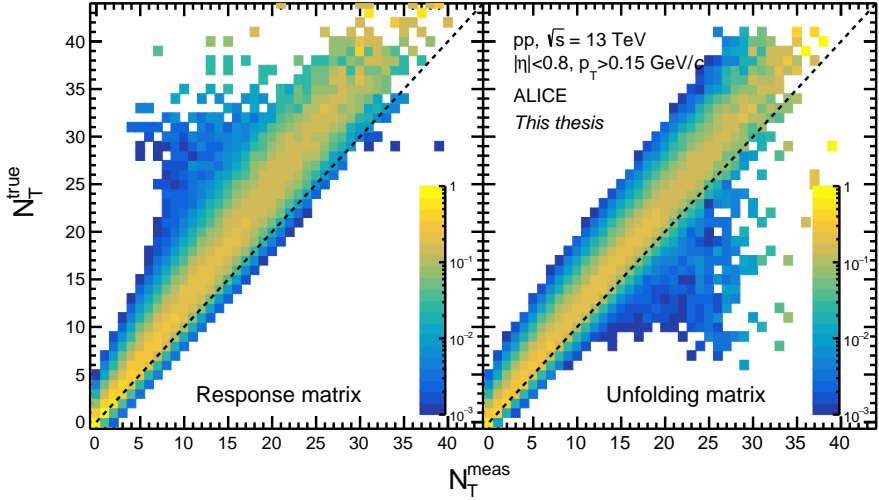


Figure 7.8: (left) Response matrix S_{mt} showing the correlation between measured and true track multiplicity in the Transverse region determined from ALICE MC simulations based on Pythia 8. The matrix is row-wise normalised. (right) Unfolding matrix $P(N_T^t | N_T^m)$ calculated from the iterative Bayesian unfolding procedure.

in the distribution. The process is stopped when χ^2/ndf reaches a minimum value or the iterations take a maximum number of steps n_{iter} . This is imposed to avoid overfitting and overestimation of statistical uncertainties.

In this dissertation, the $N_{T,\text{min}}$ and $N_{T,\text{max}}$ distributions are unfolded analogously to the N_T case. The selected n_{iter} values are reported in Tab. 7.1. The entire iterative process is summarised in a diagram shown in Fig. 7.9.

The used response matrix, as well as the resulting unfolding matrix, can be seen in Fig. 7.8. The method still exhibits some degree of model dependence due to the generation of the response matrix. Previous studies in ALICE have compared the response matrix for N_T acquired from Pythia 8 and from EPOS LHC MC simulations, which revealed that the effect is less than 1% [157]. This effect is taken into consideration as a source of systematic uncertainty.

Table 7.1: The number of iterations in the Bayesian unfolding process for N_T (capped at maximum n_{iter}), $N_{T,\text{min}}$, and $N_{T,\text{max}}$.

Unfolding observable	N_T	$N_{T,\text{min}}$	$N_{T,\text{max}}$
n_{iter}	20 (max.)	10	18

Bayes' Theorem

$$P(N_T^t | N_T^m) = \frac{P(N_T^m | N_T^t) P(N_T^t)}{P(N_T^m)}$$

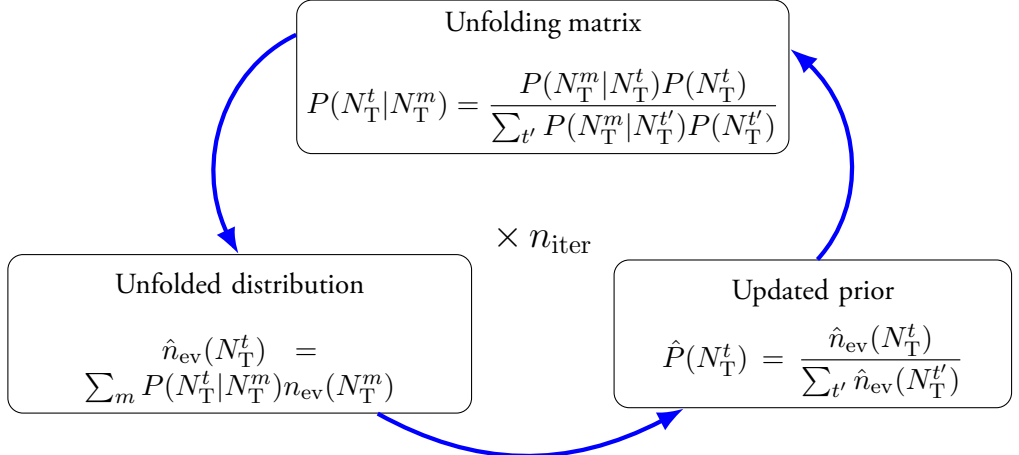


Figure 7.9: Diagram showing the iterative process of Bayesian unfolding.

7.3.2 Unfolding of K_S^0 , Λ , and $\bar{\Lambda}$ p_T spectra

In the unfolding treatment of the Λ and $\bar{\Lambda}$, the particle and the anti-particle p_T spectra were combined to reduce statistical uncertainties and increase the method's robustness. For the Toward and Away regions, the spectra can be unfolded in a similar fashion to the N_T activity, assuming that they are completely decoupled from the production in the Transverse region. This implies mere reshuffling of V^0 's in individual p_T bins $n_{p_T=i}^{V^0}$ between different events, based on the unfolding recipe established above:

$$\hat{n}_{p_T=i}^{V^0}(N_T^t) = \sum_m P(N_T^t | N_T^m) n_{p_T=i}^{V^0}(N_T^m) . \quad (7.11)$$

Closure tests using MC simulations were conducted to compare the unfolded p_T spectra as a function of unfolded-reconstructed N_T to the generated p_T spectra as a function of generated N_T – and showed the plausibility of this approach. The closure tests are presented in Fig. 7.10, indicating mostly consistent results within 5%, with the deviations observed more in the R_T extremes.

For the treatment of the Transverse regions, two approaches were considered:

1. Similarly to how this unfolding method was applied in other multiplicity and N_T measurements in ALICE for charged particles [157], one assumes correlations between the p_T spectra and the event activity. This approach requires multiplying the response matrix with number of tracks in each column, modifying the unfolding matrix to make it p_T -dependent, and applying different unfolding recipes to V^0 s based on their p_T , which approximates reshuffling on a particle-by-particle basis.
2. Given the fact that the N_T tracks and the V^0 daughters were made two disjunct sets in this measurement by separating them with a $|DCA_{xy}|$ boundary, one may assume complete de-correlation between the V^0 p_T spectra and the measured N_T . Subsequently, the Transverse region would be treated like the Toward and Away.

In this study, both approaches were tested and the second method was chosen for the measurement. Although the first method generally produced somewhat smaller non-closure discrepancies, the second method is more logically sound. Additionally, modifying the response matrix in the first method resulted in an empty zeroth bin by construction. As a consequence, events with $N_T = 0$ but the number of V^0 s $n^{V^0} > 0$ could not be treated since the unfolding matrix cannot recover this scenario. While this is not a limitation in charged particle analyses since such cases cannot occur, it posed a problem here.

The closure tests for the Transverse region are shown in Fig. 7.10, but it should be noted that they exhibit somewhat larger deviations (up to 10%) in the most extreme bins of R_T compared to the Toward/Away regions. One possible explanation for this is the simplicity of the unfolding method used here, as well as the fact that the closure tests were conducted on Pythia simulations, which due to the local string breakings may exhibit strongly correlated particle production in phase space, leading to somewhat of a coupling between N_T and V^0 s.

Unfolding of the V^0 s spectra in the Transverse-min and Transverse-max regions as a function of $N_{T,\min}$ and $N_{T,\max}$, respectively, was performed in an identical manner. Although the results close well in MC tests in the central $R_{T,\min}/R_{T,\max}$ intervals, deviations of up to around 20% are observed in the most extreme bins, as depicted in Fig. 7.10. This is likely due to low statistics samples, the simplicity of the method, and the fact that the individual $R_{T,\min}/R_{T,\max}$ intervals cover even smaller ranges of $N_{T,\min}/N_{T,\max}$, making the process highly sensitive to fluctuations.

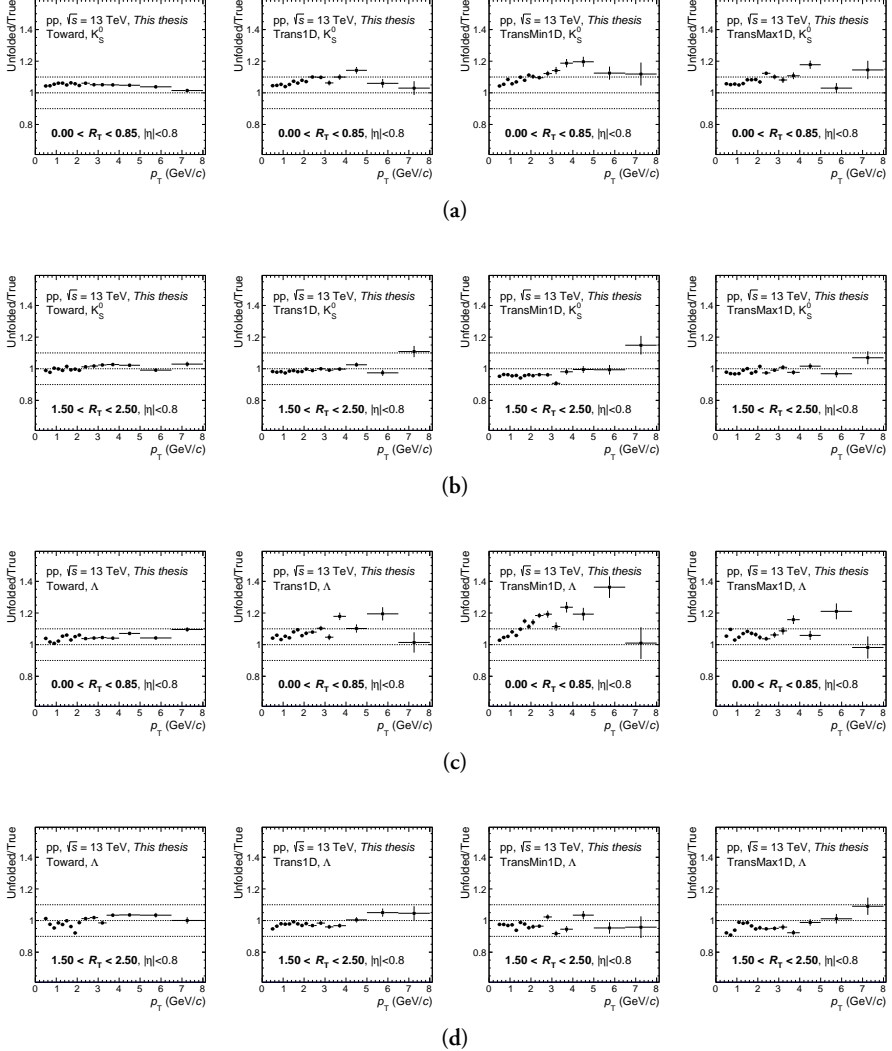


Figure 7.10: Transverse momentum Monte Carlo closure tests between true spectra and reconstructed, corrected, and unfolded spectra for (a) K_S^0 low- $R_T/R_{T,\min}/R_{T,\max}$ events, (b) K_S^0 high- $R_T/R_{T,\min}/R_{T,\max}$ events, (c) $\Lambda + \bar{\Lambda}$ low- $R_T/R_{T,\min}/R_{T,\max}$ events, and (d) $\Lambda + \bar{\Lambda}$ high- $R_T/R_{T,\min}/R_{T,\max}$ events. The columns show the regions in this order: Toward, Transverse, Transverse-min, and Transverse-max. A 10%-effect band is indicated.

7.4 $R_T, R_{T,\min}, R_{T,\max}$ distributions

The unfolded N_T , $N_{T,\min}$, and $N_{T,\max}$ distributions were self-normalised to obtain the R_T , $R_{T,\min}$, and $R_{T,\max}$ distributions, respectively. The mean values used for self-normalisation are reported in Tab. 7.2. They are shown in Fig. 7.11 and compared

with predictions from Pythia 8 (Monash tune [110] and Ropes tune [116]) as well as EPOS LHC [120].

Table 7.2: Mean number of transverse multiplicities used in the definition of R_T , $R_{T,\min}$, and $R_{T,\max}$.

Event classifier	R_T	$R_{T,\min}$	$R_{T,\max}$
Average $N_T/N_{T,\min}/N_{T,\max}$	7.345	2.470	4.869

The results can be described by the predictions quite accurately, favouring EPOS LHC, but show deviations in high-UE-activity events. The different quantiles corresponding to the $R_T/R_{T,\min}/R_{T,\max}$ ranges used in this measurement are highlighted. They are also summarised in Tab. 7.3. It should be noted that since the transverse multiplicities are non-negative integers, $N_T, N_{T,\min}, N_{T,\max} \in \mathbb{N}_0$, the $R_T/R_{T,\min}/R_{T,\max}$ distributions are not continuous observables.

Table 7.3: The intervals for UE activity classifier selected in this measurement and the corresponding average values.

Average values	$\langle R_T \rangle$	$\langle R_{T,\min} \rangle$	$\langle R_{T,\max} \rangle$
Intervals			
0–0.85	0.49	0.42	0.53
0.85–1.5	1.19	1.21	1.20
1.5–2.5	1.92	1.90	1.91
2.5–5.0	2.97	3.27	3.01

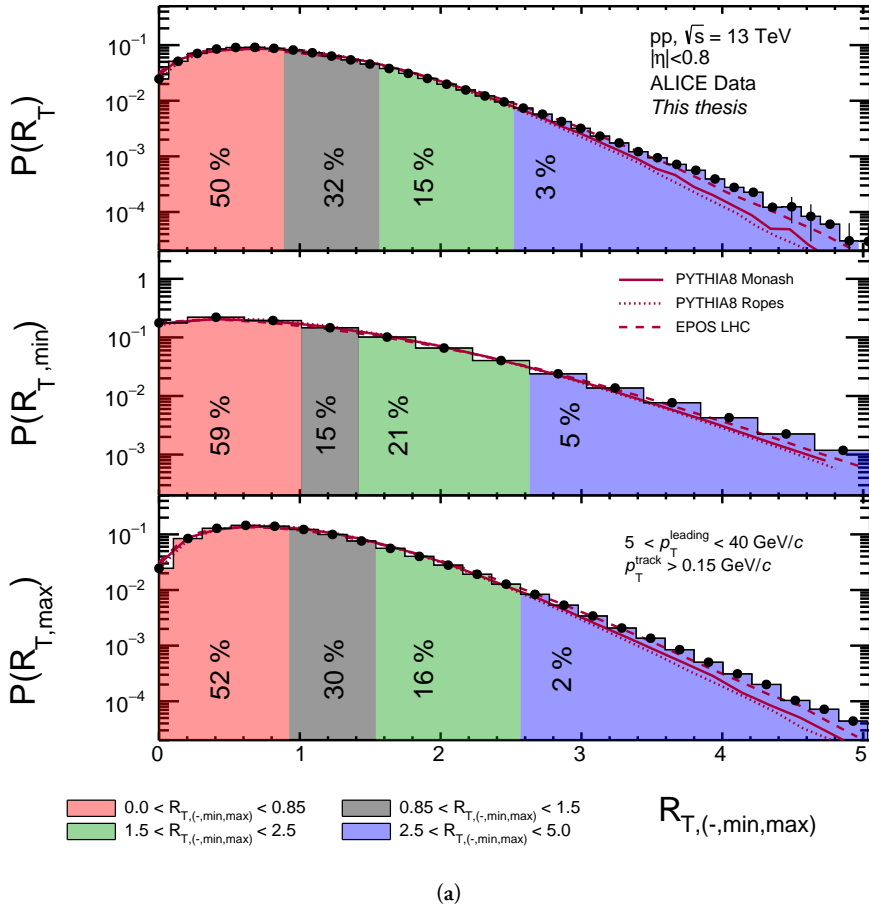


Figure 7.11: Probability distribution function of the underlying event activity classifiers R_T (top), $R_{T,\min}$ (middle), and $R_{T,\max}$ (bottom) in pp collisions at $\sqrt{s} = 13\text{ TeV}$ in events with a high- p_T track $5 < p_T < 40\text{ GeV}/c$. The results are treated with Bayesian unfolding and compared with predictions from Pythia 8 Monash, Pythia 8 Ropes, and EPOS LHC. The $R_T/R_{T,\min}/R_{T,\max}$ intervals used in this dissertation are shown along with the corresponding quantile values. Only statistical uncertainties are shown.

7.5 Systematic uncertainties

The systematic uncertainties on the p_T spectra were determined individually for each R_T interval and azimuthal region, following the procedures described in Section ???. They are reported in Fig. 7.12, Fig. 7.13, and Fig. 7.14 for the K_S^0 , Λ , and $\bar{\Lambda}$, respectively. Furthermore, they are summarised in Tab. ???. The dominant contributions to systematic uncertainties, in no specific order, come from signal extraction, selection cuts related to TPC tracking and topological reconstruction, and the requirement of signals from fast detectors to reject track pile-up.

As there are no reasons to believe the systematic uncertainties should differ when using the more specific UE activity classifiers in the two Transverse sub-regions, they are subsequently also applied in the $R_{T,\min}$ and $R_{T,\max}$ measurements.

Make the style consistent with the spherocity chapter.

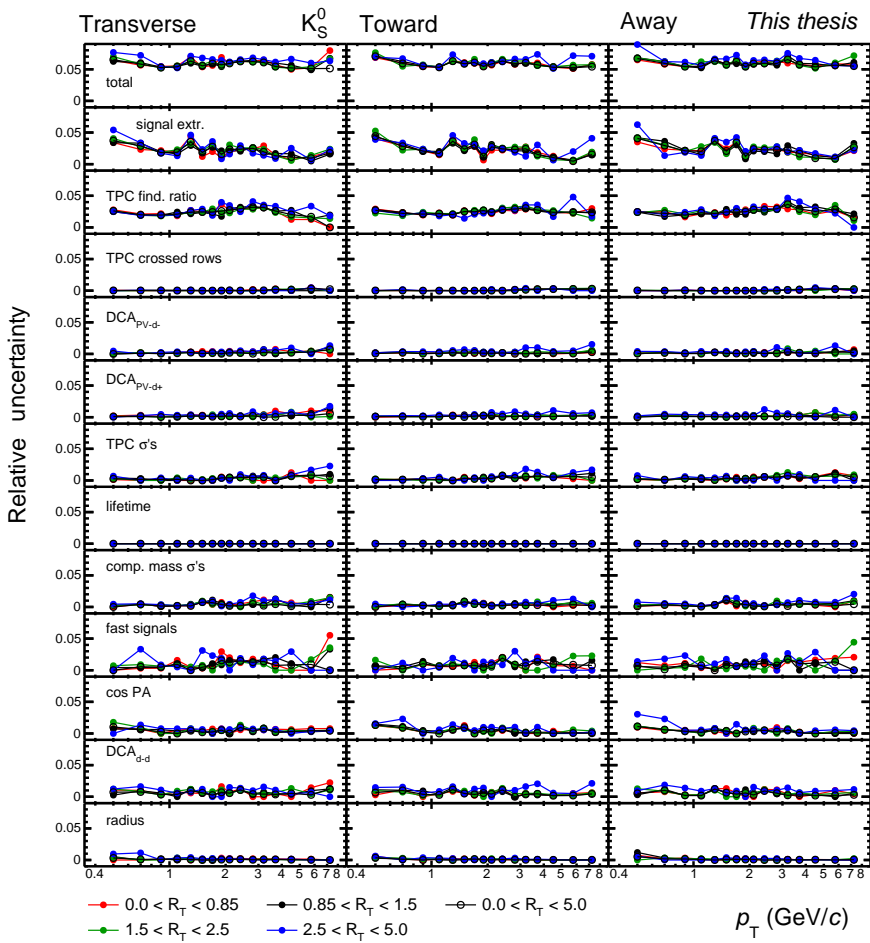


Figure 7.12: Summary of the relative systematic uncertainties on transverse momentum spectra and the individual contributions for K_S^0 in the (left) Transverse, (middle) Toward, and (right) Away in the different R_T intervals.

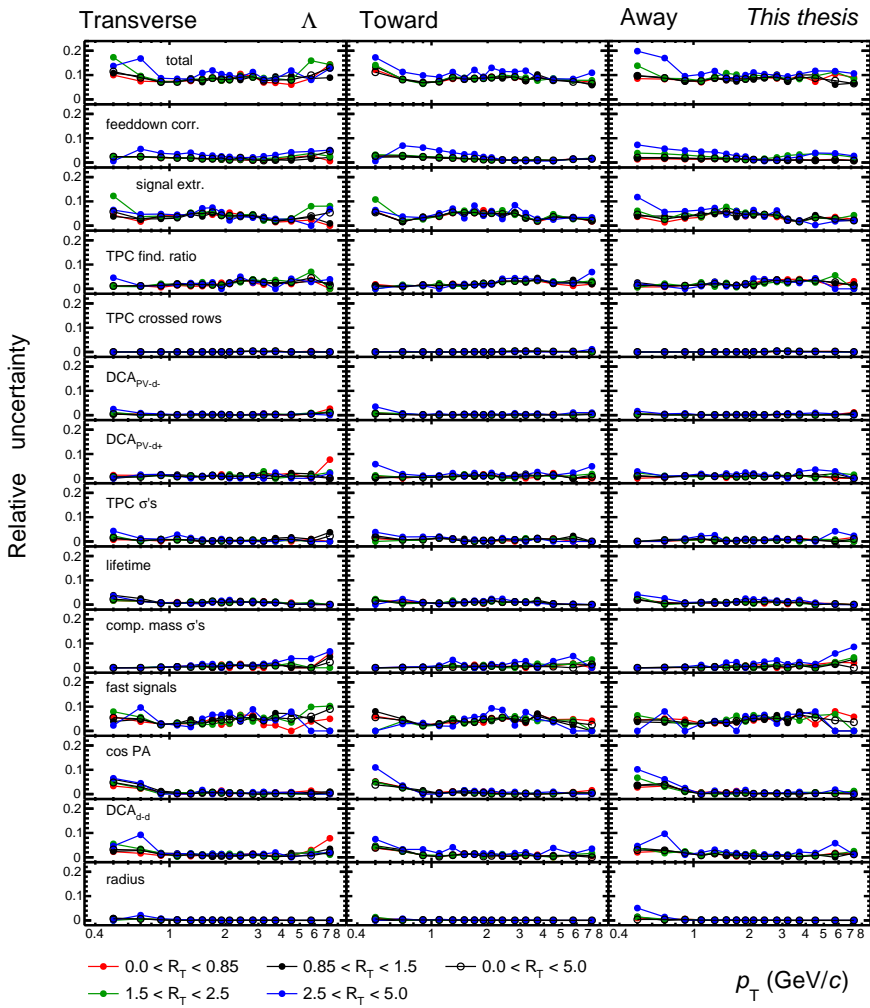


Figure 7.13: Summary of the relative systematic uncertainties on transverse momentum spectra and the individual contributions for Λ in the (left) Transverse, (middle) Toward, and (right) Away in the different R_T intervals.

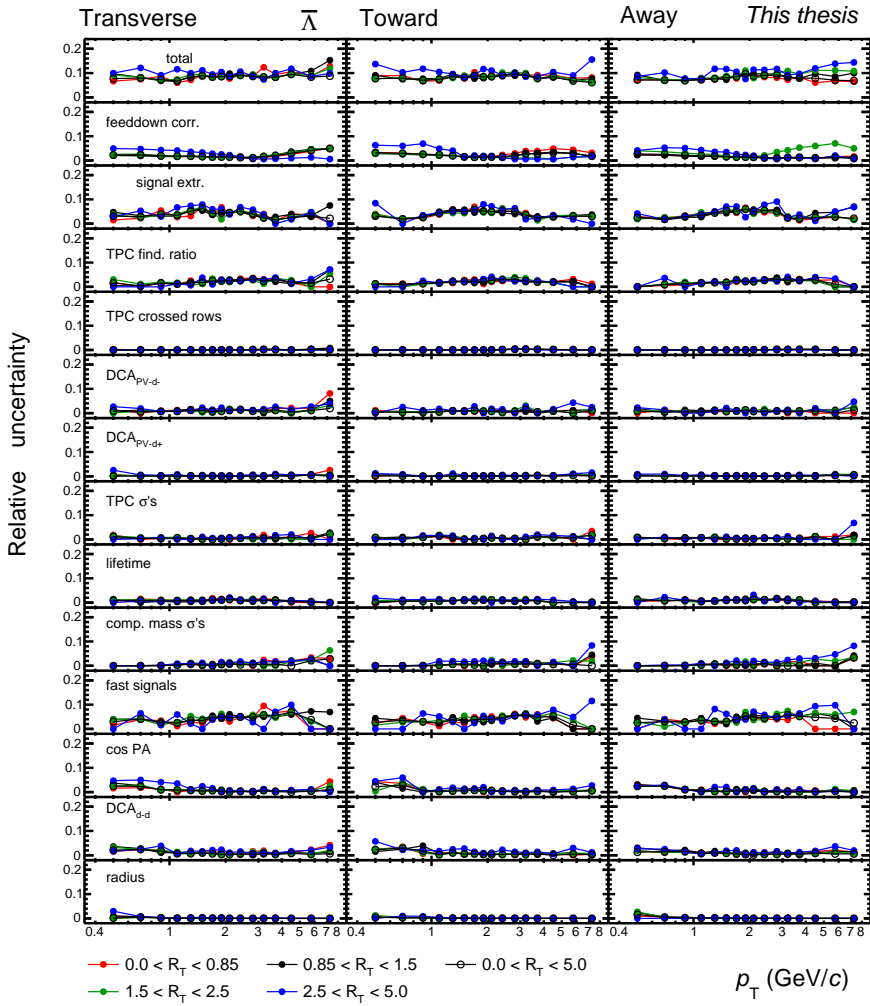


Figure 7.14: Summary of the relative systematic uncertainties on transverse momentum spectra and the individual contributions for $\bar{\Lambda}$ in the (left) Transverse, (middle) Toward, and (right) Away in the different R_T intervals.

7.5.1 Uncertainties from the unfolding procedure

The deviations between the generated p_T spectra and the reconstructed, corrected, and unfolded p_T spectra displayed in Fig. 7.10 were used to determine the systematic uncertainties associated with the unfolding procedure. To isolate the effect of unfolding from other reconstruction effects, the “non-closures” in each $R_T/R_{T,\min}/R_{T,\max}$

interval were divided by the non-closure in the $R_T/R_{T,\min}/R_{T,\max}$ -integrated bin.

The unfolding systematic uncertainties exhibited a large amount of correlation between K_S^0 and Λ . This correlation was expected, as the V^0 species should unfold in similar patterns. Therefore, the systematic uncertainty on the baryon-to-meson ratio was also calculated independently to avoid these correlations and reduce the systematic uncertainty on those results.

Moreover, in the most extreme bins, the non-closures sometimes exhibited unrealistic deviations from unity due to limited statistics and fluctuations. To address this issue, a smoothing procedure was applied by fitting the resulting uncertainties with first- and second-order polynomials. The results are shown in Fig. 7.15.

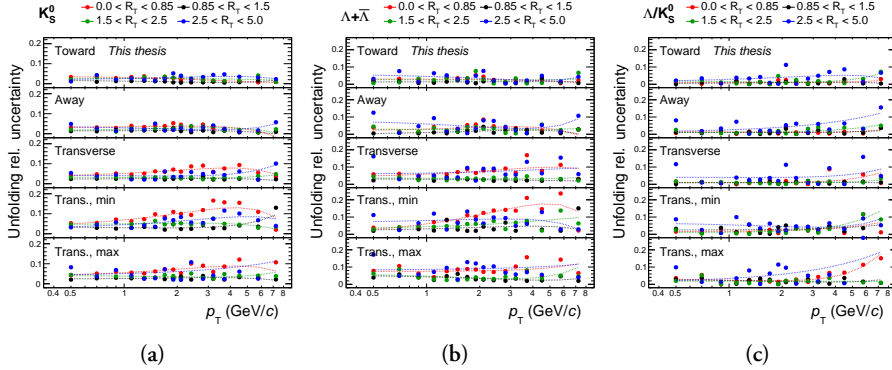


Figure 7.15: Relative systematic uncertainties on transverse momentum spectra resulting from the Bayesian unfolding treatment for the (a) K_S^0 , (b) $\Lambda + \bar{\Lambda}$, (c) and the $(\Lambda^0 + \bar{\Lambda}^0)/(2K_S^0)$ ratio. The smoothed results obtained from first- and second-order polynomial fits are shown as dotted lines.

7.5.2 Uncorrelated uncertainties

Systematic uncertainties may be largely correlated between the different R_T intervals and thus cancel to some degree when reporting ratios of p_T spectra in given R_T bins to the R_T -integrated case. To determine the uncorrelated part, the procedure outlined in Sec. ?? is followed, in the same fashion as in the $S_O^{(p_T=1.0)}$ measurement. They are reported in Appendix ?? and summarised in Tab. ??.

7.6 Description of regions and mean transverse momentum

After unfolding, the average transverse momenta $\langle p_T \rangle$ of K_S^0 and Λ were studied in the Toward, Away, Transverse, Transverse-min, and Transverse-max regions as a function of N_T , $N_{T,\min}$, and $N_{T,\max}$. To guide the focus of the analysis, according to MC paradigms as well as previous UE measurements [167, 170], the following expectations were considered on the origin of the particles:

1. *Toward and Away regions*: particles from jet fragmentation and underlying event.
2. *Transverse region*: particles from UE, which includes contributions from softer MPIs and harder wide-angle initial- and final-state radiation.
3. *Transverse-min region*: particles from UE, where the softer MPI contribution dominates.
4. *Transverse-max region*: particles from UE biased towards higher amounts of harder ISR/FSR.

The choice of the independent observable is then expected to focus on the effects of:

1. *Toward and Away regions*: for all N_T , $N_{T,\min}$, and $N_{T,\max}$, mixing the relative contributions of UE and jet fragmentation.
2. *Transverse(-min,max) regions*: for N_T , the magnitude of the inclusive UE, for $N_{T,\min}$, the magnitude of the softer-MPIs-enhanced MPI, and for $N_{T,\max}$, the magnitude of the harder-ISR/FSR-biased UE.

Fig. 7.16 shows the $K_S^0 \langle p_T \rangle$ results for different configurations. In the Toward and Away regions, the dependence on N_T , $N_{T,\min}$, and $N_{T,\max}$ appears comparable, exhibiting a "jet peak" at low N_T and a flow-like boost from the underlying event at high N_T values. In the Transverse, Transverse-min, and Transverse-max regions, $\langle p_T \rangle$ steeply increases with N_T , with an ordering in terms of absolute values, although the slopes are similar. These results suggest that the choice of particle region does not have a significant impact on its dynamical properties.

Additionally, the increase in $\langle p_T \rangle$ with $N_{T,\max}$ is much steeper in the Transverse-max region compared to the Transverse-min region's increase with $N_{T,\min}$, indicating that the choice of independent variable plays the more important role. Together with the choice of particle region, it has the potential to isolate distinct behaviors between the two activity extremes.

Given these findings, this dissertation focuses on the following measurements: Toward/Away/Transverse versus R_T (N_T), Transverse-min versus $R_{T,\min}$ ($N_{T,\min}$), and Transverse-max versus $R_{T,\max}$ ($N_{T,\max}$).

Alternatively, the $\langle p_T \rangle$ values can be calculated by a re-weighting procedure, which determines $\langle p_T \rangle$ on the pre-unfolded spectra and then sums them together with weights obtained from the smearing matrix [164]. However, this method was not pursued in this dissertation.

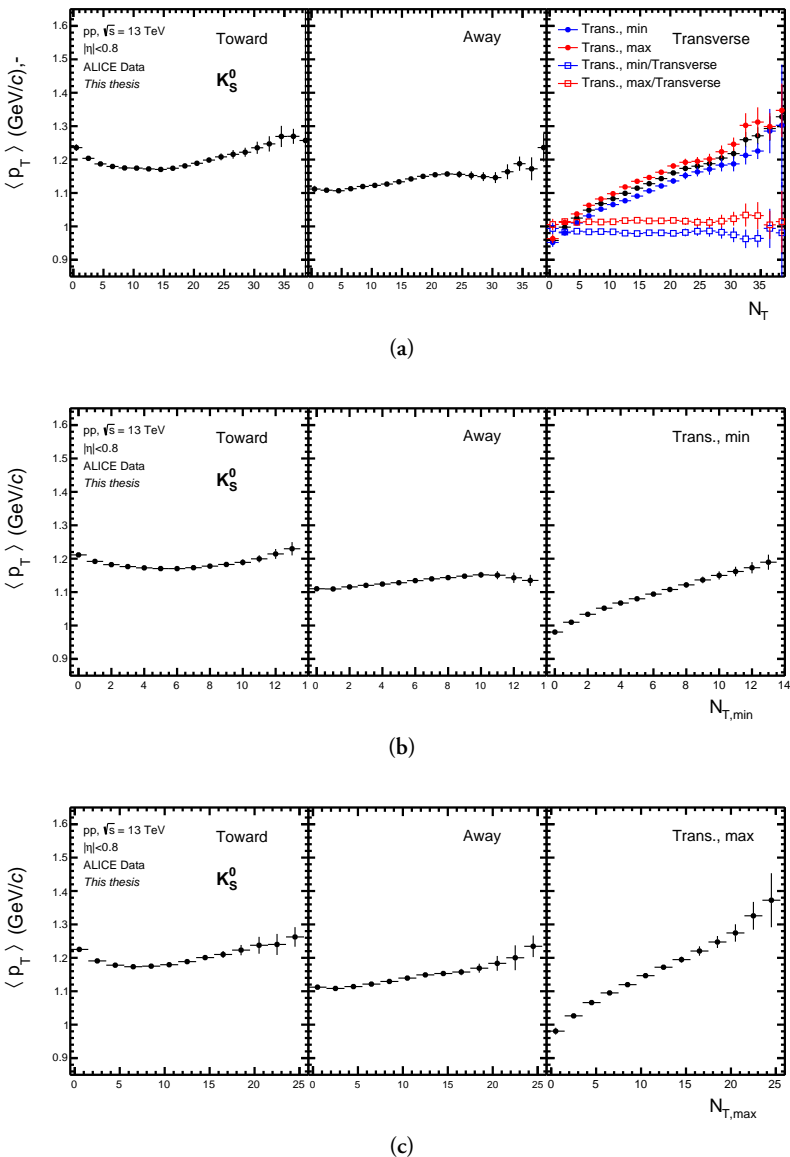


Figure 7.16: Mean transverse momentum for K_S^0 as a function of (a) N_T , (b) $N_{T,\min}$, (c) $N_{T,\max}$ in the different azimuthal regions. The x-axis ranges were chosen such that they represent comparable quantiles of the distributions of their variables, to facilitate a more direct comparison. Only statistical uncertainties are presented and systematic biases on $\langle p_T \rangle$ from the unfolding treatment were not considered.

7.7 Transverse momentum spectra

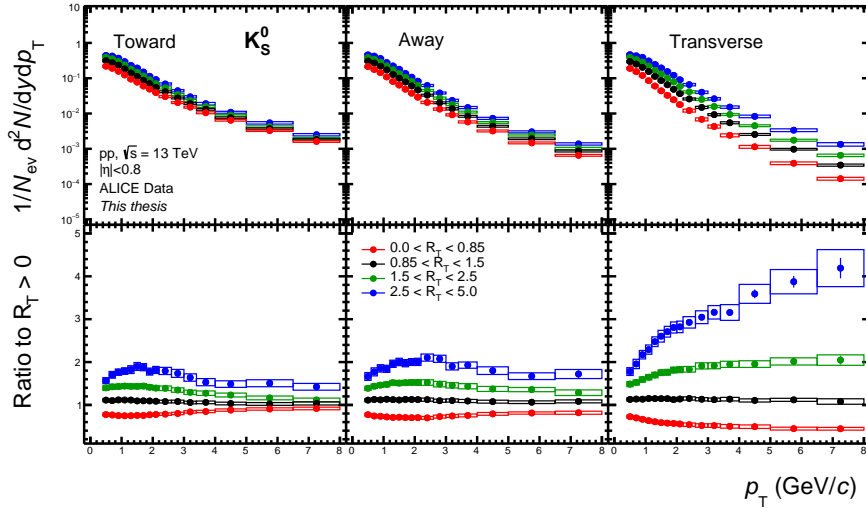
The measured p_T spectra for K_S^0 and Λ , after applying all corrections and accounting for systematic uncertainties, are presented in Fig.7.17 and Fig.7.19, respectively. In addition, these spectra are compared with model predictions in Fig.7.18 and Fig.7.20.

In the Toward and Away regions, there is a dependence at intermediate p_T , followed by a convergence "to a jet" at high p_T . This suggests that high-momentum particles solely originating from jets are independent of the UE, as expected. The Transverse region exhibit an increase and hardening with increasing R_T , indicating that events with higher UE activity are more likely to contain higher- p_T particles. This trend is similar to studies of charged particles at mid-rapidity as a function of N_{ch} measured at mid-rapidity, where the auto-correlation bias is an important factor in interpretation.

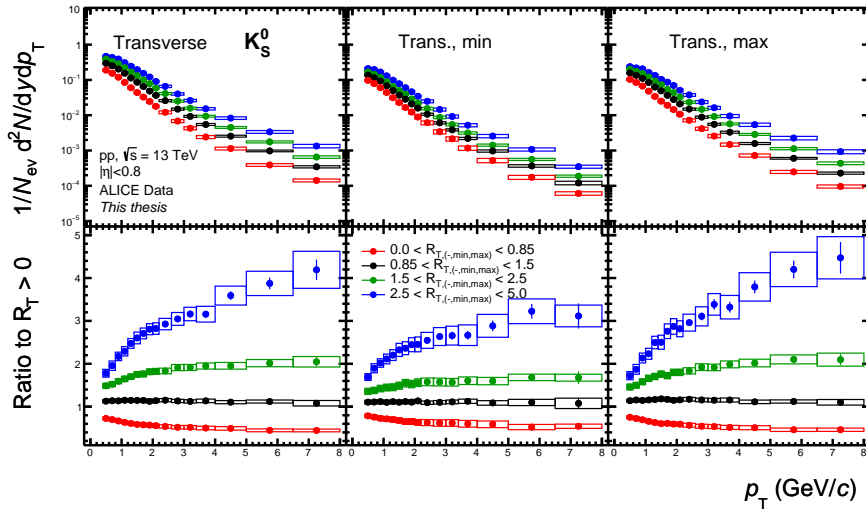
The behavior of the Transverse-max region is similar to that of the Transverse region, indicating the selection of harder wide-angle ISR/FSR. However, the Transverse-min region seems to plateau, suggesting that at higher p_T , $R_{T,min}$ does not impact the particle p_T spectral shapes.

When compared with MC predictions including Pythia Monash, Pythia Ropes, and EPOS LHC, all models reproduce the data qualitatively very well, although quantitative differences can be noticed.

Finally, it is also interesting to remember Pythia and Herwig predictions for inclusive charged particles shown in Fig. 7.5, which showed a steady hardening in high-UE events in the Transverse and Transverse-max regions, whereas a Cronin-like peak was observed for the Transverse-min case. The data reported here offer some support to these expectations but do not explicitly confirm them, suggesting that even higher $R_{T,min}$ values are needed.

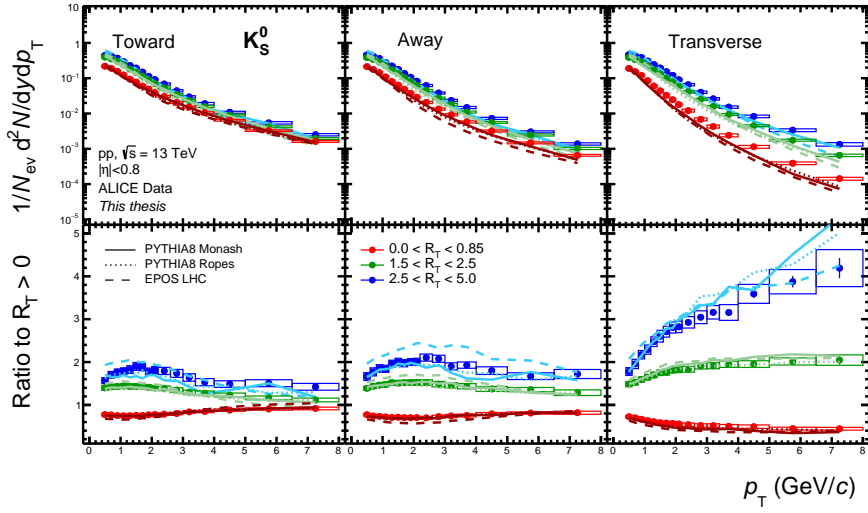


(a)

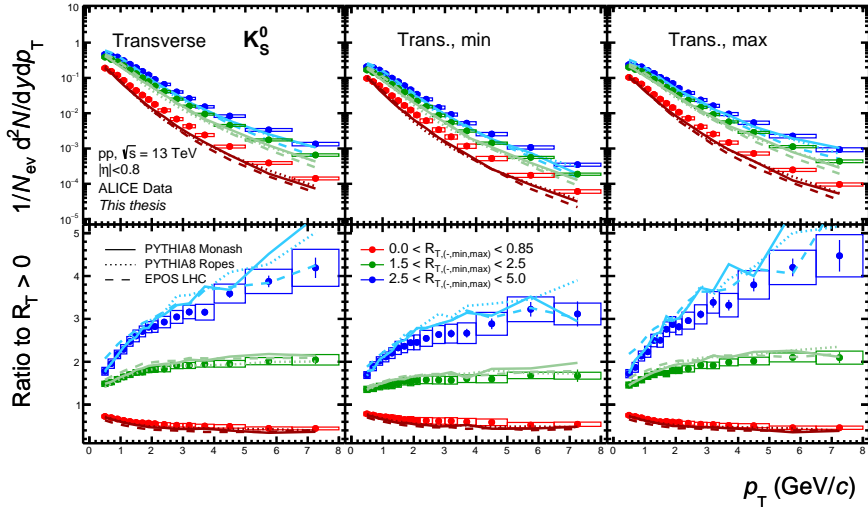


(b)

Figure 7.17: Transverse momentum spectra of K_S^0 for different $R_T/R_{T,\min}/R_{T,\max}$ intervals in pp collisions at $\sqrt{s} = 13$ TeV in (a) Toward, Away, and Transverse, (b) Transverse, Transverse-min, and Transverse-max regions. The bottom panels display ratios to the $R_T/R_{T,\min}/R_{T,\max}$ -integrated cases. The error bars represent statistical uncertainties and the rectangles show the systematic uncertainties.

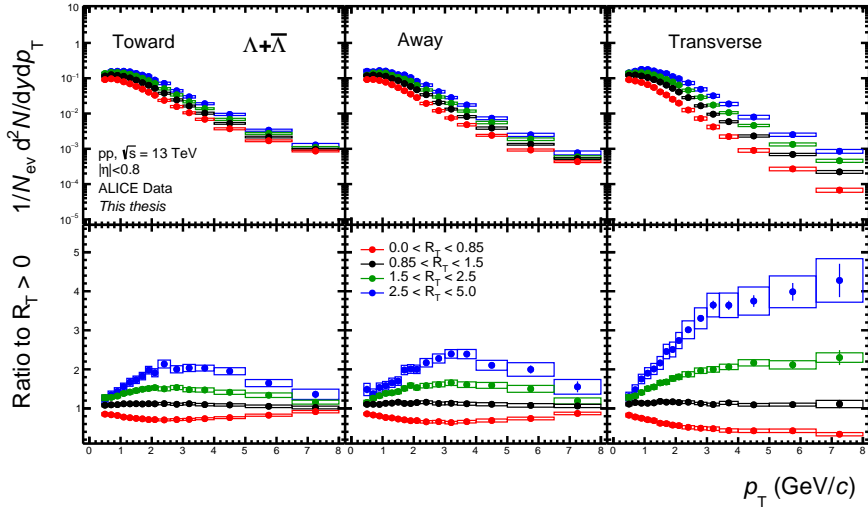


(a)

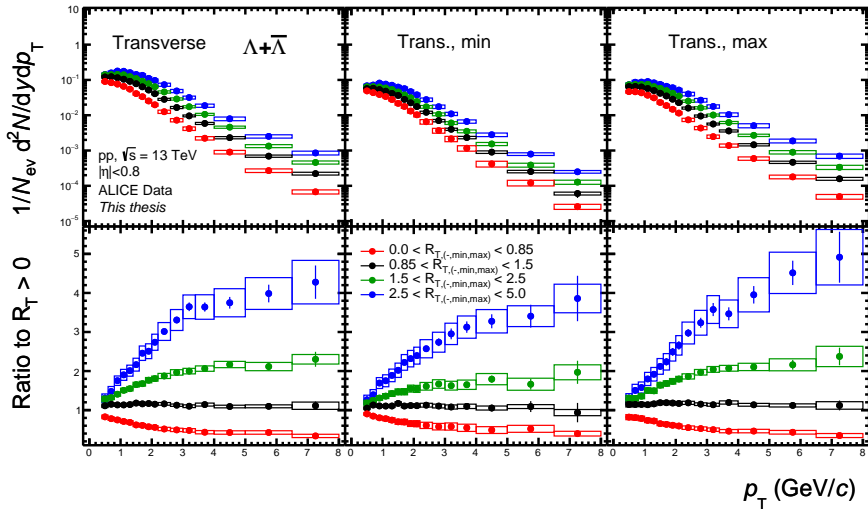


(b)

Figure 7.18: Transverse momentum spectra of K_S^0 for different $R_T/R_{T,\text{min}}/R_{T,\text{max}}$ intervals in pp collisions at $\sqrt{s} = 13$ TeV compared with MC predictions in (a) Toward, Away, and Transverse, (b) Transverse, Transverse-min, and Transverse-max regions. The bottom panels display ratios to the $R_T/R_{T,\text{min}}/R_{T,\text{max}}$ -integrated cases. The error bars represent statistical uncertainties and the rectangles show the systematic uncertainties.

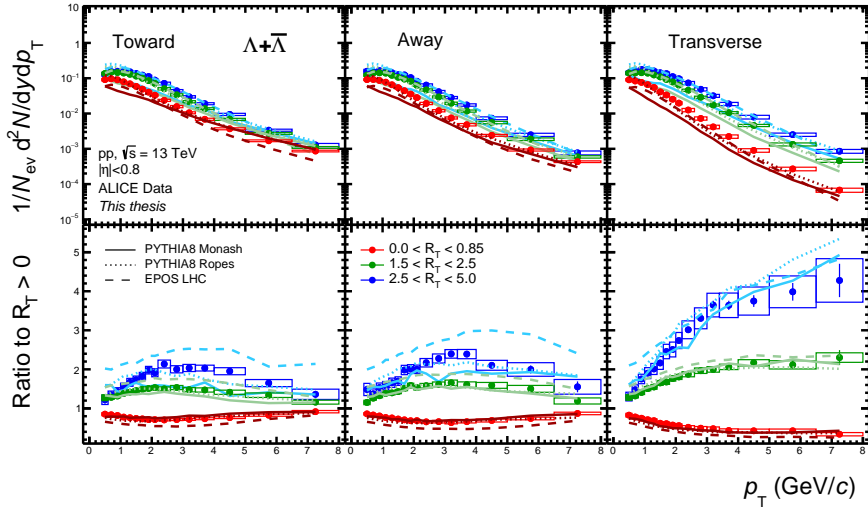


(a)

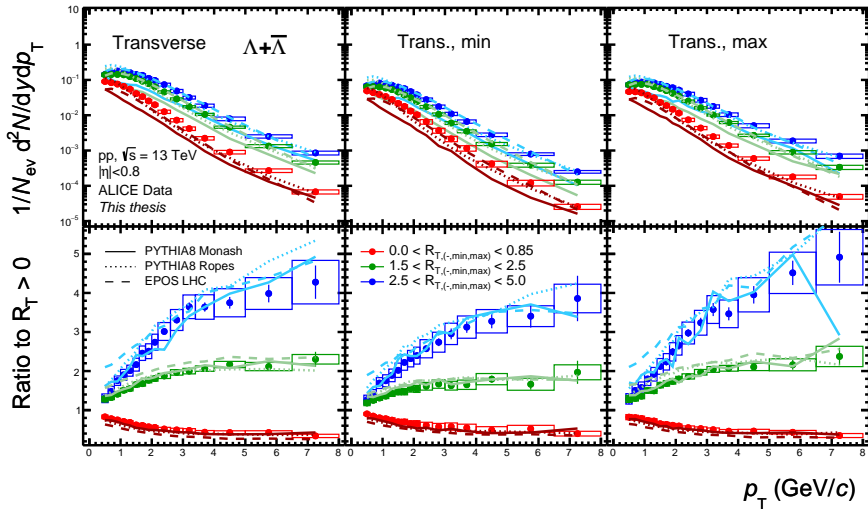


(b)

Figure 7.19: Transverse momentum spectra of $\Lambda + \bar{\Lambda}$ for different $R_T/R_{T,min}/R_{T,max}$ intervals in pp collisions at $\sqrt{s} = 13$ TeV in (a) Toward, Away, and Transverse, (b) Transverse, Transverse-min, and Transverse-max regions. The bottom panels display ratios to the $R_T/R_{T,min}/R_{T,max}$ -integrated cases. The error bars represent statistical uncertainties and the rectangles show the systematic uncertainties.



(a)



(b)

Figure 7.20: Transverse momentum spectra of $\Lambda + \bar{\Lambda}$ for different $R_T/R_{T,min}/R_{T,max}$ intervals in pp collisions at $\sqrt{s} = 13$ TeV compared with MC predictions in (a) Toward, Away, and Transverse, (b) Transverse, Transverse-min, and Transverse-max regions. The bottom panels display ratios to the $R_T/R_{T,min}/R_{T,max}$ -integrated cases. The error bars represent statistical uncertainties and the rectangles show the systematic uncertainties.

7.8 Baryon-to-meson ratio

To investigate the observable most directly linked to radial flow studies, the baryon-to-meson ratios, the $(\Lambda^0 + \bar{\Lambda}^0)/(2K_s^0)$ results are presented in Fig.7.22, and model predictions are compared in Fig.7.23.

Noteworthily, the biggest dependence on UE activity can be observed in the Toward and Away regions. Although this may not be immediately intuitive, as one may naively expect these regions to be dominated by jets and thus insensitive to softer phenomena like radial flow, there is a somewhat straightforward interpretation. In this region, R_T controls the amount of interplay between jet-related and UE-related production, which may differ for the K_s^0 and Λ . Indeed, ALICE measurements of $(\Lambda^0 + \bar{\Lambda}^0)/(2K_s^0)$ ratios inside reconstructed jet cones and outside of them reveal a drastic difference, shown in Fig. 7.21, further suggesting that the difference in production regime plays a significant role here, rather than any collective-flow-like behavior due to increased n_{MPI} .

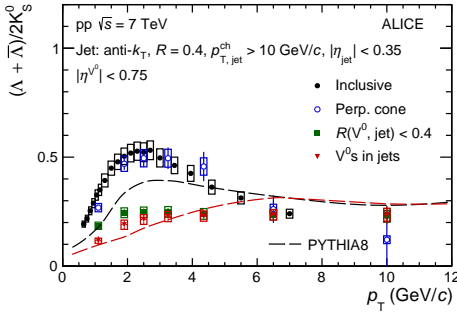
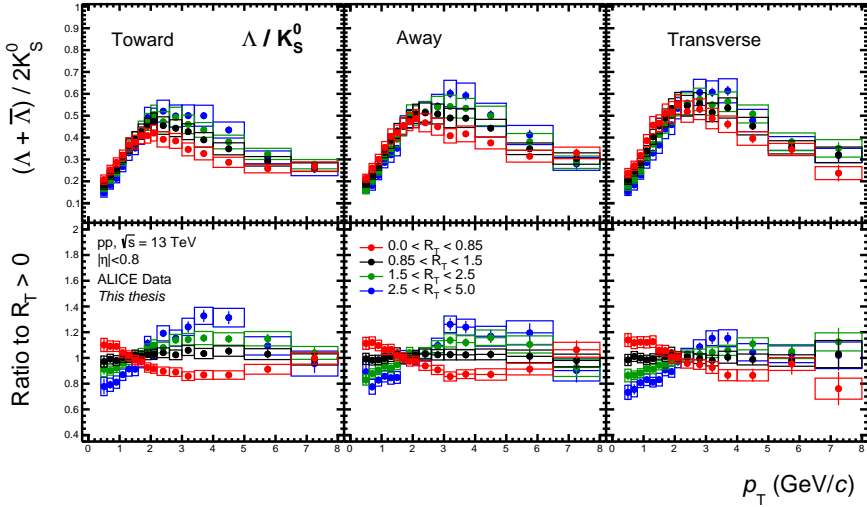


Figure 7.21: The $(\Lambda^0 + \bar{\Lambda}^0)/(2K_s^0)$ ratio measured with ALICE in pp collisions at $\sqrt{s} = 7$ TeV in events with high- p_T jets, based on their origin: inclusive (black), inside the jet cone (green), perpendicular to the jet (blue), and in jets with the UE subtracted (red). [158]

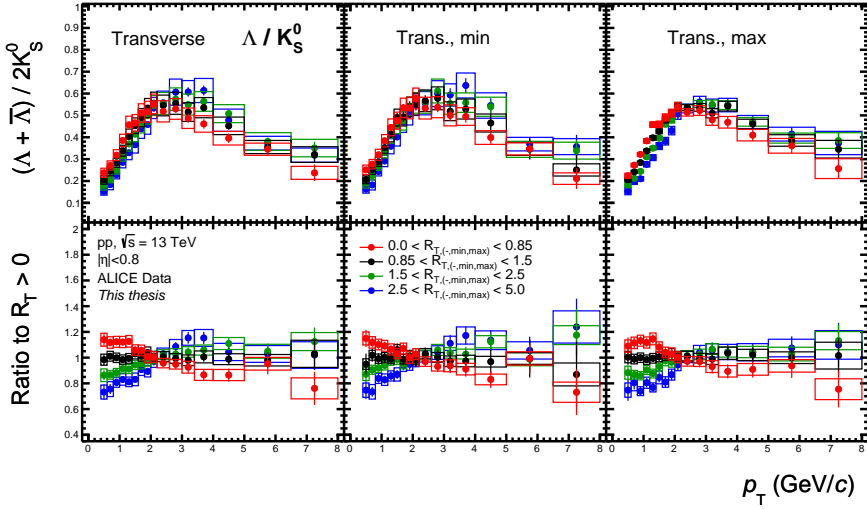
In contrast to the $S_O^{(p_T=1.0)}$ findings, the Transverse region exhibits typical radial flow patterns: enhancement of the ratio at intermediate p_T , corresponding depletion at low p_T , and an overall shift of the peak by about 1 GeV/c. The Transverse-min and Transverse-max regions appear to behave very similarly, with small hints of the Transverse-min exhibiting a slightly bigger effect than the Transverse-max, although the results suffer from significant statistical uncertainties. Therefore, more precise measurements are needed to confirm this observation.

Based on the selected models, the Pythia Ropes predictions are the most consistent with the data, whereas EPOS LHC exhibits a much larger dependence on R_T , and Pythia Monash significantly underestimates the ratios. The latter two models also demonstrate smaller variations of $(\Lambda^0 + \bar{\Lambda}^0)/(2K_s^0)$ across different regions than the

experimental data. Nevertheless, all the model predictions are generally consistent with describing the ratios to the R_T -integrated case. Overall, these results suggest that mechanisms that account for interactions between MPI, such as the Pythia Ropes model's implementation of increasing tension strength of many overlapping strings, are a step in the right direction.

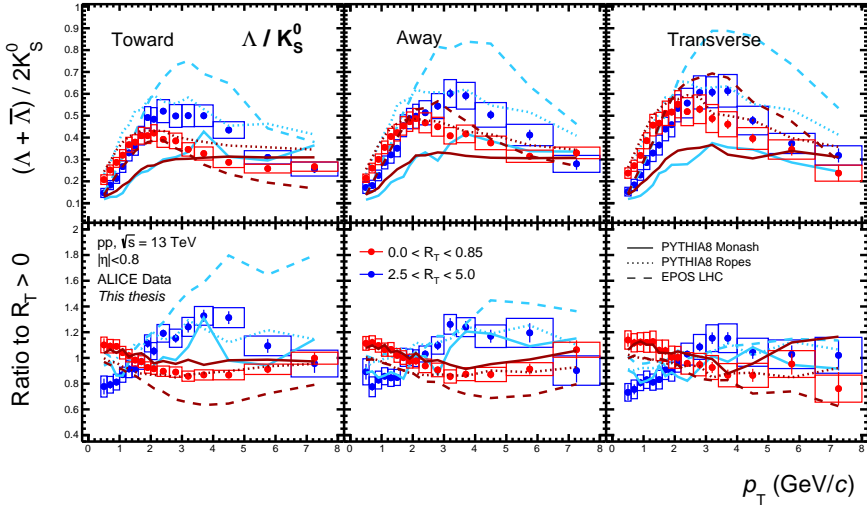


(a)

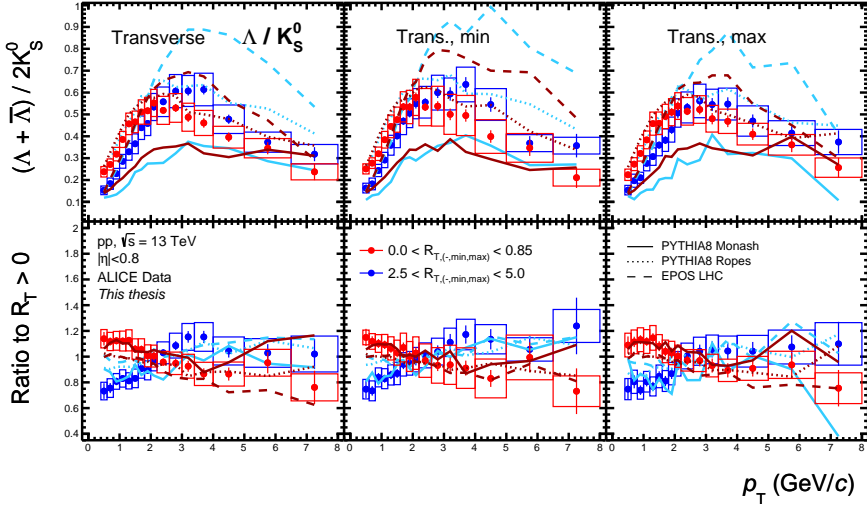


(b)

Figure 7.22: Baryon-to-meson ratios of p_T spectra $(\Lambda^0 + \bar{\Lambda}^0)/(2K_s^0)$ for different $R_T/R_{T,\text{min}}/R_{T,\text{max}}$ intervals in pp collisions at $\sqrt{s} = 13$ TeV in (a) Toward, Away, and Transverse, (b) Transverse, Transverse-min, and Transverse-max regions. The bottom panels display ratios to the $R_T/R_{T,\text{min}}/R_{T,\text{max}}$ -integrated cases. The error bars represent statistical uncertainties and the rectangles show the systematic uncertainties.



(a)



(b)

Figure 7.23: Baryon-to-meson ratios of p_T spectra $(\Lambda^0 + \bar{\Lambda}^0)/(2K_s^0)$ for different $R_{T,R_{T,min}}/R_{T,max}$ intervals in pp collisions at $\sqrt{s} = 13$ TeV in (a) Toward, Away, and Transverse, (b) Transverse, Transverse-min, and Transverse-max regions, compared with MC predictions. The bottom panels display ratios to the $R_{T,R_{T,min}}/R_{T,max}$ -integrated cases. The error bars represent statistical uncertainties and the rectangles show the systematic uncertainties.

7.9 Integrated yields

Finally, in Fig. 7.24, the integrated yields of K_S^0 and Λ are shown as a function of R_T , $R_{T,\min}$, and $R_{T,\max}$. The yields are self-normalised, similar to other multiplicity-dependent particle production measurements by ALICE. Using the same approach as in the $S_O^{(p_T=1.0)}$ measurement, for the V^0 s, the reported p_T range is used to integrate the yields, rather than extrapolating. The yields are then compared to data on pions and protons, as well as model predictions.

The yields of K_S^0 and Λ increase with R_T , but at a slower rate than the underlying UE activity (same rate would correspond to $y = x$). The increase of Λ with R_T appears to be somewhat faster than K_S^0 , which is in contrast to similar measurements using forward-rapidity event activity classifier [94]. The largest increase in yields is observed in the Transverse and Transverse-max regions, with the Transverse-min region showing a slightly slower increase. In the Toward and Away regions, the increase in yields appears to be slower than linear.

When comparing the yields of charged particles [157], the effect of decoupling the neutral K_S^0 and Λ from the N_T in the Transverse region is evident. There is also slight, albeit systematic evidence for strangeness enhancement in the Toward and Away regions, with K_S^0 increasing slightly faster than π and Λ slightly faster than p . However, the uncertainties are significant, and strong conclusions cannot be drawn.

Based on the selected models, Pythia Monash and Pythia Ropes predict values that are consistent with the experimental data. EPOS LHC is also consistent in the Transverse regions but exhibits a faster rise with R_T than what is observed. In addition, it is less sensitive to the choice of regions compared to the other models.

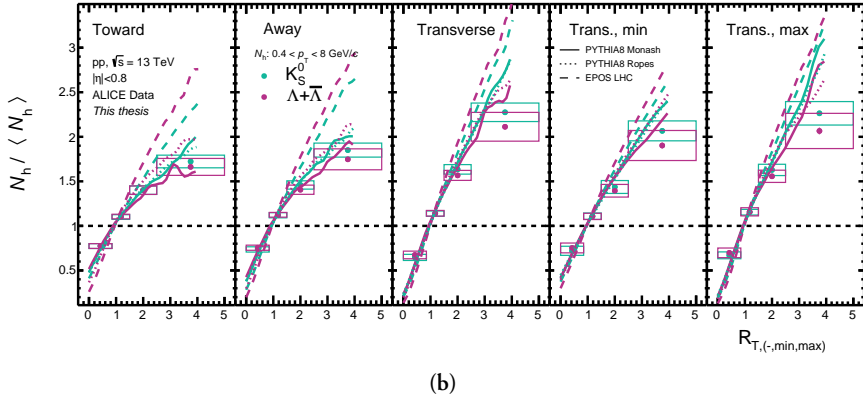
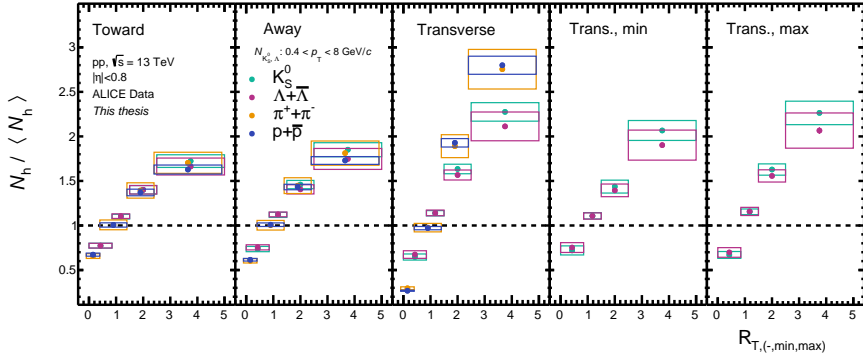


Figure 7.24: Self-normalised yields of K_S^0 and $\Lambda + \bar{\Lambda}$ as a function of $R_T/R_{T,\min}/R_{T,\max}$, the self-normalised mid-rapidity underlying event activity, compared with (a) charged particles [157] and (b) MC predictions. The K_S^0 and $\Lambda + \bar{\Lambda}$ yields are determined by integration in the reported p_T range. Datapoints are centered to the median R_T values, and not $\langle R_T \rangle$, of the given intervals. Statistical and systematic uncertainties are indicated by vertical error bars and boxes, respectively.

Chapter 8

Discussion of results, conclusions, and outlooks

8.1 Summary of the research goals

The first part of this dissertation provides an introduction to quantum chromodynamics (QCD), a theory of the fundamental strong force of the Universe, and explains why QCD interactions involving low-momentum (soft) transfers cannot be calculated from first principles, unlike hard processes, which can use perturbation theory. Next, the importance of studying QCD matter at extreme conditions is discussed, specifically the plasma of deconfined quarks and gluons QGP.

Furthermore, the dissertation presents an overview of experimental studies that investigate the properties and signatures of the QGP in AA collisions and their dependence on collision centrality, which can be related to energy densities as well as final-state multiplicities in the system. Special attention is given to the phenomena of strangeness enhancement, where strange particles are produced more abundantly in more active collisions, and collective flow, where the hydrodynamic behavior of the plasma affects the dynamics of final-state hadrons.

The dissertation also describes the challenges to traditional paradigms that pp collisions were thought to be incapable of producing extremes of QCD matter, and lists the observations resembling traditional QGP phenomena in these small system collisions. Moreover, it explains the intricacies of isolating the physics behind these phenomena, given that event multiplicity arises from non-perturbative (softer) as well as perturbative (harder) processes, is susceptible to large fluctuations, and cannot be directly linked to the energy density.

The goal of this dissertation is to provide a clearer and more differential study of QGP phenomena, namely strangeness enhancement and radial flow, and to elucidate the roles played by both soft and hard processes. The aim is to identify and utilise observables that isolate events with extreme activity resulting from non-perturbative processes, where novel physics may be at play, such as the formation of a QGP-like state or complex interactions of overlapping QCD fields. Two state-of-the-art phenomenological models are used to represent these paradigms: EPOS LHC, which includes QGP droplets, and the Ropes tune of Pythia 8, which allows for the merging of strings into higher-tension fields. These observables should also be capable of isolating event activity extremes dominated by perturbative physics at the other end of the spectrum.

Given the complexity of the physics picture and its need to be studied from various angles, these measurements are unlikely to single-handedly confirm or reject the “big hypothesis” of whether QGP can be formed in pp collisions. Nevertheless, they will be able to provide valuable insight into the underlying physics processes in hadronic and partonic interactions and their deeper understanding. Furthermore, the measurements have the potential to significantly discriminate between different phenomenological models.

8.2 Highlights of the $S_O^{(p_T=1.0)}$ measurement

Chapter 6 introduces measurements of the neutral, weakly decaying K_S^0 , Λ , and $\bar{\Lambda}$ as a function of transverse spherocity $S_O^{(p_T=1.0)}$ in pp collisions at $\sqrt{s} = 13$ TeV using the ALICE detector at the LHC. This observable describes the geometrical shape of the charged particles produced in the collision and provides a simple, albeit effective discriminator between pencil-like events, dominated by a di-jet coming from a single hard partonic scattering, and isotropic events, where particles are produced from multiple sources involving lower momentum transfers.

These measurements provide the first ever experimental results of these strange particles as a function of an event shape observable. Moreover, they develop and utilise the so-called unweighted spherocity, a modification from its traditional form S_O , which is easier to compare with phenomenological models. The results are fully corrected and come with a thorough investigation of their experimental uncertainties.

In this dissertation, the following results are presented: transverse momentum p_T spectra, average $\langle p_T \rangle$, ratios of p_T spectra to pions, baryon-to-meson ratios, and integrated production yields as a function of $S_O^{(p_T=1.0)}$ in high-multiplicity events. The following findings can be highlighted:

1. Figure 6.7 shows that $S_O^{(p_T=1.0)}$ has interplays with the event multiplicity:
 - If high multiplicity is determined at forward-rapidity (V0M), $S_O^{(p_T=1.0)}$ varies mostly the mid-rapidity multiplicity, leading to more constant increases and decreases in particle spectra between jetty and isotropic events (Fig. 6.14).
 - If high multiplicity is determined at mid-rapidity ($N_{\text{SPD}_{\text{Trkts}}}$), $S_O^{(p_T=1.0)}$ varies mostly the $\langle p_T \rangle$, leading to similar yields but significant hardening and softening between jetty and isotropic events (Fig. 6.14 and Fig. 6.16).
2. Generally, the isotropic spectra are closer to the $S_O^{(p_T=1.0)}$ -unbiased spectra than the jetty are, suggesting that average high-multiplicity collisions are somewhat isotropic, whereas jetty events are outliers.
3. Ratios to pions in Fig. 6.18 reveal that relatively to pions, K_S^0 and Λ are consistently suppressed in jetty events and enhanced in isotropic events in $N_{\text{SPD}_{\text{Trkts}}}$ classes. This effect is different in the V0M class.
4. The baryon-to-meson ratios $(\Lambda^0 + \bar{\Lambda}^0)/(2K_S^0)$ in Fig. 6.19 display an enhancement of Λ in intermediate p_T in isotropic events. This is expected with observing radial flow, however, its other characteristic features, such as shift of the peak, are not seen.
5. Ratios of integrated yields to pions in Fig. 6.20 show a characteristic strangeness enhancement behaviour for the $N_{\text{SPD}_{\text{Trkts}}}$ class and the effect increases with increasing the mass and strangeness content. This result is the first observation ever of strangeness enhancement that occurs with (mostly) constant multiplicity. In the V0M class, the effect is not observed.
6. Results are compared with selected MC predictions, mostly favouring Pythia 8 Ropes and EPOS LHC over Pythia 8 Monash, although with varying degrees of success.

8.3 Highlights of the R_T measurements

Chapter 7 presents measurements of the production of K_S^0 , Λ , and $\bar{\Lambda}$ in pp collisions at $\sqrt{s} = 13$ TeV and their dependence on the relative underlying event activity R_T . This quantity controls the magnitude of the underlying event, which consists of many softer particles produced through multiple partonic interactions (MPIs) and other sources, and is unrelated to the primary hard partonic scatterings and its fragmentation. It acts as a dial, selecting events resembling ee collisions ($R_T \rightarrow 0$, $n_{\text{MPI}} \rightarrow 1$)

and AA collisions ($R_T \rightarrow \infty$, $n_{\text{MPI}} \rightarrow \infty$). Particle production is studied in three azimuthal regions based on the highest- p_T track, which serves as a proxy for the primary scattering axis: Towards, Away, and Transverse.

Moreover, to distinguish between the contributions to the underlying event from softer (MPIs) and harder (wide-angle radiation ISR/FSR) interactions, this approach is extended to divide the Transverse region further into Transverse-min and Transverse-max based on the number of particles, and define the classifiers $R_{T,\text{min}}$ and $R_{T,\text{max}}$, accordingly. At the time of conducting this measurement, the $R_{T,\text{min}}$ observable is expected to be the cleanest probe of the $\langle n_{\text{MPI}} \rangle$, as the harder contributions are captured in the $R_{T,\text{max}}$ quantity.

The measurements presented in this dissertation are the first ever experimental results of K_S^0 , Λ , and $\bar{\Lambda}$ as a function of R_T , as well as the first use ever of $R_{T,\text{min}}$ and $R_{T,\text{max}}$ on identified particles. Considerable effort has been required to experimentally use and understand these observables, particularly in the choice of tracks used, the treatment with Bayesian unfolding, and the quantification of systematic uncertainties.

The following results are focused on: p_T spectra, $\langle p_T \rangle$, baryon-to-meson ratios, and self-normalised yields. Key outcomes of this study are:

1. Figure 7.16 implies a much steeper increase of $\langle p_T \rangle$ of K_S^0 with $R_{T,\text{max}}$ than $R_{T,\text{min}}$.
2. The transverse momentum spectra in Fig. 7.17 and Fig. 7.19 show:
 - In the Toward region, the spectra in different R_T events converge at high p_T to the R_T -integrated values, corresponding to the dominance of jet.
 - In the Transverse region, p_T spectra continue hardening with increasing R_T , similarly to the picture in multiplicity measurements.
 - In contrast, the Transverse-min region seems to plateau.
3. The baryon-to-meson ratios in Fig. 7.22 reveal typical radial flow features in high- R_T events, including the enhancement of intermediate- p_T baryons, their depletion at low- p_T , as well as shifts of the peaks. Moreover,
 - In the Toward region, the effect is the largest. This is due to the mixing of jet- and UE-related particle production, which shows largely different $(\Lambda^0 + \bar{\Lambda}^0)/(2K_S^0)$ ratios.
 - The effect is comparable among the Transverse, Transverse-min, and Transverse-max regions, with only small hints of being slightly bigger in the Transverse-min case. This suggests that the harder and softer components of UE affect the relative production of Λ and K_S^0 in a similar fashion.

4. The self-normalised yields in Fig. 7.24 of K_S^0 and Λ are consistent with π and p , respectively, in the Toward and Away regions, although more experimental precision is needed. In the Transverse region, the effect of auto-correllation is apparent for the charged particles. Moreover, the K_S^0 and Λ yields rise more slowly in the Transverse-min cases than the Transverse-max.
5. The experimental data favour the Pythia 8 Ropes predictions. EPOS LHC does not display the right amount of sensitivity to the azimuthal region and the Pythia 8 Monash tune underestimates the effects of radial flow. This implies that Colour Reconnection is somewhat insufficient to describe the flow-like behaviour.
6. Generally, higher values of $R_T/R_{T,\min}/R_{T,\max}$ observables need to be reached in order to isolate the different behaviours of softer MPIs and harder ISR/FSR and further test the MC predictions.

8.4 Conclusions and Outlooks

One paragraph wrap-up? One paragraph about possible improvements One paragraph about other areas for exploration

Part IV

Appendices

Appendix A

List of Acronyms

Lorem ipsum dolor sit amet, consectetuer adipiscing elit. Etiam lobortis facilisis sem. Nullam nec mi et neque pharetra sollicitudin. Praesent imperdiet mi nec ante. Donec ullamcorper, felis non sodales commodo, lectus velit ultrices augue, a dignissim nibh lectus placerat pede. Vivamus nunc nunc, molestie ut, ultricies vel, semper in, velit. Ut porttitor. Praesent in sapien. Lorem ipsum dolor sit amet, consectetuer adipiscing elit. Duis fringilla tristique neque. Sed interdum libero ut metus. Pellentesque placerat. Nam rutrum augue a leo. Morbi sed elit sit amet ante lobortis sollicitudin. Praesent blandit blandit mauris. Praesent lectus tellus, aliquet aliquam, luctus a, egestas a, turpis. Mauris lacinia lorem sit amet ipsum. Nunc quis urna dictum turpis accumsan semper.

Appendix B

Mathematical Derivations

Lore*m* ipsum dolor sit amet, consectetuer adipiscing elit. Etiam lobortis facilisis sem. Nullam nec mi et neque pharetra sollicitudin. Praesent imperdiet mi nec ante. Donec ullamcorper, felis non sodales commodo, lectus velit ultrices augue, a dignissim nibh lectus placerat pede. Vivamus nunc nunc, molestie ut, ultricies vel, semper in, velit. Ut porttitor. Praesent in sapien. Lore*m* ipsum dolor sit amet, consectetuer adipiscing elit. Duis fringilla tristique neque. Sed interdum libero ut metus. Pellentesque placerat. Nam rutrum augue a leo. Morbi sed elit sit amet ante lobortis sollicitudin. Praesent blandit blandit mauris. Praesent lectus tellus, aliquet aliquam, luctus a, egestas a, turpis. Mauris lacinia lorem sit amet ipsum. Nunc quis urna dictum turpis accumsan semper.

Appendix C

Complementary Material

Lorem ipsum dolor sit amet, consectetuer adipiscing elit. Etiam lobortis facilisis sem. Nullam nec mi et neque pharetra sollicitudin. Praesent imperdiet mi nec ante. Donec ullamcorper, felis non sodales commodo, lectus velit ultrices augue, a dignissim nibh lectus placerat pede. Vivamus nunc nunc, molestie ut, ultricies vel, semper in, velit. Ut porttitor. Praesent in sapien. Lorem ipsum dolor sit amet, consectetuer adipiscing elit. Duis fringilla tristique neque. Sed interdum libero ut metus. Pellentesque placerat. Nam rutrum augue a leo. Morbi sed elit sit amet ante lobortis sollicitudin. Praesent blandit blandit mauris. Praesent lectus tellus, aliquet aliquam, luctus a, egestas a, turpis. Mauris lacinia lorem sit amet ipsum. Nunc quis urna dictum turpis accumsan semper.

Appendix D

Scientific Publications

Author contributions

Paper I: Title paper 1

I participated in developing the theory and wrote the simulation software. I participated in writing the manuscript.

Paper II: Title paper 2

I participated in developing the theory and writing simulation software. I participated in writing the manuscript.

Paper I

S. Doctor and B. someone

An Exact Ewald Summation Method in Theory and Practice

The Journal of Physical Chemistry A, 2020, 124(19), pp. 3943-3946

Reproduced with permission from *J. Phys. Chem. A*

Copyright 2020 American Chemical Society.

Hello, I am an article

Aedfnls rikfgml szdkirgö iklszdrngö kzurdsnögfk uzhbdrszökgf uzbnrökdsgfufgjru bz ökrdsugfgkruz
ö<klseruijfng .-<jls <rnf.k jxzdbndnrtxökgku özdxnrikögjl dzxr

Paper II

S. Doctor, B. someone, C. another and D. another

Grand canonical simulations of ions between charged conducting surfaces using exact
3D Ewald summations

Physical Chemistry Chemical Physics, 2020, 22(24), pp. 13659-13665

Reproduced from *Phys. Chem. Chem. Phys.* with permission from the PCCP Owner Societies.

Hello, I am another article

Sergt sdetrqty sdrtgt xtcdhgh dxtrggbs zdrtgt xfdth szdtfgh dxft

References

- [1] M. Tanabashi *et al.*, “Review of Particle Physics,” *Phys. Rev. D*, vol. 98, no. 3, p. 030001, 2018.
- [2] P. W. Higgs, “Broken Symmetries and the Masses of Gauge Bosons,” *Phys. Rev. Lett.*, vol. 13, no. 16, pp. 508–509, Oct. 1964.
- [3] F. Englert and R. Brout, “Broken Symmetry and the Mass of Gauge Vector Mesons,” *Phys. Rev. Lett.*, vol. 13, no. 9, pp. 321–323, Aug. 1964.
- [4] The ATLAS Collaboration, “Observation of a new particle in the search for the Standard Model Higgs boson with the ATLAS detector at the LHC,” *Physics Letters B*, vol. 716, no. 1, pp. 1–29, Sep. 2012.
- [5] T. C. Collaboration, “Observation of a new boson at a mass of 125 GeV with the CMS experiment at the LHC,” *Physics Letters B*, vol. 716, no. 1, pp. 30–61, Sep. 2012.
- [6] H. Fritzsch, “Fundamental Constants at High Energy,” *Fortschr. Phys.*, vol. 50, no. 5-7, pp. 518–524, May 2002.
- [7] B. Delamotte, “A hint of renormalization,” *American Journal of Physics*, vol. 72, no. 2, pp. 170–184, Feb. 2004.
- [8] B. Odom *et al.*, “New Measurement of the Electron Magnetic Moment Using a One-Electron Quantum Cyclotron,” *Phys. Rev. Lett.*, vol. 97, no. 3, p. 030801, Jul. 2006.
- [9] G. Altarelli, “A QCD Primer,” in *AIP Conference Proceedings*, vol. 631, 2002, pp. 70–III.
- [10] H. D. Politzer, “Reliable Perturbative Results for Strong Interactions?” *Phys. Rev. Lett.*, vol. 30, no. 26, pp. 1346–1349, Jun. 1973.

- [11] A. Deur, S. J. Brodsky, and G. F. de Teramond, “The QCD Running Coupling,” *Progress in Particle and Nuclear Physics*, vol. 90, pp. 1–74, Sep. 2016.
- [12] D. J. Gross and F. Wilczek, “Asymptotically Free Gauge Theories. I,” *Phys. Rev. D*, vol. 8, no. 10, pp. 3633–3652, Nov. 1973.
- [13] G. Dissertori, “The Determination of the Strong Coupling Constant,” Oct. 2016, vol. 26, pp. 113–128.
- [14] Particle Data Group *et al.*, “Review of Particle Physics,” *Progress of Theoretical and Experimental Physics*, vol. 2022, no. 8, p. 083Cor, Aug. 2022.
- [15] S. Prestel, “Particle Physics Phenomenology,” Lund University.
- [16] G. Altarelli and G. Parisi, “Asymptotic freedom in parton language,” *Nuclear Physics B*, vol. 126, no. 2, pp. 298–318, Aug. 1977.
- [17] J. C. Collins, D. E. Soper, and G. Sterman, “Factorization of Hard Processes in QCD,” Sep. 2004.
- [18] A. M. Cooper-Sarkar, “Extraction of the proton parton density functions using a NLO-QCD fit of the combined H1 and ZEUS inclusive DIS cross sections,” Aug. 2008.
- [19] C. Marquet and G. Soyez, “The Balitsky-Kovchegov equation in full momentum space,” *Nuclear Physics A*, vol. 760, no. 1-2, pp. 208–222, Oct. 2005.
- [20] STAR Collaboration *et al.*, “Evidence for Nonlinear Gluon Effects in QCD and Their Mass Number Dependence at STAR,” *Phys. Rev. Lett.*, vol. 129, no. 9, p. 092501, Aug. 2022.
- [21] S. Ferreres-Solé and T. Sjöstrand, “The Space-Time Structure of Hadronization in the Lund Model,” *Eur. Phys. J. C*, vol. 78, no. 11, p. 983, Nov. 2018.
- [22] T. Sjostrand, “QCD for BSM in PYTHIA,” IMPU-YITP Workshop, Kyoto, 2011.
- [23] T. Åkesson *et al.*, “Double Parton Scattering in $p\ p$ Collisions at $\sqrt{s}=63$ -GeV,” *Z. Phys. C*, vol. 34, p. 163, 1987.
- [24] Z. Koba, H. B. Nielsen, and P. Olesen, “Scaling of multiplicity distributions in high energy hadron collisions,” *Nuclear Physics B*, vol. 40, pp. 317–334, Jan. 1972.
- [25] G. J. Alner *et al.*, “Scaling violation favouring high multiplicity events at 540 GeV CMS energy,” *Physics Letters B*, vol. 138, no. 4, pp. 304–310, Apr. 1984.

- [26] R. E. Ansorge *et al.*, “Charged particle multiplicity distributions at 200 and 900 GeV c.m. energy,” *Z. Phys. C - Particles and Fields*, vol. 43, no. 3, pp. 357–374, Sep. 1989.
- [27] T. Sjöstrand, “The Development of MPI Modelling in PYTHIA,” Jun. 2017.
- [28] “Electroweak measurements in electron–positron collisions at W-boson-pair energies at LEP,” *Physics Reports*, vol. 532, no. 4, pp. 119–244, Nov. 2013.
- [29] C. Bierlich *et al.*, “A comprehensive guide to the physics and usage of PYTHIA 8.3,” Mar. 2022.
- [30] G. Gustafson, “Multiple Interactions, Saturation, and Final States in pp Collisions and DIS,” May 2009.
- [31] A. Ortiz *et al.*, “Color reconnection and flow-like patterns in pp collisions,” *Phys. Rev. Lett.*, vol. 111, no. 4, p. 042001, Jul. 2013.
- [32] CDF Collaboration *et al.*, “Charged jet evolution and the underlying event in proton-antiproton collisions at 1.8 TeV,” *Phys. Rev. D*, vol. 65, no. 9, p. 092002, Apr. 2002.
- [33] G. Arnison *et al.*, “Hadronic jet production at the CERN proton-antiproton collider,” *Physics Letters B*, vol. 132, no. 1, pp. 214–222, Nov. 1983.
- [34] H. Caines, “Underlying Event Studies at RHIC,” Oct. 2009.
- [35] C. E. DeTar and J. F. Donoghue, “BAG MODELS OF HADRONS,” *Ann.Rev.Nucl.Part.Sci.*, vol. 33, pp. 235–264, 1983.
- [36] O. Matonoha, “Upsilon meson production in heavy-ion collisions at the STAR experiment,” Diploma Thesis (Monograph), Czech Technical University in Prague, 2018.
- [37] J. McGreevy, “Lecture Notes: Quantum Ideal Gases.”
- [38] H. B. Meyer, “Lattice QCD: A Brief Introduction,” in *Lattice QCD for Nuclear Physics*, ser. Lecture Notes in Physics, H.-W. Lin and H. B. Meyer, Eds. Cham: Springer International Publishing, 2015, pp. 1–34.
- [39] E. Bennett *et al.*, “BSMBench: A flexible and scalable HPC benchmark from beyond the standard model physics,” in *2016 International Conference on High Performance Computing & Simulation (HPCS)*, Jul. 2016, pp. 834–839.
- [40] K. Nagata, “Finite-density lattice QCD and sign problem: Current status and open problems,” *Progress in Particle and Nuclear Physics*, vol. 127, p. 103991, Nov. 2022.

- [41] S. Dürr *et al.*, “Ab Initio Determination of Light Hadron Masses,” *Science*, vol. 322, no. 5905, pp. 1224–1227, Nov. 2008.
- [42] P. Petreczky, “Lattice QCD at non-zero temperature,” *J. Phys. G: Nucl. Part. Phys.*, vol. 39, no. 9, p. 093002, Aug. 2012.
- [43] A. Bazavov *et al.*, “The equation of state in (2+1)-flavor QCD,” *Phys. Rev. D*, vol. 90, no. 9, p. 094503, Nov. 2014.
- [44] R. Pasechnik and M. Šumbera, “Phenomenological Review on Quark–Gluon Plasma: Concepts vs. Observations,” *Universe*, vol. 3, no. 1, p. 7, Jan. 2017.
- [45] H. Sazdjian, “Introduction to chiral symmetry in QCD,” *EPJ Web Conf.*, vol. 137, p. 02001, 2017.
- [46] S. Gottlieb *et al.*, “Estimating the chiral-symmetry–restoration temperature in two-flavor QCD,” *Phys. Rev. Lett.*, vol. 59, no. 14, pp. 1513–1516, Oct. 1987.
- [47] Y.-Z. Xu, S.-X. Qin, and H.-S. Zong, “Chiral symmetry restoration and properties of Goldstone bosons at finite temperature,” *Chinese Phys. C*, vol. 47, no. 3, p. 033107, Mar. 2023.
- [48] S. Collaboration *et al.*, “Search for the Chiral Magnetic Effect with Isobar Collisions at $\sqrt{s_{NN}} = 200$ GeV by the STAR Collaboration at RHIC,” Aug. 2021.
- [49] P. M. Hohler and R. Rapp, “Is ρ -meson melting compatible with chiral restoration?” *Physics Letters B*, vol. 731, pp. 103–109, Apr. 2014.
- [50] M. L. Miller *et al.*, “Glauber Modeling in High Energy Nuclear Collisions,” *Annu. Rev. Nucl. Part. Sci.*, vol. 57, no. 1, pp. 205–243, Nov. 2007.
- [51] D. Kharzeev and M. Nardi, “Hadron production in nuclear collisions at RHIC and high density QCD,” *Physics Letters B*, vol. 507, no. 1-4, pp. 121–128, May 2001.
- [52] B. Schenke, P. Tribedy, and R. Venugopalan, “Fluctuating Glasma Initial Conditions and Flow in Heavy Ion Collisions,” *Phys. Rev. Lett.*, vol. 108, no. 25, p. 252301, Jun. 2012.
- [53] C. Loizides, “Glauber modeling of high-energy nuclear collisions at sub-nucleon level,” *Phys. Rev. C*, vol. 94, no. 2, p. 024914, Aug. 2016.
- [54] S. Borsányi, “Thermodynamics of the QCD transition from lattice,” *Nuclear Physics A*, vol. 904–905, pp. 270c–277c, May 2013.

- [55] I. Arsene *et al.*, “Quark–gluon plasma and color glass condensate at RHIC? The perspective from the BRAHMS experiment,” *Nuclear Physics A*, vol. 757, no. 1, pp. 1–27, Aug. 2005.
- [56] J. Adams *et al.*, “Experimental and theoretical challenges in the search for the quark–gluon plasma: The STAR Collaboration’s critical assessment of the evidence from RHIC collisions,” *Nuclear Physics A*, vol. 757, no. 1, pp. 102–183, Aug. 2005.
- [57] T. Niida and Y. Miake, “Signatures of QGP at RHIC and the LHC,” Apr. 2021.
- [58] U. Heinz and M. Jacob, “Evidence for a New State of Matter: An Assessment of the Results from the CERN Lead Beam Programme,” Feb. 2000.
- [59] CMS Collaboration, “Measurement of nuclear modification factors of $\Upsilon(1S)$, $\Upsilon(2S)$, and $\Upsilon(3S)$ mesons in PbPb collisions at $\sqrt{s_{\text{NN}}} = 5.02 \text{ TeV}$,” *Physics Letters B*, vol. 790, pp. 270–293, Mar. 2019.
- [60] L. Adamczyk *et al.*, “Global Λ hyperon polarization in nuclear collisions,” *Nature*, vol. 548, no. 7665, pp. 62–65, Aug. 2017.
- [61] D. E. Kharzeev, L. D. McLerran, and H. J. Warringa, “The effects of topological charge change in heavy ion collisions: ”Event by event P and CP violation”,” *Nuclear Physics A*, vol. 803, no. 3-4, pp. 227–253, May 2008.
- [62] ALICE Collaboration, “The ALICE experiment – A journey through QCD,” Nov. 2022.
- [63] S. Sarkar, H. Satz, and B. Sinha, Eds., *The Physics of the Quark-Gluon Plasma: Introductory Lectures*, ser. Lecture Notes in Physics. Berlin, Heidelberg: Springer, 2010, vol. 785.
- [64] T. Matsui and H. Satz, “ J/ψ suppression by quark-gluon plasma formation,” *Physics Letters B*, vol. 178, no. 4, pp. 416–422, Oct. 1986.
- [65] H. Satz, “Probing the States of Matter in QCD,” *Int. J. Mod. Phys. A*, vol. 28, no. 27, p. 1330043, Oct. 2013.
- [66] B. Kroupa and M. Strickland, “Predictions for bottomonia suppression in 5.023 TeV Pb-Pb collisions,” *Universe*, vol. 2, no. 3, p. 16, Aug. 2016.
- [67] J. Rafelski and B. Müller, “Strangeness Production in the Quark-Gluon Plasma,” *Phys. Rev. Lett.*, vol. 48, no. 16, pp. 1066–1069, Apr. 1982.
- [68] P. Koch, B. Müller, and J. Rafelski, “Strangeness in relativistic heavy ion collisions,” *Physics Reports*, vol. 142, no. 4, pp. 167–262, Sep. 1986.

- [69] ALICE Collaboration, “Multi-strange baryon production in p-Pb collisions at $\sqrt{s_{\text{NN}}} = 5.02 \text{ TeV}$,” Jan. 2016.
- [70] A. Andronic, P. Braun-Munzinger, and J. Stachel, “Thermal hadron production in relativistic nuclear collisions: The hadron mass spectrum, the horn, and the QCD phase transition,” *Physics Letters B*, vol. 673, no. 2, pp. 142–145, Mar. 2009.
- [71] S. Wheaton, J. Cleymans, and M. Hauer, “THERMUS—A thermal model package for ROOT,” *Computer Physics Communications*, vol. 180, no. 1, pp. 84–106, Jan. 2009.
- [72] S. Hamieh, K. Redlich, and A. Tounsi, “Canonical Description of Strangeness Enhancement from p-A to Pb-Pb Collisions,” *Physics Letters B*, vol. 486, no. 1-2, pp. 61–66, Jul. 2000.
- [73] ALICE Collaboration, “Centrality dependence of π , K, p production in Pb-Pb collisions at $\sqrt{s_{\text{NN}}} = 2.76 \text{ TeV}$,” *Phys. Rev. C*, vol. 88, no. 4, p. 044910, Oct. 2013.
- [74] ———, “ K_S^0 and Λ production in Pb-Pb collisions at $\sqrt{s_{\text{NN}}} = 2.76 \text{ TeV}$,” *Phys. Rev. Lett.*, vol. 111, no. 22, p. 222301, Nov. 2013.
- [75] ———, “ $K^*(892)^0$ and $\Phi(1020)$ production in Pb-Pb collisions at $\sqrt{s_{\text{NN}}} = 2.76 \text{ TeV}$,” *Phys. Rev. C*, vol. 91, no. 2, p. 024609, Feb. 2015.
- [76] C. M. Hung and E. Shuryak, “Equation of State, Radial Flow and Freeze-out in High Energy Heavy Ion Collisions,” *Phys. Rev. C*, vol. 57, no. 4, pp. 1891–1906, Apr. 1998.
- [77] E. Schnedermann, J. Sollfrank, and U. Heinz, “Thermal phenomenology of hadrons from 200 AGeV S+S collisions,” *Phys. Rev. C*, vol. 48, no. 5, pp. 2462–2475, Nov. 1993.
- [78] K. Werner *et al.*, “Analysing radial flow features in p-Pb and p-p collisions at several TeV by studying identified particle production in EPOS3,” *Phys. Rev. C*, vol. 89, no. 6, p. 064903, Jun. 2014.
- [79] S. Voloshin and Y. Zhang, “Flow Study in Relativistic Nuclear Collisions by Fourier Expansion of Azimuthal Particle Distributions,” *Zeitschrift für Physik C Particles and Fields*, vol. 70, no. 4, pp. 665–671, May 1996.
- [80] B. Alver and G. Roland, “Collision geometry fluctuations and triangular flow in heavy-ion collisions,” *Phys. Rev. C*, vol. 82, no. 3, p. 039903, Sep. 2010.

- [81] ALICE Collaboration, “Higher harmonic anisotropic flow measurements of charged particles in Pb-Pb collisions at 2.76 TeV,” *Phys. Rev. Lett.*, vol. 107, no. 3, p. 032301, Jul. 2011.
- [82] M. Luzum, “Flow fluctuations and long-range correlations: Elliptic flow and beyond,” *J. Phys. G: Nucl. Part. Phys.*, vol. 38, no. 12, p. 124026, Dec. 2011.
- [83] ALICE Collaboration, “Elliptic flow of identified hadrons in Pb-Pb collisions at $\sqrt{s_{\text{NN}}} = 2.76$ TeV,” *J. High Energ. Phys.*, vol. 2015, no. 6, p. 190, Jun. 2015.
- [84] K. Schade, “Applications of Holography to Strongly Coupled Plasmas,” Ph.D. dissertation, 2012.
- [85] M. Gyulassy and M. Plümer, “Jet quenching in dense matter,” *Physics Letters B*, vol. 243, no. 4, pp. 432–438, Jul. 1990.
- [86] X.-N. Wang, “Effect of Jet Quenching on High- p_T Hadron Spectra in High-energy Nuclear Collisions,” *Phys. Rev. C*, vol. 58, no. 4, pp. 2321–2330, Oct. 1998.
- [87] M. Gyulassy, P. Levai, and I. Vitev, “Non-Abelian Energy Loss at Finite Opacity,” *Phys. Rev. Lett.*, vol. 85, no. 26, pp. 5535–5538, Dec. 2000.
- [88] K. Zapp *et al.*, “A Monte Carlo Model for ‘Jet Quenching’,” *Eur. Phys. J. C*, vol. 60, no. 4, p. 617, Apr. 2009.
- [89] C. CMS, “CMS collision events: From lead ion collisions,” <http://cdsweb.cern.ch/record/1309898>, 2010.
- [90] R. Vogt, “Shadowing Effects on J/ψ and Υ Production at the LHC,” *Phys. Rev. C*, vol. 92, no. 3, p. 034909, Sep. 2015.
- [91] J. W. Cronin *et al.*, “Production of hadrons at large transverse momentum at 200, 300, and 400 GeV,” *Phys. Rev. D*, vol. 11, no. 11, pp. 3105–3123, Jun. 1975.
- [92] C. Wong, *Introduction to High-Energy Heavy-Ion Collisions*. United States: World Scientific Pub Co, 1990.
- [93] E. G. Ferreiro, “Excited charmonium suppression in proton–nucleus collisions as a consequence of comovers,” *Physics Letters B*, vol. 749, pp. 98–103, Oct. 2015.
- [94] J. Adam *et al.*, “Enhanced production of multi-strange hadrons in high-multiplicity proton–proton collisions,” *Nature Phys.*, vol. 13, no. 6, pp. 535–539, Jun. 2017.

- [95] ALICE Collaboration, “Multiplicity dependence of J/ψ production at midrapidity in pp collisions at $\sqrt{s} = 13$ TeV,” *Physics Letters B*, vol. 810, p. 135758, Nov. 2020.
- [96] ———, “Observation of a multiplicity dependence in the p_T -differential charm baryon-to-meson ratios in proton-proton collisions at $\sqrt{s} = 13$ TeV,” *Physics Letters B*, vol. 829, p. 137065, Jun. 2022.
- [97] CMS Collaboration, “Evidence for collectivity in pp collisions at the LHC,” *Physics Letters B*, vol. 765, pp. 193–220, Feb. 2017.
- [98] R. D. Weller and P. Romatschke, “One fluid to rule them all: Viscous hydrodynamic description of event-by-event central p+p, p+Pb and Pb+Pb collisions at $\sqrt{s} = 5.02$ TeV,” *Physics Letters B*, vol. 774, pp. 351–356, Nov. 2017.
- [99] ALICE Collaboration, “Investigations of anisotropic flow using multi-particle azimuthal correlations in pp, p-Pb, Xe-Xe, and Pb-Pb collisions at the LHC,” *Phys. Rev. Lett.*, vol. 123, no. 14, p. 142301, Oct. 2019.
- [100] ———, “Multiplicity dependence of (multi-)strange hadron production in proton-proton collisions at $\sqrt{s} = 13$ TeV,” *Eur. Phys. J. C*, vol. 80, no. 2, p. 167, Feb. 2020.
- [101] CMS Collaboration, “Investigation into the event-activity dependence of $\Upsilon(nS)$ relative production in proton-proton collisions at $\sqrt{s} = 7$ TeV,” *J. High Energ. Phys.*, vol. 2020, no. 11, p. 1, Nov. 2020.
- [102] S. Behrends *et al.*, “Inclusive Hadron Production in Upsilon Decays and in Nonresonant electron-Positron Annihilation at 10.49-GeV,” *Phys. Rev. D*, vol. 31, p. 2161, 1985.
- [103] CMS Collaboration, “Elliptic flow of charm and strange hadrons in high-multiplicity pPb collisions at $\sqrt{s_{NN}} = 8.16$ TeV,” *Phys. Rev. Lett.*, vol. 121, no. 8, p. 082301, Aug. 2018.
- [104] B. G. Zakharov, “Parton energy loss in the mini quark-gluon plasma and jet quenching in proton-proton collisions,” *J. Phys. G: Nucl. Part. Phys.*, vol. 41, no. 7, p. 075008, Jul. 2014.
- [105] S.-Y. Chen *et al.*, “Centrality Dependence of Productions for Single Hadrons and Inclusive Jets in High-Energy p + A Collisions with NLO QCD*,” *Commun. Theor. Phys.*, vol. 64, no. 1, p. 95, Jul. 2015.
- [106] ALICE Collaboration, “Constraints on jet quenching in p-Pb collisions at $\sqrt{s_{NN}} = 5.02$ TeV measured by the event-activity dependence of semi-inclusive hadron-jet distributions,” *Physics Letters B*, vol. 783, pp. 95–113, Aug. 2018.

- [107] J. Bellm *et al.*, “Herwig 7.2 Release Note,” *Eur. Phys. J. C*, vol. 80, no. 5, p. 452, May 2020.
- [108] E. Bothmann *et al.*, “Event Generation with Sherpa 2.2,” *SciPost Phys.*, vol. 7, no. 3, p. 034, Sep. 2019.
- [109] T. Sjöstrand, “The PYTHIA Event Generator: Past, Present and Future,” *Computer Physics Communications*, vol. 246, p. 106910, Jan. 2020.
- [110] P. Skands, S. Carrazza, and J. Rojo, “Tuning PYTHIA 8.1: The Monash 2013 tune,” *Eur. Phys. J. C*, vol. 74, no. 8, p. 3024, Aug. 2014.
- [111] C. Bierlich *et al.*, “The Angantyr model for Heavy-Ion Collisions in PYTHIA8,” *J. High Energ. Phys.*, vol. 2018, no. 10, p. 134, Oct. 2018.
- [112] T. Sjöstrand, S. Mrenna, and P. Skands, “A Brief Introduction to PYTHIA 8.1,” *Computer Physics Communications*, vol. 178, no. 11, pp. 852–867, Jun. 2008.
- [113] C. Bierlich and J. R. Christiansen, “Effects of Colour Reconnection on Hadron Flavour Observables,” *Phys. Rev. D*, vol. 92, no. 9, p. 094010, Nov. 2015.
- [114] T. S. Biro, H. B. Nielsen, and J. Knoll, “Colour rope model for extreme relativistic heavy ion collisions,” *Nuclear Physics B*, vol. 245, pp. 449–468, Jan. 1984.
- [115] H. Sorge *et al.*, “Colour rope formation and strange baryon production in ultrarelativistic heavy ion collisions,” *Physics Letters B*, vol. 289, no. 1, pp. 6–11, Sep. 1992.
- [116] C. Bierlich *et al.*, “Effects of Overlapping Strings in pp Collisions,” Feb. 2015.
- [117] C. Bierlich, G. Gustafson, and L. Lönnblad, “A shoving model for collectivity in hadronic collisions,” Dec. 2016.
- [118] H. J. Drescher *et al.*, “Parton-Based Gribov-Regge Theory,” *Physics Reports*, vol. 350, no. 2-4, pp. 93–289, Sep. 2001.
- [119] K. Werner, F.-M. Liu, and T. Pierog, “Parton Ladder Splitting and the Rapidity Dependence of Transverse Momentum Spectra in Deuteron-Gold Collisions at RHIC,” *Phys. Rev. C*, vol. 74, no. 4, p. 044902, Oct. 2006.
- [120] T. Pierog *et al.*, “EPOS LHC : Test of collective hadronization with LHC data,” *Phys. Rev. C*, vol. 92, no. 3, p. 034906, Sep. 2015.
- [121] T. Pierog and K. Werner, “EPOS Model and Ultra High Energy Cosmic Rays,” *Nuclear Physics B - Proceedings Supplements*, vol. 196, pp. 102–105, Dec. 2009.

- [122] A. G. Knospe *et al.*, “Hadronic resonance production and interaction in partonic and hadronic matter in EPOS₃ with and without the hadronic afterburner UrQMD,” *Phys. Rev. C*, vol. 93, no. 1, p. 014911, Jan. 2016.
- [123] ———, “Hadronic resonance production and interaction in p-Pb collisions at LHC energies in EPOS₃,” *Phys. Rev. C*, vol. 104, no. 5, p. 054907, Nov. 2021.
- [124] R. Cashmore, L. Maiani, and J.-P. Revol, Eds., *Prestigious Discoveries at CERN*. Berlin, Heidelberg: Springer, 2003.
- [125] T. A. Collaboration *et al.*, “The ATLAS Experiment at the CERN Large Hadron Collider,” *J. Inst.*, vol. 3, no. 08, p. S08003, Aug. 2008.
- [126] T. C. Collaboration *et al.*, “The CMS experiment at the CERN LHC,” *J. Inst.*, vol. 3, no. 08, p. S08004, Aug. 2008.
- [127] T. L. Collaboration *et al.*, “The LHCb Detector at the LHC,” *J. Inst.*, vol. 3, no. 08, p. S08005, Aug. 2008.
- [128] R. Schmidt *et al.*, “Protection of the CERN Large Hadron Collider,” *New J. Phys.*, vol. 8, no. 11, p. 290, Nov. 2006.
- [129] M. Brice, “Aerial View of the CERN taken in 2008.” 2008.
- [130] “LHC report: Make way for the heavy ions,” <https://home.cern/news/news/accelerators/lhc-report-make-way-heavy-ions>, Mar. 2023.
- [131] T. A. Collaboration *et al.*, “The ALICE experiment at the CERN LHC,” *J. Inst.*, vol. 3, no. 08, p. S08002, Aug. 2008.
- [132] ALICE Collaboration, “Performance of the ALICE Experiment at the CERN LHC,” *Int. J. Mod. Phys. A*, vol. 29, no. 24, p. 1430044, Sep. 2014.
- [133] V. Peskov, M. Planicic, and F. García, *Technical Design Report for the Upgrade of the ALICE Time Projection Chamber*, Mar. 2014.
- [134] A. Kalweit, “Production of light flavor hadrons and anti-nuclei at the LHC,” Monograph, Technische Universität Darmstadt, 2012.
- [135] J. Adolfsson *et al.*, “The upgrade of the ALICE TPC with GEMs and continuous readout,” *JINST*, vol. 16, no. arXiv:2012.09518, 2021.
- [136] ALICE Collaboration, “Alignment of the ALICE Inner Tracking System with cosmic-ray tracks,” *J. Inst.*, vol. 5, no. 03, pp. Po3 003–Po3 003, Mar. 2010.

- [137] M. Krammer, “Silicon detectors in High Energy Physics experiments,” *Scholarpedia*, vol. 10, no. 10, p. 32486, 2015.
- [138] S. Masciocchi, “Lecture notes: Semiconductor detectors,” 2017.
- [139] ALICE Collaboration, “Performance of the ALICE VZERO system,” *J. Inst.*, vol. 8, no. 10, pp. P10016–P10016, Oct. 2013.
- [140] M. Krivda *et al.*, “The ALICE trigger system performance for p-p and Pb-Pb collisions,” *J. Inst.*, vol. 7, no. 01, p. C01057, Jan. 2012.
- [141] A. D. P. Group, “ALICE Data Flow,” Nov. 2018.
- [142] M. Arslanbekov *et al.*, “Track Reconstruction in a High-Density Environment with ALICE,” *Particles*, vol. 5, no. 1, pp. 84–95, Mar. 2022.
- [143] A. Maire, “Production des baryons multi-étranges au LHC dans les collisions proton-proton avec l’expérience ALICE,” Ph.D. dissertation, Strasbourg U., 2011.
- [144] G. Contin, “Performance of the present ALICE Inner Tracking System and studies for the upgrade,” *J. Inst.*, vol. 7, no. 06, p. C06007, Jun. 2012.
- [145] ALICE Collaboration, “Centrality determination of Pb-Pb collisions at $\sqrt{s_{\text{NN}}} = 2.76 \text{ TeV}$ with ALICE,” *Phys. Rev. C*, vol. 88, no. 4, p. 044909, Oct. 2013.
- [146] ——, “Multiplicity dependence of light-flavor hadron production in pp collisions at $\sqrt{s} = 7 \text{ TeV}$,” *Phys. Rev. C*, vol. 99, no. 2, p. 024906, Feb. 2019.
- [147] ——, “The ALICE definition of primary particles,” 2017.
- [148] R. Brun *et al.*, *GEANT: Detector Description and Simulation Tool*; Oct 1994, ser. CERN Program Library. Geneva: CERN, 1993.
- [149] S. Agostinelli *et al.*, “GEANT4-a simulation toolkit,” *Nuclear Instruments and Methods in Physics Research Section A Accelerators Spectrometers Detectors and Associated Equipment*, vol. 506, p. 250, Jul. 2003.
- [150] R. Brandelik *et al.*, “Evidence for a spin-1 gluon in three-jet events,” *Physics Letters B*, vol. 97, no. 3, pp. 453–458, Dec. 1980.
- [151] A. Ortiz, “Experimental results on event shapes at hadron colliders,” Dec. 2018, vol. 29, pp. 343–357.
- [152] A. Banfi, G. P. Salam, and G. Zanderighi, “Phenomenology of event shapes at hadron colliders,” *J. High Energ. Phys.*, vol. 2010, no. 6, p. 38, Jun. 2010.

- [153] ALICE Collaboration, “Charged-particle production as a function of multiplicity and transverse spherocity in pp collisions at $\sqrt{s} = 5.02$ and 13 TeV,” *Eur. Phys. J. C*, vol. 79, no. 10, p. 857, Oct. 2019.
- [154] E. Cuautle *et al.*, “Disentangling the soft and hard components of the pp collisions using the sphero(i)city approach,” Apr. 2014.
- [155] E. Cuautle, A. Ortiz, and G. Paic, “Mid-rapidity charged hadron transverse spherocity in pp collisions simulated with Pythia,” *Nuclear Physics A*, vol. 941, pp. 78–86, Sep. 2015.
- [156] A. Nassirpour, “The Shape of Strangeness: Transverse Spherocity and Underlying Event studies of φ and its relation to Ξ in $\sqrt{s} = 13$ TeV pp collisions,” Doctoral Thesis (Monograph), Lund University (Media-Tryck), Nov. 2022.
- [157] O. Vazquez Rueda, “Study of the production of π , K and p in pp collisions at $\sqrt{s} = 13$ TeV as a function of the Transverse Spherocity and the Relative Transverse Activity,” Doctoral Thesis (Monograph), Lund, 2022.
- [158] S. Acharya *et al.*, “Production of Λ and KSo in jets in p–Pb collisions at $s_{\text{NN}}=5.02$ TeV and pp collisions at $s=7$ TeV,” *Physics Letters B*, vol. 827, p. 136984, Apr. 2022.
- [159] ALICE Collaboration, “Multiplicity dependence of charged-particle production in pp, p–Pb, Xe–Xe and Pb–Pb collisions at the LHC,” Nov. 2022.
- [160] A. Collaboration, “Measurement of charged-particle distributions sensitive to the underlying event in $\sqrt{s} = 13$ TeV proton-proton collisions with the ATLAS detector at the LHC,” *J. High Energ. Phys.*, vol. 2017, no. 3, p. 157, Mar. 2017.
- [161] ALICE Collaboration, “Underlying Event measurements in pp collisions at $\sqrt{s} = 0.9$ and 7 TeV with the ALICE experiment at the LHC,” *J. High Energ. Phys.*, vol. 2012, no. 7, p. 116, Jul. 2012.
- [162] ALICE Collaboration, “Underlying-event properties in pp and p–Pb collisions at $\sqrt{s_{\text{NN}}} = 5.02$ TeV,” Apr. 2022.
- [163] T. Martin, P. Skands, and S. Farrington, “Probing collective effects in hadronisation with the extremes of the underlying event,” *Eur. Phys. J. C*, vol. 76, no. 5, p. 299, May 2016.
- [164] ALICE Collaboration, “Underlying Event properties in pp collisions at $\sqrt{s} = 13$ TeV,” *J. High Energ. Phys.*, vol. 2020, no. 4, p. 192, Apr. 2020.

- [165] ——, “Production of pions, kaons and protons as a function of the transverse event activity in pp collisions at $\sqrt{s} = 13$ TeV,” Jan. 2023.
- [166] G. Bencédi, A. Ortiz, and A. Paz, “Disentangling the hard gluon bremsstrahlung effects from the relative transverse activity classifier in p p collisions,” *Phys. Rev. D*, vol. 104, no. 1, p. 016017, Jul. 2021.
- [167] R. Field, “The Underlying Event in Hadronic Collisions,” *Annual Review of Nuclear and Particle Science*, vol. 62, no. 1, pp. 453–483, 2012.
- [168] B. Z. Kopeliovich *et al.*, “Cronin Effect in Hadron Production off Nuclei,” *Phys. Rev. Lett.*, vol. 88, no. 23, p. 232303, May 2002.
- [169] G. D’Agostini, “A multidimensional unfolding method based on Bayes’ theorem,” *Nuclear Instruments and Methods in Physics Research Section A: Accelerators, Spectrometers, Detectors and Associated Equipment*, vol. 362, no. 2, pp. 487–498, Aug. 1995.
- [170] A. Ortiz, “Energy dependence of underlying-event observables from RHIC to LHC energies,” *Phys. Rev. D*, vol. 104, no. 7, p. 076019, Oct. 2021.